Morphological and Multifractal Analyses of Retinal Amyloid Deposits for Staging in Alzheimer's Disease

by

Peter Andrew Charles Neathway

A thesis
presented to the University of Waterloo
in fulfillment of the
thesis requirement for the degree of
Master of Science
in
Physics (Nanotechnology)

Waterloo, Ontario, Canada, 2019

Author's Declaration

This thesis consists of material all of which I authored or co-authored: see Statement of Contributions included in the thesis. This is a true copy of the thesis, including any required final revisions, as accepted by my examiners.

I understand that my thesis may be made electronically available to the public.

Statement of Contributions

Veronica Hirsch-Reinshagen of the University of British Columbia performed the brain pathology. Rachel Redekop, Laura Emptage, and Monika Kitor performed the dissections and captured the images necessary for the Mueller Matrix calculations. Laura Emptage also introduced me to confocal microscopy and assisted in the preparation of materials for the initial electron microscopy experiments. Erik Mason developed both the custom phase correlation image registration method and the original automated segmentation method for our polarimetry data and provided useful feedback in the debugging of several programs I wrote for this research. Tao Jin also provided some assistance with debugging programs, especially related to the segmentation of confocal image stacks. Several confocal image stacks were collected by Monika Kitor and her initials appear in the captions of the associated figures. Figures 1.1, 2.6, 2.8b, and 2.12 contain images that have been included (with appropriate permission) from works by other authors.

Members of Campbell Labs also aided in the detection of grammatical mistakes, including Steven Esau, Monika Kitor, Rachel Redekop, and Laura Emptage. Outside of the academic community, I would further like to acknowledge the grammatical revisions provided by my partner's mother, Carol-Ann Reintsma, and my own, Maxine Brown. To all of you, I am grateful.

I would like to thank Dr. Strickland and Dr. Leonenko for being on my primary research advisory committee, and for their contributions to my academic performance. Furthermore, I thank Dr. Bizheva for agreeing to be an external examiner of my thesis, and taking on this hefty document as holiday reading on very short notice.

The most direct contribution to my thesis work came directly from Dr. Campbell. She has spent many hours helping me find the right ways to express and refine my ideas, and has contributed to the development of ideas presented in my second chapter. It was through her guidance and patience that I have been able to perform and complete this work, and most of all, to appreciate its importance. Additionally, her support of my academic career and future ambitions has been of the utmost importance to my personal growth. For these reasons, and others that are too numerous to count, I am grateful to Dr. Campbell, and thankful for her contributions to my research.

Abstract

Dementia is a neurodegenerative condition that leads to loss of cognitive ability, typically in older adults. Alzheimer's disease (AD) is the most common cause of dementia and affects millions of people worldwide. The prominence and impact of AD is expected to intensify in the near future, especially in Canada, as the world's population continues to age. Current treatments for AD can delay symptoms, but there is no cure that has been made available to the general population. Detection of AD has been at the forefront of the medical sciences for decades but still involves expensive and inaccessible procedures.

Dr. Campbell's group has shown that amyloid deposits, a hallmark of AD in the brain, also occur in the retina, in quantities correlated with brain pathology. The optical accessibility of the retina makes it a strong candidate for future diagnostic methods. In preparation for the implementation of a live-eye imaging device, our group has continued to seek new means for extracting information related to said deposits that could be of diagnostic interest. This thesis includes a description of the three-dimensional morphological features of amyloid deposits found in the retina, with proposed explanations for said features. Most deposits appear to be very flat, like sheets in the *en face* plane, and bear little resemblance to the typical isotropic deposits found in the brain.

This thesis applied complexity and texture analysis to differentiate between key categories of amyloid deposits in human retinas. Texture analysis and polarization signals were both different on average for deposits in different layers of the retina, deposits from subjects with different likelihoods of AD, and deposits from subjects with AD from those with other pathologies. Tests were performed to assess the resilience of these methods to various resolutions (using both digital resampling and different magnifications in the imaging apparatuses) and orientations. Further analysis considered deposit texture as a function of depth in three-dimensional image volumes and found that texture appears to be somewhat continuous, to an extent that may be useful for the live-eye imaging application.

Acknowledgements

In completing this research, I received invaluable assistance from the other members of Dr. Campbell's group, and certainly from Dr. Campbell herself. This group supported my project academically and I consider each of them to be true friends.

I would also like to thank Pierrick Legrand and the other members of INRIA for sharing the raw code used in FracLab, and for their willingness to share details of the program's inner workings with me. I would like to express my gratitude towards Dr. Kathryn Grandfield for guiding the experimental configuration for the electron microscopy experiments, to Laura Emptage for determining optimal means of sample preparation for the electron microscopy experiments, and to Dr. Edward Vrscay for helpful discussions about fractals and their meanings. Lastly, I wish to thank Dr. Melanie Campbell for her supervision, guidance, and trust in my research, and for being of the utmost support. I am sure there are others I have omitted here, but I am certainly in debt to many fellow researchers, my friends, and the entire community at the University of Waterloo for the technical and social support I have received over the past couple of years.

Dedication

This thesis report is dedicated to my family, friends, and to my fiancée Anna Reintsma for her unwavering support.

Table of Contents

List of Figures

List of Tables

List of Acronyms

3D	Three dimensional
AD	Alzhiemer's disease
ALS	Amyotrophic lateral sclerosis
AMD	Age-related macular degeneration
CAA	Cerebral amyloid angiopathy
CCD	Charge coupled device
CSLM	Confocal scanning laser microscope
CVD	Cerebral vascular disease
DAPI	4',6-Diamidino-2-phenylindole
DLB	Dementia with Lewy bodies
EELS	Electron energy loss spectroscopy
FITC	Fluorescein isothiocyanate
FTLD	Frontotemporal lobular degeneration
HS	Hippocampal sclerosis
KS	Kolmogorov-Smirnov
MFA	Multifractal analysis
MFS	Multifractal spectrum
OCT	Optical coherence tomography
ONFL	Optical nerve fiber layer
P1	Linear polarizer within the PSG
P2	Linear polarizer within the PSA

PC Personal computer

PCA Principal component analysis

PET Positron emission tomography

PSA Polarization state analyzer

PSG Polarization state generator

RGC Retinal ganglion cell

STEM Scanning transmission electron microscope

TDP-43 Transactive response deoxyribonucleic acid-binding protein 43

TEM Transmission electron microscope

List of Symbols

α	Point-wise Hölder exponent
ϵ	Lower limit of region size considered in theoretical Hausdorff dimension calculation
μ	Capacity for Hölder exponent calculation
$A*$	a-metric
A_θ	Anisotropy angle
A_C	Circular anisotropy
A_L	Linear anisotropy
A_T	Total anisotropy
b	b-metric
CI_L	Lower bound on the confidence interval for the tests of multifractal spectra for rotated deposit z-stacks
CI_U	Upper bound on the confidence interval for the tests of multifractal spectra for rotated deposit z-stacks
D_θ	Diattenuation angle
$\vec{D}$	Diattenuation vector
D_C	Circular diattenuation
D_I	Depolarization index
D_L	Linear diattenuation
D_T	Total diattenuation
E	Entropy
F	Hausdorff dimension

H_s^q	Theoretical Hausdorff content
$Hvec$	List of region sizes used in Hölder exponent calculation
$Hvec_{min}$	The smallest region size used in the Hölder exponent calculation
$Hvec_{max}$	The greatest region size used in the Hölder exponent calculation
I	An image
kurtosis	The 4th moment of said distribution of the probability distribution of the spectrum
M	Mueller matrix
M_Δ	Mueller matrix of a depolarizer
M^O	Magnification associated with objective O
M_D	Mueller matrix of a diattenuator
MFE	Trapezoidal integral of an MFS
MFR	The difference between the greatest and smallest Hölder exponent bin values
M_{PSA}	Mueller matrix of the polarization state analyzer
M_{PSG}	Mueller matrix of the polarization state generator
M_R	Mueller matrix of a retarder
$p1$	The prominence of peak 1
$p2$	The prominence of peak 2
p_{2WIL}	P-value associated with a 2-sided Wilcoxon test
P_θ	Polarizance angle
$\vec{P}$	Polarizance vector
P_C	Circular polarizance
peak ratio	The ratio $\frac{F(x1)}{F(x2)}$

peak sep	The difference in the α of the peak 1 and peak 2
p_{KSA}	Asymptotic p-value associated with the two-sample Kolmogorov-Smirnov test
P_L	Linear polarizance
prom ratio	The ratio $\frac{p1}{p2}$
P_T	Total polarizance
q	q-metric
R_θ	Retardance angle
$\vec{R}$	Retardance vector
R_C	Circular retardance
R_L	Linear retardance
R_T	Total retardance
$\vec{S}$	Stokes vector representing input light
$\vec{S}'$	Stokes vector representing output light
skewness	The 3rd moment of said distribution of the probability distribution of the spectrum
$Svec$	List of region sizes used in Hausdorff dimension calculation
$Svec_{min}$	The smallest region size used in the Hausdorff dimension calculation
$Svec_{max}$	The greatest region size used in the Hausdorff dimension calculation
t	t-metric
T	Transmission
U_i	Diameter of the i^{th} ball used in the theoretical Hausdorff dimension calculation
$w1$	The full width at half max of peak 1

$w2$	The full width at half max of peak 2
width ratio	The ratio $\frac{w1}{w2}$
x	x-metric
$x1$	Hölder exponent associated with peak 1 (the most prominent peak of the spectrum)
$x2$	The Hölder exponent associated with peak 2 (the second most prominent peak of the spectrum)
x^O_{crop}	Dimensions of an image taken with objective O after cropping to match the dimensions contained in a field associated with the 40X objective
x^O	Original dimension of an image taken with objective O

Chapter 1

Introduction

1.1 Alzheimer's Disease

As the most common form of dementia, Alzheimer's disease (AD) is associated with loss of cognitive ability and an overall reduced quality of life. In 2017, 261,914 people died of dementia-related causes, 46% of which were AD-related [1]. AD is typically observed in older adults, but the Alzheimer Society of Canada [2] estimates that there were approximately 16000 Canadians younger than 65 living with AD in 2016 (based on results in [3]). In spite of decades of research into AD, no cure is readily available to the general population (though some pharmaceuticals are moving forward [4]). Models of the disease's impact, and existing statistics, suggest that the problem is becoming more widespread [5, 6], with this largely being due to an ageing population [6]. Treatments have only been able to delay disease progression, or to deal with symptoms but not underlying causes of AD [7, 8]. Early diagnosis of the disease may allow for treatments to have a more critical impact [9].

Conclusive diagnosis currently can only be performed *post mortem*, and other clinical techniques are either non-specific, or inaccessibly expensive. For instance, positron emission tomography (PET) scans, which have shown some clinical success for detecting AD [10, 11], typically cost between 900 and 1400 USD [12]. The study in [10] further qualified that the average cost per quality-adjusted life year[1] was €21,888. To recover expenses associated with scans, a study into the feasibility of PET in Canada [14] proposed that costs of 2195 CAD per PET study would be needed to counter costs if there were 740

[1] This unit describes both a period of time and a presumed quality of life [13].

new cases per year. The AD research by Dr. Campbell's lab is primarily motivated by the notion that noninvasive, inexpensive, accessible tools for detection of the early onset of the disease could lead to improved success in pharmaceutical trials, earlier and better treatments, and overall better quality of life.

1.2 Brain Pathology

AD is associated with the accumulation of several protein-laden deposits in the brain. This research focuses on deposits containing amyloid, presumably amyloid-β, but neurofibrillary tangles of tau protein are also associated with AD [15, 16]. Amyloid protein exists within the cerebral spinal fluid of healthy adults and is one of the substances cleared from the brain during sleep. One of the popular theories explaining amyloidosis of the brain is known as the Sink Hypothesis, which suggests that amyloid crosses the blood brain barrier by means of balance between the levels in the brain and the peripheral nervous system. If the balance is disrupted, as the protein accumulates in the brain, the amyloid precursor protein is cleaved in such a way that a portion forms fibrils, which form fibrillar bundles, and larger macro structures known as plaques or deposits. Though precursors to amyloid fibrils are believed to lead to cytotoxicity [17], the plaques are large enough that they can be detected through several clinical methods. Currently, positron emission tomography (PET) seems to be the most accurate method for measuring the density of amyloid plaques within the brain. Unfortunately, PET scans cost thousands of dollars and are not highly accessible due largely to equipment costs. Spinal taps can also detect changes in amyloid levels, but these are invasive. Recently, a unique blood test was developed that could be used to identify protein signals in the blood that are indicative of higher amyloid levels in the brain, but in spite of its potential for being a low cost solution it too would require taking blood and a series of analytic tests.

1.3 Amyloid Deposits in Animal Models

Both for diagnostic and pharmaceutical purposes, animal models of AD, and other neurodegenerative conditions, have been critical. These models have allowed easier access to brains affected by amyloidosis, and allow for the precise observation of plaque formation, using methods that are not necessarily safe for human subjects. Many deposit morphologies have been identified by previous groups using such techniques. These morphologies are also dependent on how the disease is modeled, whether it be a condition that mice

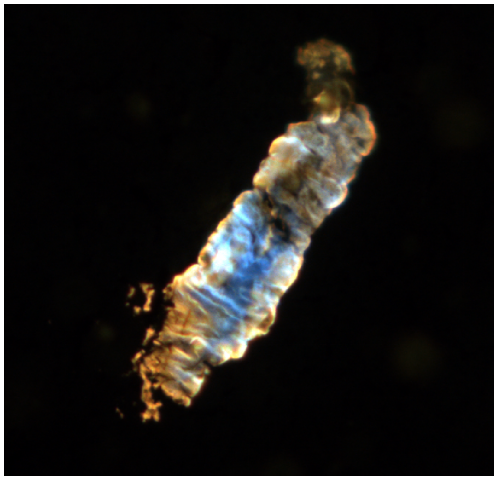

Figure 1.1: A blood vessel burdened with amyloid in a mouse brain, with colour channels representing different structural forms of amyloid (yellow → less mature; blue → more mature), included with permission of the researchers [21], courtesy of Sofie Nyström. Previously distributed in [22].

inherently are susceptible to, or through genetic manipulations. A study involving inbred mice that had been experimentally infected with scrapie [18] found that cerebral amyloid plaques fell into six different categories including *amorphous*, *giant*, and *perivascular* plaques (figure 2.6), among others. Other research groups have stained vessel-associated deposits in mice using techniques that stain different structural types of amyloid beta with different labels. In an article describing their work [19, 20, 21], Nyström *et al* presented a micrograph of an amyloid-laden blood vessel (figure 1.1). In the fluorescence signal associated with the less mature structure of amyloid (yellow), the edges of the deposit are bright. The center of the deposit in the cross-section view seems to have a very weak signal, though it is bright in the other fluorescence channel, associated with more mature amyloid structures (blue). Deposit growth rates have previously been tracked *in vivo* in mice [23]. This work revealed the rapidity of deposit formation in the mouse model (using B6C3-YFP and Tg2576 transgenic mice), on the scale of 24-48 hours. After initial formation, the investigators found that microglial cells soon arrived to deal with the newly formed deposits, but were not able to clear the new deposits away. The deposits analyzed in the study do not change significantly in size past the initial 48-hour window surrounding their formation, and the mean area was comparable between new plaques measured *in vivo* and plaques measured *post mortem* afterwards for the same specimens. Contrarily, another study found that amyloid β deposits in mice grew over a 25-week period [24], with new

and existing deposits both growing radially at a rate equivalent to 1 μm per month. The deposits tracked in [24] covered a range of sizes including those of the deposits in [23]. This dramatic difference might be due to differences in the strains of transgenic mice, and the in the ages of the mice upon the commencement of the study. Furthermore, the first group considered the cross-sectional area of deposits at specific layers repeatedly, whereas the second study used volumetric data from each deposit to calculate the equivalent radii (calculated by assuming spherical deposits). The latter of these studies found that larger deposits grow more rapidly, supporting a radial growth model.

Understanding the speed with which deposits form and the conditions of the tissue in which they form could be paramount for preventing their formation or disrupting early deposits. Yet another study uncovered more precisely that there are several stages of amyloid deposit growth [25]. Deposits form around so-called seeds and continue to grow and become denser until the concentration of amyloid-β limits increases in density. Deposits then proceed to grow with stable density, hence rapid change in volume, until reaching some asymptotic saturation point. Though this does not necessarily mean that cerebral amyloid and retinal amyloid accumulate in this same manner in human subjects, it still has implications for the work described in chapter 2 of categorizing the deposits found in human AD retinas, and theorizing possible reasons for particular morphologies.

There is a form of amyloidosis in the brain known as cerebral amyloid angiopathy (CAA) in which deposits form in association with vasculature. Occasionally, these take forms similar to the image shown in figure 2.12, with a pattern of bands. This pattern is due to the disruption of smooth muscle cells. Consider figure 2.12, taken with permission from Wolters Kluwer Health, Inc. [26]. This figure shows 2-photon images in which smooth muscle matter is stained green with phalloidin-Alexa 488 and amyloid is stained blue with methoxy-X04. As CAA progresses and the smooth muscle cells are disrupted, the amyloid accumulates in a banded structured around the vasculature, with a visibly darker region along the center axis.

1.4 Amyloid Deposits in the Human Brain

Studies involving human brain tissues have led to major conclusions pertaining to AD pathogenesis based on amyloid deposits in different regions. Amyloid plaques in the human brain have been reported as having isotropic structures in some cases, typically described as diffuse, fibrillar, or dense-core [27, 28]. Diffuse plaques are effectively amorphous in that there is no clear structure beyond the overall spherical "homogeneous" shape, fibrillar plaques reportedly have a center and lines running out from the center like a star, and

dense core plaques have a concentrated center and a diffusive cloud of amyloid forming a sphere around the core. The percentage of deposits in each of these categories was found to differ between different stages of AD [27], indicating structural changes that occur in tandem with disease progression.

Some studies of deposit growth in the human brain have been performed. Such studies are more difficult to perform than the analogous research described above for tracking deposit growth in animal models. The average size of dense-core plaques does not appear to correlate with clinical disease duration [29]. Other work in cognitively normal adults revealed that the volume of plaques grew roughly 8.0 % per year, across a 2.5-year period, in 17 of 21 individuals who initially had amyloid accumulation in the first test (using PET) [30]. These results connect to the result that deposits presumably appear in the human brain decades before symptoms occur.

CAA, which includes a variety of forms of vascular amyloidosis and other ways in which amyloid affects cerebral blood flow, is connected to AD in that there is significant coincidence of the two conditions [31]. Observations of CAA in the occipital cortex (which is primarily responsible for the human visual system) have led to the conclusion that in extreme cases, all features of an affected artery can be replaced by amyloid [32], with the accumulation beginning in the inner layers of the artery wall (basement membrane of the tunica media). There have been reports of banded patterns in amyloid-laden vessels in the human brain [33], identified using thioflavin-S staining, associated with the basement membranes of the smooth muscle cells. Beyond the basic geometric morphological analysis, some research has been performed to describe amyloid deposits in human brains through fractal analysis [34], which is described in more detail in chapter 3.

1.5 Amyloid Deposits in the Human Retina

Deposits found in the human retina have several similarities to those in the brain. As addressed by Koronyo *et al* [35], both brain and retina contain microglia, neurons, and other features that are structurally similar. However, the retinal tissue is distinct from brain tissue in that it is organized as a series of effectively two-dimensional layers. This implies the possibility for similar and different deposit morphologies in the brain and retina. Koronyo's group used different methods for imaging amyloid in the retina (a curcumin-based stain/ingestion process and immunohistochemistry [35]), and showed evidence of deposits associated with blood vessels. Retinal samples stained with 12F4 mAb showed plaques forming both within and alongside blood vessels, and some examples were shown of plaques formed at branching points. Some deposits are shown in their report with cross-sections

that resemble those in the brain, with the implication that they are generally similar morphologically. Campbell's lab has previously presented several examples of amyloid deposit morphologies in the human retina. Some of this work includes evidence that the deposits have intrinsic birefringence signals [36], and that the deposits have high contrast against the background retina when imaged using polarimetry [37]. These properties suggest a level of order amongst the fibrils that coalesce to form deposits in the retina, which could be consistent with the ordered arrangements of fibrils found using electron tomography of deposits grown in cell cultures [38].

1.6 Theory of Mueller Matrix Polarimetry

To measure the interactions that retinal amyloid deposits and the surrounding tissue have with polarized light, the spatially-resolved Mueller matrix M is calculated for each deposit (equation 1.1). This matrix is a 16-element data array that represents the manner in which different media act upon incident light (with various polarizations):

$$\mathbf{M}(x,y) = \begin{bmatrix} m_{00} & m_{01} & m_{02} & m_{03} \\ m_{10} & m_{11} & m_{12} & m_{13} \\ m_{20} & m_{21} & m_{22} & m_{23} \\ m_{30} & m_{31} & m_{32} & m_{33} \end{bmatrix} \tag{1.1}$$

where m_{ij} denotes the component of the Mueller matrix in the i^{th} row and j^{th} column, and (x,y) denote the horizontal and vertical coordinates of the pixel associated with the particular M. The Mueller matrix can be used to find a variety of polarization signals by representing the incident and exiting light as separate four-element Stokes vectors. Incident light $\vec{S}$ is acted upon by the tissue sample, resulting in an output Stokes vector, $\vec{S}'$ (equation 1.2).

$$\vec{S}' = \mathbf{M}\vec{S} \tag{1.2}$$

A series of mutually exclusive interacting media that each lie along a light path can be denoted by a right-to-left matrix multiplication of the individual Mueller matrices associated with each of the media (i.e. $\mathbf{M} = \mathbf{M}_n\mathbf{M}_{n-1}...\mathbf{M}_2\mathbf{M}_1$). This is the operating principle of the polarimeter. The matrices representing the polarization state generator (PSG) and polarization state analyzer (PSA) are controlled. These components are made of a stationary linear polarizer and a rotating quarter wave plate (see figure 3.4 for ordering). The matrices representing these components, M_{PSG} and M_{PSA}, are both known. The system can then be represented by:

$$\vec{S}' = \mathbf{M}_{PSA}\mathbf{M}_{Sample}\mathbf{M}_{PSG}\vec{S} \tag{1.3}$$

where M_{Sample} is the Mueller matrix associated with a particular position in the sample.

The polarization metrics listed in table 1.1 can each be calculated using the Mueller matrix. All of the metrics with the subscript $_\theta$ represent the angle of the linear component of that polarization property. For example, linear polarizance is calculated from m_{10} and m_{20} and is at the angle $\arctan(m_{20}/m_{10})$. For these calculations, as prepared by Tao Jin [36], the arctangent calculation uses a compensation procedure to ensure that the result is a positive angle. This operation has been omitted from the equations in table 1.1 for brevity.

The linear and circular anisotropy signals, A_L and A_C [41], are defined by presenting $\mathbf{M}$ as:

$$\mathbf{M}(x,y) = m_{00}\begin{bmatrix} 1 & D_1 & D_2 & D_3 \\ P_1 & k_1 & r_3 & -r_2 \\ P_2 & q_3 & k_2 & r_1 \\ P_3 & -q_2 & q_1 & k_3 \end{bmatrix} \tag{1.4}$$

From there, A_L and A_C can be found by letting:

$$\begin{aligned} \alpha_{iD} &= D_i + P_i \\ \alpha_{iR} &= r_i - q_i \end{aligned} \tag{1.5}$$

for $i = [1,3]$. Being that each of the polarization metrics represents a particular interaction between the medium and polarized light, it is understandable that, when represented as a function of two-dimensional position, the metrics show varying levels of contrast between the retinal amyloid deposits and the surrounding retina. Our group has found that R_L gives the strongest contrast[2]. The main analysis in chapter 3 is performed on R_L maps. The R_L map is calculated through a matrix decomposition that writes M as the product of three matrices associated with independent components - a depolarizer M_Δ (which reduces the degree of polarization of incident light), a retarder M_R (which introduces a phase delay between differently polarized components), and a diattenuator M_D (which introduces polarization-dependent attenuation): $M = M_\Delta M_R M_D$ [43]. With M_R calculated, the retardance vector is found by:

$$\vec{R} = \cos^{-1}\left[\frac{tr(\mathbf{M}_R)}{2} - 1\right] \tag{1.6}$$

where $tr(\mathbf{M}_R)$ is the trace of $\mathbf{M}_R$. The first, second, and third elements of $\vec{R}$ are the horizontal, 45^o-linear, and circular retardances [43].

[2] R_L can be approximated with an incomplete polarimeter but this dismisses opportunities to detect potentially superior signals that might require the complete polarimeter.

Metric	Symbol	Formula	Source
a-metric	$A*$	$\frac{2b \cdot t_1}{b^2+t_1^2}$	[39]
b-metric	b	$\frac{m_{11}+m_{22}}{2}$	[39]
t-metric	t	$\frac{1}{2}((m_{11}-m_{22})^2+(m_{12}+m_{21})^2)^{1/2}$	[39]
x-metric	x	$x = \frac{1}{2}\arctan(\frac{m_{20}}{m_{10}})$	[39]
q-metric	q	$\frac{\Sigma_{j=1,k=0}^{3} m_{jk}^2}{\Sigma_{k=0}^{3} m_{0k}^2}$	[40]
Transmission	T	m_{00}	[41]
Depolarization Index	D_I	$(\frac{(\Sigma_{j=0,k=0}^{3} m_{jk}^2)-m_{00}^2}{3m_{00}^2})$	[42]
Depolarization Power	D_P	$1-\frac{\lvert tr(\mathbf{m}_\Delta)\rvert}{3}$ (m_Δ defined below)	[43]
Total Diattenuation	D_T	$(D_L^2+D_C^2)^{1/2}$	[43]
Linear Diattenuation	D_L	$\frac{1}{m_{00}}(m_{01}^2+m_{02}^2)^{1/2}$	[43]
Diattenuation Angle	D_θ	$\arctan(m_{02}/m_{01})$	[43]
Circular Diattenuation	D_C	$\frac{m_{03}}{m_{00}}$	[43]
Total Polarizance	P_T	$(P_L^2+P_C^2)^{1/2}$	[43]
Linear Polarizance	P_L	$\frac{1}{m_{00}}(m_{10}^2+m_{20}^2)^{1/2}$	[43]
Polarizance Angle	P_θ	$\arctan(m_{20}/m_{10})$	[43]
Circular Polarizance	P_C	$\frac{m_{30}}{m_{00}}$	[43]
Total Retardance	R_T	$(R_L^2+R_C^2)^{1/2}$	[43]
Linear Retardance	R_L	$(R_1^2+R_2^2)^{1/2}$ (see below)	[43]
Retardance Angle	R_θ	$\arctan(R_2/R_1)$	[43]
Circular Retardance	R_C	R_3 (see below)	[43]
Total Anisotropy	A_T	$(A_L^2+A_C^2)^{1/2}$	[43]
Linear Anisotropy	A_L	$\sqrt{\frac{(\alpha_{1D}^2+\alpha_{1R}^2+\alpha_{2D}^2+\alpha_{2R}^2)}{\Sigma}}$	[41]
Anisotropy Angle	A_θ	$\arctan(\frac{\alpha_{2D}^2+\alpha_{2R}^2)}{\sqrt{(\alpha_{1D}^2+\alpha_{1R}^2}})$	[41]
Circular Anisotropy	A_C	$\sqrt{\frac{(\alpha_{3D}^2+\alpha_{3R}^2)}{\Sigma}}$	[41]

Table 1.1: Definitions of the polarization signals considered in chapter 3.

1.7 Confocal Scanning Laser Microscopy

Many advancements in biomedical sciences have been due to optical microscopy techniques, and fluorescence techniques in particular. Fluorescence imaging involves exciting a sample with a wavelength of light and then characterizing the radiation emitted by the sample. Early fluorescence microscopes (which were first invented by Heimstädt in 1911[3] [44]) were devoid of means for limiting contributions to signals from planes outside of the desired focal plane. In 1961, Minsky [45] proposed an optical microscope in which a confocal pinhole was implemented. This meant that the fluorescence of different depths within the sample could be viewed in isolation from others. The pinhole removes rays that are generated outside of the object plane, thus greatly reducing noise. Since the pinhole in principle only illuminated a single point on the sample, Minsky's patent also describes an electromechanical system that would move the sample in a scanning pattern.

With the advent of laser technology came the opportunity to reduce the dimensions of the interaction volume, and to have a controlled beam excite particular positions on a sample. Raster scanning mechanisms then allowed for the beam to scan the surface of the sample, instead of moving the sample relative to the point source generated by the pinhole. The use of laser scanning microscopes was proposed in 1974 by Cremer and Cremer [46]. The primitive development of the confocal laser scanning microscope was completed in 1986 [47] and brought with it fundamental improvements to resolution. In its simplest form, the scanning is performed by two spinning reflectors and a laser. Light that has interacted with the sample is descanned and passes into a detector that samples the intensity of the beam. Confocal scanning laser microscopes are typically equipped with multiple lasers, allowing for excitation at different wavelengths, and the recording of different responses from a sample. To manage the output of such a configuration, filters and beam-splitters are used to track the intensities of the exiting signals separately. Many biomedical applications of microscopy involve investigations into samples with three-dimensional variance.

[3] As per [44], Köhler made an ultraviolet microscope in 1904.

Chapter 2

Morphological Properties of Retinal Amyloid Deposits

2.1 Introduction

Alzheimer's Disease (AD) is a neurodegenerative condition associated with accumulation of amyloid in the brain [27, 28]. Other retinal indicators of AD include thinning of the optic nerve fiber layer (ONFL), loss of retinal ganglion cells (RGCs) [48, 49], and changes in vasculature [50, 51, 52]. Research by our group, and others, has confirmed the presence of amyloid in the retina [35, 49, 53, 54, 55, 56]. We are also one of several groups that has specifically found amyloid-β in the retina [35, 49, 56, 57] using immunohistochemistry (IHC). Other groups have concluded that amyloid-β either does not occur in the retina or is not of diagnostic interest for AD [57, 58, 59]. Our group has detected deposits in *ex vivo* human tissue using thioflavin-S fluorescence and label-free polarimetry [37, 60].

Cerebral amyloid angiopathy (CAA) is a condition during which amyloid accumulates in association with vasculature in the brain [33]. Amyloid-β might accumulate initially in the basement membrane of vessels in the brain as a result of a "perivascular drainage pathway" [61]. Deposits associated with CAA take several different forms [33, 62]. These forms include deposits that have banded patterns along their short axis, due to interaction with smooth muscle cells [33], deposits that have filled or replaced a segment of the walls of a vessel [32, 62], and in severe cases, deposits that form within the vessel then disrupt the vessel and continue to form outside of the vessel [63]. CAA deposits can be composed of several different forms of amyloid including amyloid-β, cystatin C amyloid, amyloid prion

protein, transthyretin amyloid, gelsolin amyloid, amyloid Bri(*tish*), amyloid Dan(*ish*), and light-chain amyloid (AL) [61].

There is significant overlap between cases of AD and CAA [31], and it has been reported that higher severity CAA brain pathology is associated with greater retinal loads of amyloid-β [64]. Therefore, the presence of amyloid in retinal vessels [35, 49] in those with CAA would not be surprising. Amyloid-β has been found in AD human retinal vessels using IHC in flat mounts. Amyloid deposits associated with blood vessels may also be connected to previously reported changes in retinal blood vessels associated with AD and/or CAA [50, 51, 52].

Three-dimensional (3D) analysis of amyloid deposits in the brain has been performed in mice and humans [65, 66] using various methods (see [65, 66, 67] for example). Non-vessel related amyloid deposits in brains associated with AD are distinct from those in CAA in that they are commonly isotropic (or spherical) [27]. Based on flat mounted and thin-sectioned retinas, there have been groups that concluded deposits in the retina resemble those found in AD brains [35], and others that did not [57].

This chapter will study the 3D structures of retinal amyloid deposits based on thioflavin-S fluorescence and confocal scanning laser microscopy in *post-mortem* tissue. Comparisons will be made with AD and CAA brain pathology, quantified in *post-mortem* brain pathologies for those individuals who also donated their eyes.

2.2 Methods

2.2.1 Sample Preparation

Human eyes from 25 individuals were donated and collected by the University of British Columbia (UBC) in alignment with the Declaration of Helsinki (pathologies are listed in table 2.1). Of these, nine associated with AD (and/or cerebral amyloid angiopathy, CAA, and/or cerebrovascular disease, CVD), three associated with AD pathology as well as additional conditions, and three associated with non-AD pathologies, were imaged using the confocal microscopy technique (section 2.2.2) for this chapter. Retinas had been prepared for a previous study. They were each separated from the eye *post-mortem*, fixed in 10% formalin, stained with Thioflavin-S for amyloid, and counterstained with 4',6-diamidino-2-phenylindole (DAPI) for nuclear matter. These stains are used for fluorescence imaging. The retinas were then flat-mounted onto glass slides, cover slipped, and sealed to reduce

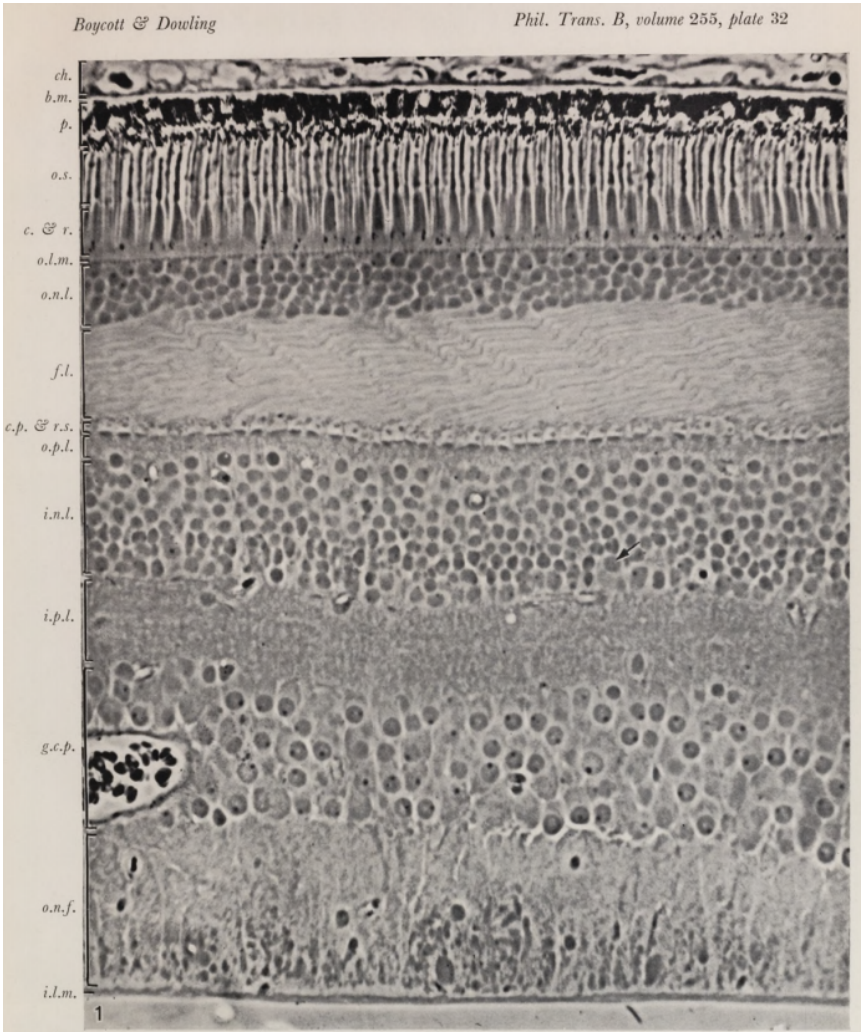

Figure 2.1: Electron micrograph that shows the layers of the human retina, as presented by Boycott and Dowling in 1969, included with permission of The Royal Society [68]. According to the original caption: "the arrow points to a displaced ganglion cell. Magn. x 550. *ch*, choroid; *b.m.*, Bruch's membrane; *p.* pigment epithelium; *o.s.*, outer segments of rods and cones; *c & r*, inner segments of cones (c) and rods (r); *o.l.m.*, outer limiting membrane; *o.n.l.*, outer nuclear layer; *f.l.*, fibre layer; *c.p.*, cone pedicles; rod spherules; *o.p.l.*, outer plexiform layer; *i.n.l.*, inner nuclear layer; *i.p.l.*, inner plexiform layer; *g.c.p.*, ganglion cell perikarya; *o.n.f.*, optic nerve fibre layer; *i.l.m.*, inner limiting membrane. A portion of a blood vessel with erythrocytes shows in the ganglion cell perikaryon layer." The anterior (vitreal) side of the retina is at the bottom of this figure.

Pathologies	Number of retinas	Number of retinas used in this chapter
AD (possibly including additional pathologies of CAA and/or CVD)	15	9
MSA	1	1
DLB, CVD	1	1
DLB, AD	2	2
PSP	1	1
ALS	1	0
FTLD-TDP	2	0
AD, DLB, TDP, HS, CVD, CAA	1	1
FTLD-TDP, ALS-TDP, NFT (Braak III), age-related tau astrogliopathy	1	0
TOTALS	**25**	**15**

Table 2.1: Number of retinas with particular sets of pathologies. CAA → cerebral amyloid angiopathy, CVD → cerebrovascular disease, MSA → multiple system atrophy, DLB → dementia with Lewy bodies, PSP → progressive supranuclear palsy, ALS → amyotrophic lateral sclerosis, TDP → transactive response deoxyribonucleic acid-binding protein 43, FTLD-TDP → frontotemporal lobular degeneration - TDP, HS → hippocampal sclerosis, NFT → neurofibrillary tangles.

dehydration and the presence of contaminants. These samples were also previously imaged using polarimetry, as discussed in section 3.2.4 in chapter 3. Brain pathologies were determined *post-mortem* by a neuropathologist based on the NIA-AA guidelines [69].

2.2.2 Confocal Scanning Laser Microscopy

Retinal slides were imaged using the Zeiss LSM 700 confocal scanning laser microscope (CSLM). Samples were mounted with their cover slips facing downwards toward the objectives. Using the `Smart Setup` option in Zen (designed by Zeiss for operation with CSLM), DAPI and fluorescein isothiocyanate (FITC) channels were selected and the separation of detection windows was preset. The FITC channel was used to image Thioflavin-S, which was excited at 488 nm, and fluoresces at 510 nm. DAPI is optimally excited at 360 nm and fluoresces at 460 nm [70]. The DAPI channel used in this work was excited with a laser at 405 nm which only accounts for a small portion of the possible excitation spectrum. The emission for the channel was broad and appears to give weaker fluorescent labelling to the nuclear material as compared to results attained with another CSLM in the past. This is not a major concern since the FITC channels contain the deposit signals. These

two channels were collected for each selected deposit (see figure 2.2). In spite of the configuration of the DAPI channel, detail in the retinal surround is visible to an extent that made identification of cellular structures possible. Small tile scans across the samples were performed after focusing on a layer near the anterior retina to look for deposits. Once a deposit was found, the Zen software was used to set the range of depth over which slices would be captured, and the confocality was set to a single Airy unit (to reduce the impact of fluorescence from outside of the desired image plane). These image planes correspond to z-slices, which are images taken at different depths along a direction normal to the retinal sample. The Range Indicator mode was used to ensure that gains for individual detector channels were as bright as possible without saturating the image.

The planar dimensions of each 512x512 image were set based on the voxel size of 0.44 μm and imaged with a 20X objective. This led to slices that were approximately 225 μm x 225 μm, unless noted as otherwise. To ensure that voxels were cubic, the axial separation of the z-slices was also set 0.44 μm. This set the number of slices taken in each stack. The number of slices and range of depth were both calibrated for each deposit so as to fully enclose all slices in which the deposit signal was visible. Image stacks were collected as a sequential raster scan across the plane for each z value. This process of detecting plaques in (x,y,z) and collecting image stacks was applied to multiple deposits in each of the 15 retinas analyzed in this chapter. The deposits were selected arbitrarily from those in the anterior layers of the retina. Over 100 deposits were imaged in this way, mostly including deposits that were presumably associated with retinal blood vessels, and a lesser quantity of deposits that were not. The structural properties of these two groups of deposits are discussed and then compared in this chapter. No conscious effort was made to image deposits with particular features or structures. The depth from the anterior surface of the retina that can be imaged on the CSLM is limited to between 50 and 100 μm. The 3D structures of these deposits were observed using Zen, as were cross-sectional cuts.

2.3 Results

2.3.1 Deposits Presumably Associated with Blood Vessels

Recently, work has been performed within our lab to characterize the difference between deposits that are associated with blood vessels and those that are not. Blood vessels were of low contrast but visible as long dim paths through the imaged fields, in some cases with presumed red blood cells visible within. The vessel-associated deposits can be further categorized as those outside but touching the vessel, and those within vessels. Some

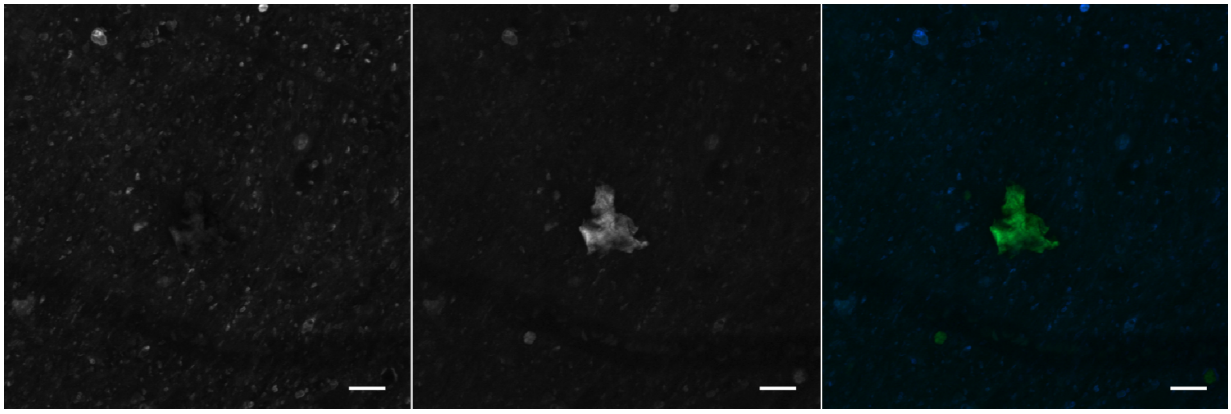

Figure 2.2: Split-view of slice 20 in a z-stack for a deposit; left-right: DAPI, FITC, combined and coloured; scale bar is 20 μm.

deposits presumably between layers in the vessel walls resemble the banded structure of deposits previously found in a mouse model of CAA (figure 2.12). The morphologies of these vessel associated deposits are described below in detail.

Deposits Possibly Filling Vessel Walls

Long deposits with elliptical cross-sections, that in at least one case had a hollow core (figure 2.3), were observed. These are possibly blood vessels whose walls are filled with amyloid, as has been reported in the human brain [32, 62]. The deposit in figure 2.4 displays a particularly interesting property in which the long deposit connects to a presumed vessel, but does not itself appear to have any sort of bounding vasculature running along its length and beyond. Both the deposit and the lower branches of the vessel in this slice are of similar widths, so this deposit has possibly formed in the vessel and closed off the branch it accumulated within, equivalent to some form of amyloid clot. However, it has been hypothesized that amyloid is associated with a repair response in the brain [71], so the vasculature may have been damaged through some other means. In either case, this deposit appears to have a solid elliptical cross-section, implying that it perhaps filled the lumen of the vessel, but it also has some textural features along its outermost surface that may be consistent with those found in vessel walls. Hence, the deposit in figure 2.4 may have accumulated in both the wall and lumen of a vessel.

Several of the deposits which might be filling vessels (or vessel walls) have tattered ends (figures 2.4 and 2.5), described as such because they resemble a rope that has become

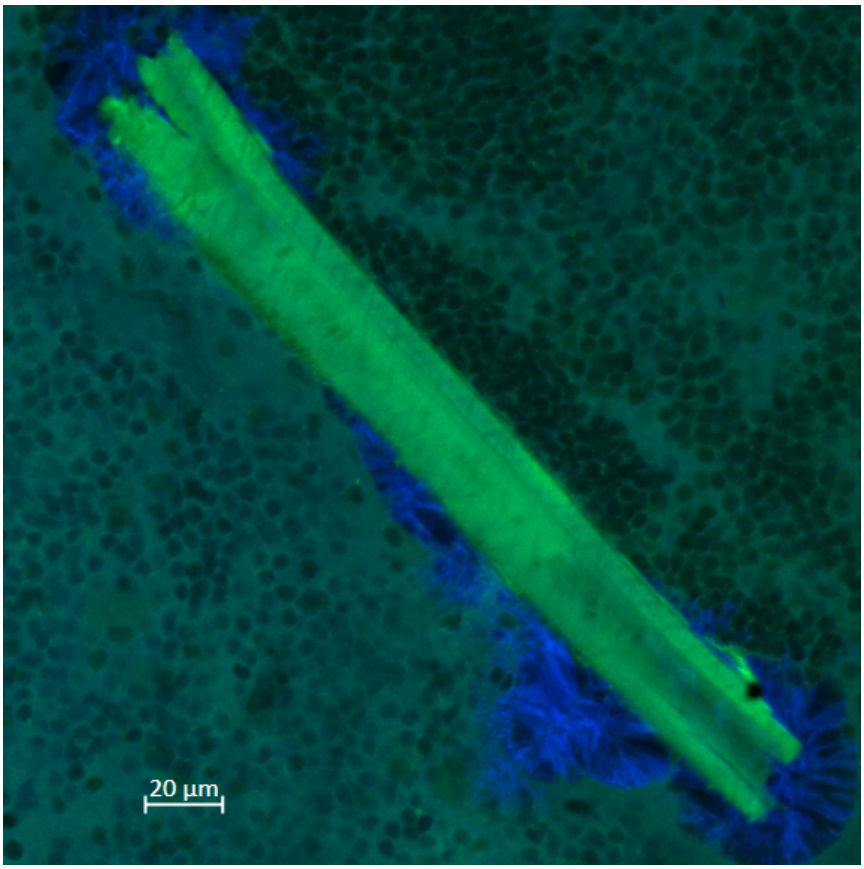

(a) *En face* slice

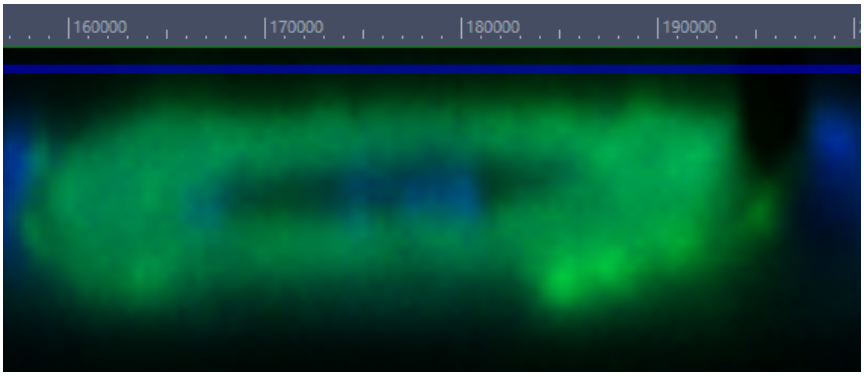

(b) Orthogonal cut (xz-plane), scale in nanometers.

Figure 2.3: A z-slice and orthogonal cut of a long and hollow deposit, presumably filling the walls of a blood vessel.

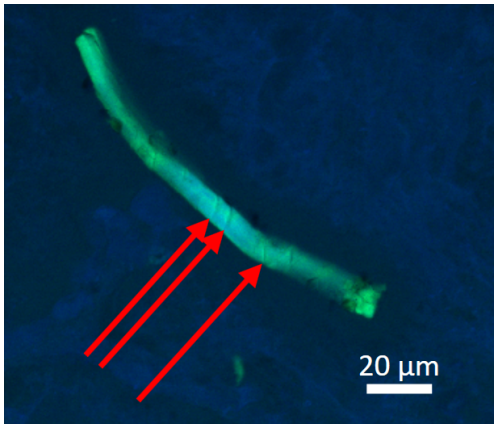

(a) Slice 29: Red arrows indicate locations of several grooves that are likely hallmarks of smooth muscle within the vessel wall.

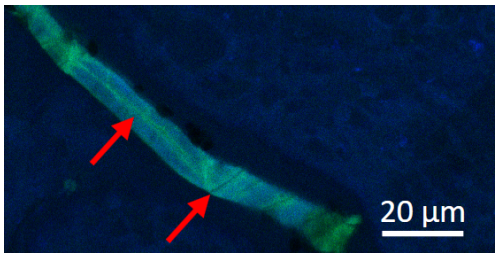

(b) Slice 72: Red arrows indicate grooves, and a strip of amyloid through the center of the deposit (100X objective).

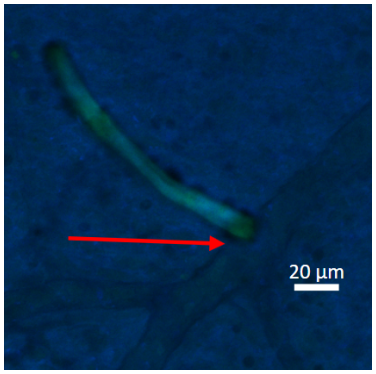

(c) Slice 43: Red arrow indicates vasculature that the deposit connects with.

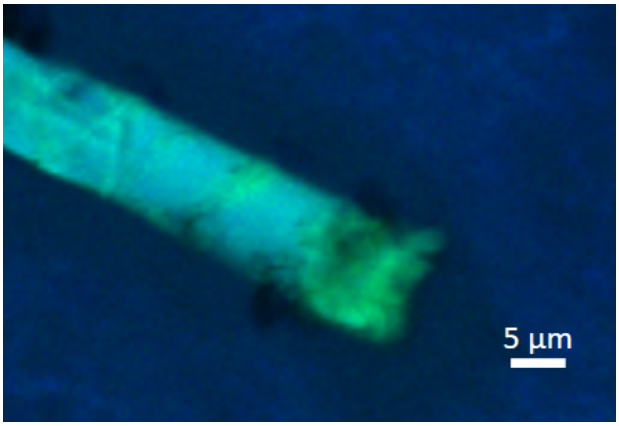

(d) Slice 33: Enlarged region around tattered end of the deposit, where it connects to another presumed vessel.

Figure 2.4: A long vessel associated deposit, with labelled features.

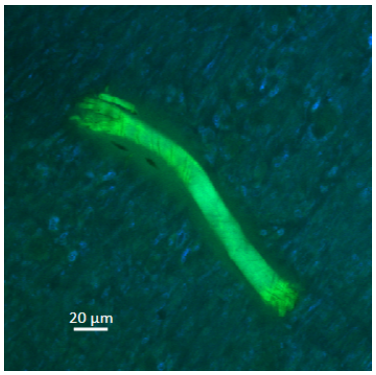

(a) Slice 24

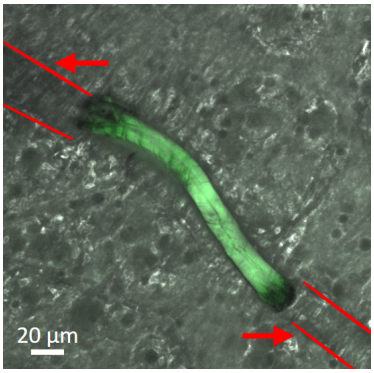

(b) Slice 30

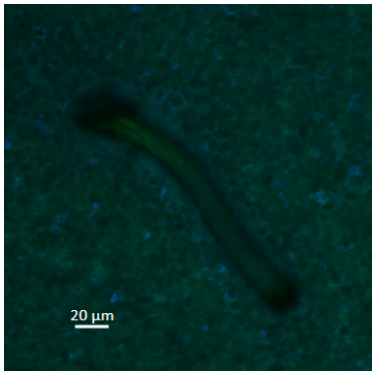

(c) Slice 47

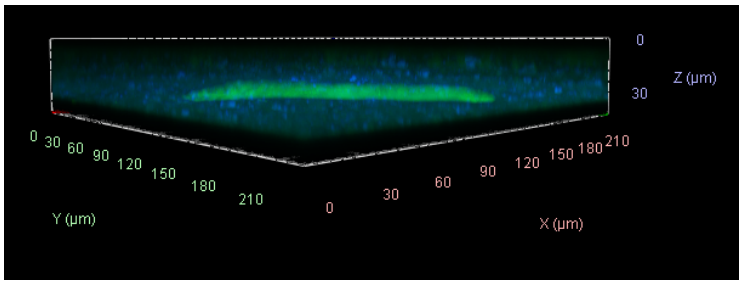

(d) Oblique perspective of 3D volume. Note the levelness of the deposit and the slight slant at its ends, and that 2.5b has been artificially contrasted and false coloured to highlight a presumed vessel.

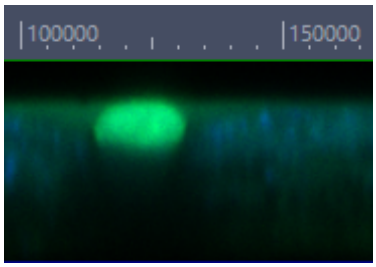

(e) Orthogonal cross-section of the deposit; scale in nanometers.

Figure 2.5: Selected slices from a z-stack of a long deposit with grooves, tattered ends, and likely filling a segment of a blood vessel. This deposit was found in a retina that was not associated with AD brain pathology or cerebral amyloid angiopathy. The only listed pathology was multiple system atrophy (MSA).

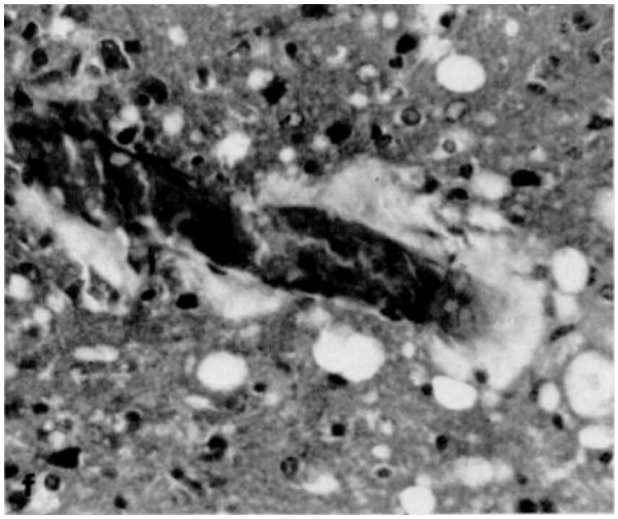

Figure 2.6: A blood vessel in a mouse brain with amyloid along its edges and seemingly running in a line through the lumen, included with permission of Wiley, based on work performed by Bruce and Fraser [18].

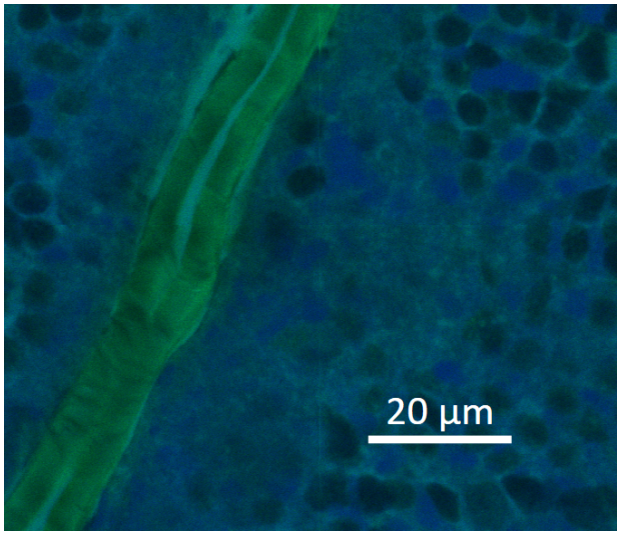

(a) Slice 43

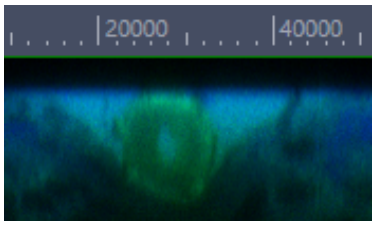

(b) Orthogonal Cut showing xz-plane, scale in nanometers.

Figure 2.7: A long deposit that appears to have formed within a vessel wall and partially filled the lumen.

frayed. The roughness of these ends might further support this hypothesized link to ruptured or damaged vasculature. The fringing of the amyloid off the ends of the segment of the presumed vessel partly resembles a vessel fringed with amyloid that was reported in [18]. See figure 2.6 for an example from [18] that has been included with permission of the publisher. Note that the deposit in figure 2.5 was from the retina of a subject that had MSA but no evidence of AD or CAA brain pathologies.

The regions surrounding the deposit in figure 2.3a has virtually no signal in the FITC channel and is in plane with the deposit, making it unlikely that it is due to some optical shadowing. This may be an indication of tissue degradation.

Large deposits with elliptical cross-sections commonly have grooves, oriented at some acute angle to the short axis of the deposit. This might indicate interaction with smooth muscle along the vasculature, or an artifact from the way in which the amyloid is aligning in this large tubular structure. These deposits occasionally have wrinkles or crevices (figure 2.8a) which are visually consistent with the reconstructed image of an amyloid-β laden leptomeningeal vessel (APP23 mouse brain) in [72] (figure 2.8b, Copyright 2001 Society of Neuroscience).

In some of the cylindrical deposits within vessels, the lumen is partially empty, but in other cases, another feature that stained with thioflavin-S ran coaxially within the deposit and may have indicated amyloid within the lumen (see figures 2.4b and 2.7 for instance). The cross-section shown in figure 2.7b appears to show amyloid within the vessel wall, and then also filling the lumen, but notably the colour profiles of the two features are different. This may be indicative that the amyloid in and around the wall of the vessel fluoresced based on excitation at the FITC wavelength, and that the amyloid presumably within the lumen was potentially auto-fluorescing primarily based on the DAPI excitation. This may further indicate that amyloid aggregates of different stages or maturities, as reported by [21], accumulated within the different regions of the vessel. Their study used hypersensitive fluorescent amyloid markers to demonstrate that different structures of amyloid-β could be found within individual deposits, corresponding to different structural maturities of the deposit. See figure 1.1 for an image of theirs taken within a transgenic mouse model of AD [21, 22].

A Deposit within a Possibly Twist-Buckled Vessel

A presumably vessel associated deposit with a spiral-like feature in its cross-section is shown in figure 2.9. The slight fold in the deposit at the approximate location of x=250 μm and y=180 μm could be a retinal case of vascular twist buckling [73, 74], which is a class of tortuous vessels. The presence of tortuous vessels in the brain in association with ageing has been well documented (see the review in [75]). The deposit appears to be within

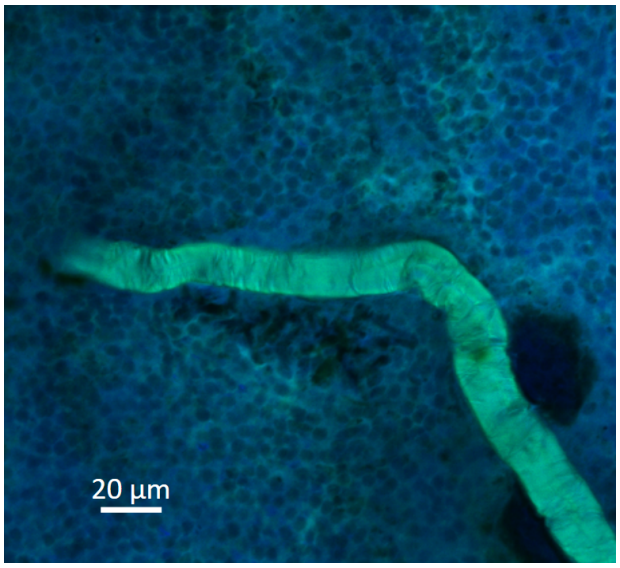

(a) A slice in a z-stack containing a deposit that is presumably filling a vessel, and has the appearance of wrinkles across its surface.

(b) A leptomeningeal vessel in a mouse brain that has stained for amyloid-β with similar wrinkles, scale bar represents 25 μm. Copyright 2001 Society for Neuroscience [72].

Figure 2.8: A retinal amyloid deposit with an apparently wrinkled surface is shown in 2.8a, which seems to resemble an amyloid-β-positive leptomeningeal vessel in a mouse brain shown in 2.8b [72] (Copyright 2001 Society for Neuroscience) [72].

a vessel and to join a presumed vessel along the right side of the field. In the orthogonal cuts through the stack (figure 2.9b), the curled region closes in on itself; the other portion of the deposit is shaped like an ellipse that is pinched at one end. Otherwise, the deposit is similar to the deposits with elliptical cross-sections described earlier. In the orthogonal cross-sections, it further appears that the deposit is not within the vessel lumen, implying that this deposit is between layers in a vessel wall.

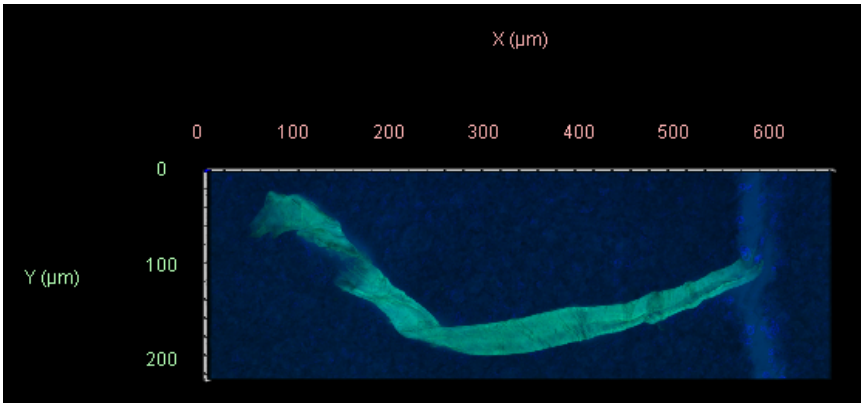

(a) 3D view of the *en face* projection

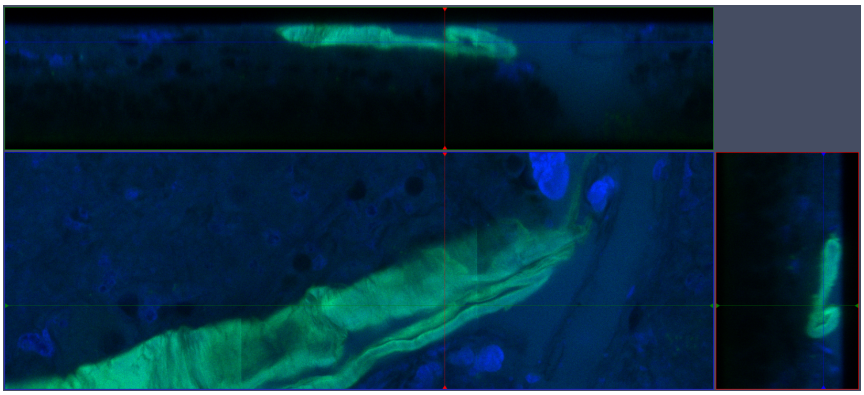

(b) Orthogonal cuts, based on a z-stack captured with the 100X objective (voxels 0.13μm x 0.13μm x 0.14μm)

Figure 2.9: A large deposit within the walls of a presumably tortuous vessel that has a rolled structure, curling along its short axis.

Micron-Sized Dark Spots within Vessel Walls

A possibly vessel-associated deposit was found (see figure 2.10) which has a series of dark spots periodically spaced across it. The sizes of the spots in this image are also

consistent (roughly 0.9-1.8μm), but the shapes of the patterned dark spots change with depth. It is plausible that the dark spots are the result of amyloid accumulating in the outer walls of a vessel. In the lower right portion of the deposit, corresponding to the cross-section in figure 2.10c, the dark spots appear to travel through the deposit. Long deposits with elliptical ring-like cross-sections, like that shown in figure 2.10c, are consistent with amyloid filling the walls of vessels, as occurs in the human brain [32, 62]. At the opposite end of the deposit, the cross-section does not have a cavity, suggesting that the vessel in which this deposit has formed may have closed off as a result of the deposition. The deposits in figures 2.11a, 2.11d, and 2.11f, also have dark spots. These spots may be indicative of cellular structures close to the outermost layer of the vessel wall.

Deposits with Banded Patterns

Deposits with banded patterns were observed in the human retina. See figure 2.11a for an example of one such deposit, which appears to have formed in the wall of a vessel but does not fully wrap around the vessel. The bands resemble those found in CAA deposits in the brain, and in mouse models (figure 2.12 [26]). In CAA deposits in the brain, these bands reportedly form due to amyloid displacing smooth muscle cells in the vessel wall [26, 33], so it is possible that the pattern described here has an equivalent cause. Note that the deposit in figure 2.11a has less distinct bands.

Several other deposits with bands, or dark spots (discussed above) are in figures 2.11d and 2.11f. Further efforts, which have already been initiated by other members of the group, will involve staining for vasculature, which will likely allow for more definitive explanations of the banded patterns in the flat retinal amyloid deposits. With the information currently available, and the visual similarities to deposits present in animal models of CAA, it seems plausible that the banded deposits are vessel-associated, and that the pattern is related to the displacement of smooth muscle cells by amyloid deposits.

Possible Examples of Dyshoric Changes

In brains affected by CAA, amyloid that accumulates within vessels can in severe cases disrupt the vasculature and continue to form in the region outside of the vessel [63]. This section contains descriptions of several deposits that were found in the space immediately outside of vessels, touching the external surface of the vessel wall in some cases, and deposits that appeared to have possibly initially formed within vessels and then continued to form in the region immediately outside the vessel.

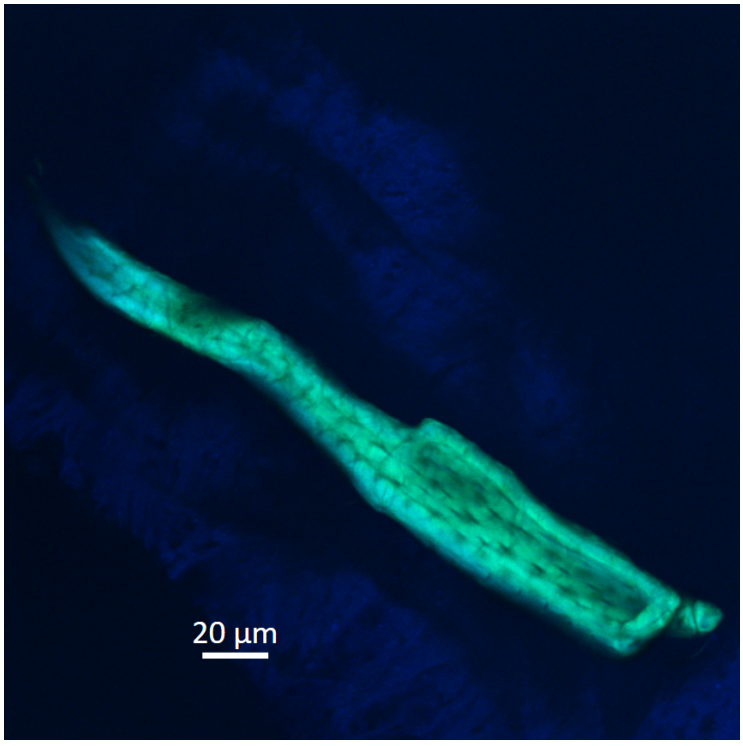

(a) Slice 24

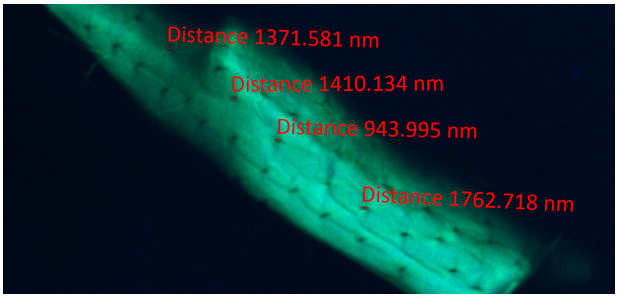

(b) Slice 15

(c) Orthogonal cross-section showing the xz-plane; scale in nanometers.

Figure 2.10: Slices and an orthogonal cross-section in a z-stack with measurements of the diameters of dark spots that are spaced very regularly through a deposit that appears to fill the walls of a vessel. Note that the measurements in 2.10b are for the dark spots directly below the letter *D* in "distance", for each of the four measurements shown. The cross-section illustrates that the dark spot go through the deposit.

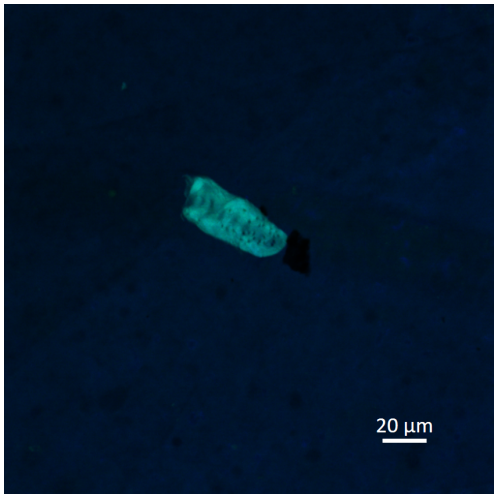

(a) Slice 32

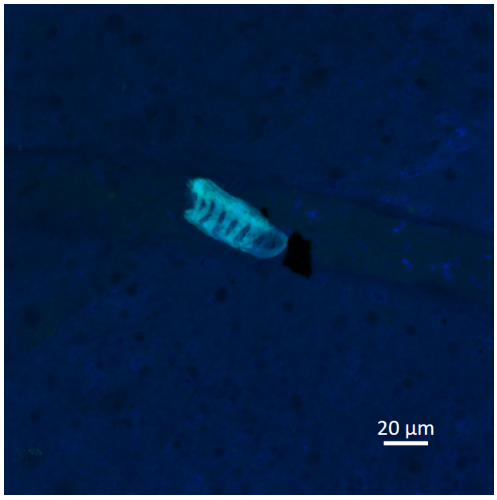

(b) Slice 36

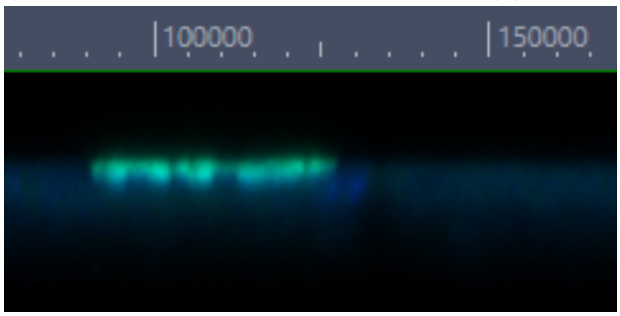

(c) Orthogonal cross-section of the deposit in 2.11a and 2.11b, showing the xz-plane; scale in nanometers.

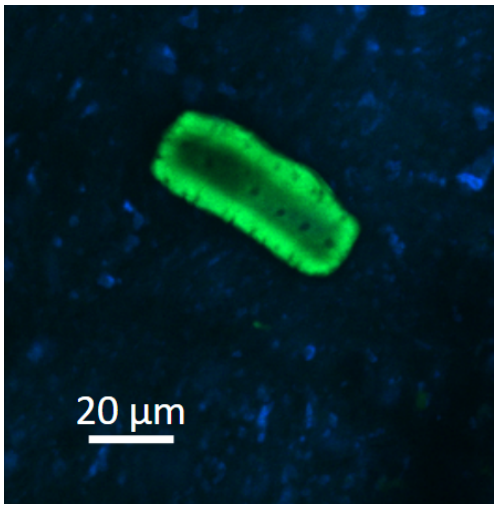

(d) Slice 25

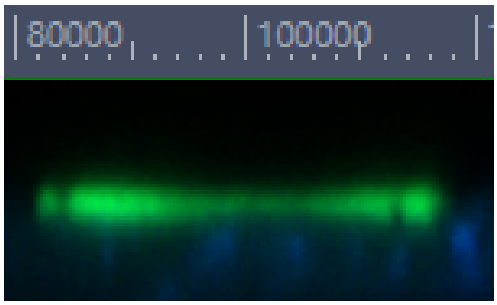

(e) Orthogonal cross-section of 2.11d showing the xz-plane; scale in nanometers.

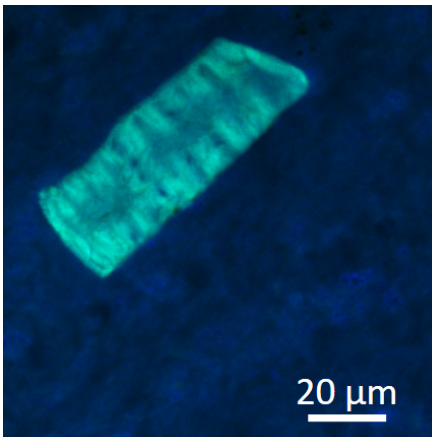

(f) Slice 44 in a deposit with a weaker signal running along its center, and a banded pattern periodically spaced along its long axis.

(g) Orthogonal cross-section of 2.11f showing the xz-plane; scale in nanometers.

Figure 2.11: Flat deposits that are presumably within vessel walls. Note that the deposits in 2.11d and 2.11f were not clearly found within a vessel wall but the similarities in their morphologies to the deposit in 2.11a which was found in a vessel wall, make it likely that these other deposits formed through similar mechanisms.

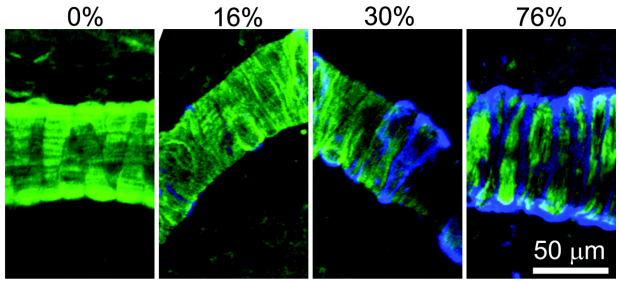

Figure 2.12: 2-Photon images of vasculature affected by cerebral amyloid angiopathy in transgenic mice (green → vascular smooth muscle cells; blue → amyloid deposition), included with permission of Wolters Kluwer Health, Inc. [26].

A Deposit that Bends Around a Vessel A deposit that is thin in the z-direction but not parallel to the *en face* plane is shown in figure 2.13. This deposit has multiple bends, including its central bend that appears to be around some sort of vasculature. It is not precisely clear whether the deposit makes direct contact with the vessel beneath due to a shadow that appears to have been cast by the deposit, but it is possible that this deposit started within the walls of said vessel and then spread into the surrounding retinal tissue.

A Folded Deposit Touching the Outside of a Capillary The deposit shown in figure 2.14 appears to lie on top of a vessel. The deposit has two folds, labelled with red arrows in figure 2.14a. As in figure 2.14b, the different features of the deposit appear to be very thin in the z-direction. This folded deposit appears to be located above a capillary that joins the major vasculature in the field (see figure 2.15).

Several other possibly vessel associated deposits contain a mixture of morphologies which may be indicative of dyshoric changes in the retina. For instance, a deposit was found that has a long and flat structure, with a nearly transparent thin feature that partially wraps around one of its ends (see figure 2.16). Other deposits of this mixed morphology include those in figures 3.26a and 2.17b. Differing morphologies in a single deposit might indicate a coalescing of multiple adjacent deposits, or differential tissue densities that lead to growth being restricted in particular directions. The layered structure of the retina is likely a determining factor in the tendency of most retinal amyloid deposits to be thin relative to their lateral dimensions, as opposed to amyloid deposits in the brain which are commonly spherical. Some additional retinal deposit structures like those in figures 2.16 and 2.17 could result from a deposit that initially forms in vasculature and then escapes (through a rupture or micro-aneurysm [76], for example) and continues to grow in the adjacent cellular tissue. This would be analogous to dyshoric changes that occur in CAA [63]. Note that the deposit in figure 2.16 does not have any clear vasculature in the field,

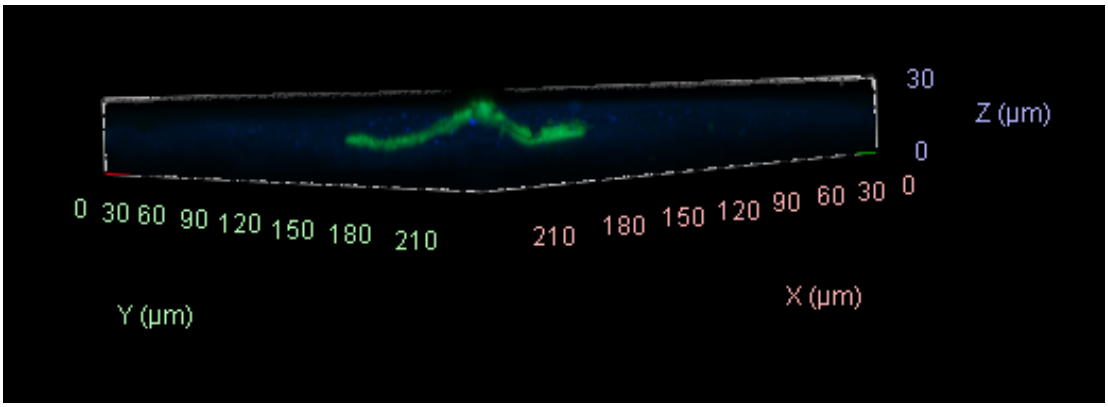

(a) 3D oblique view

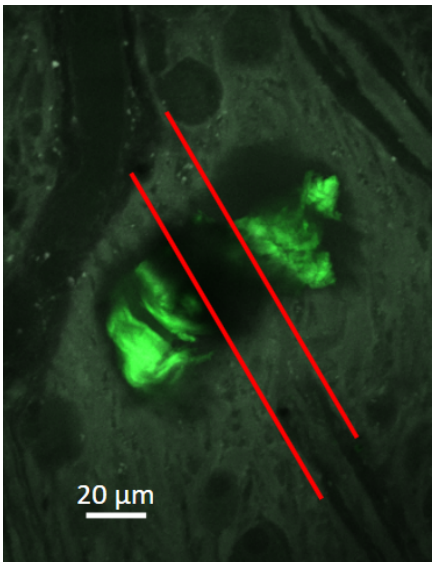

(b) Slice 44

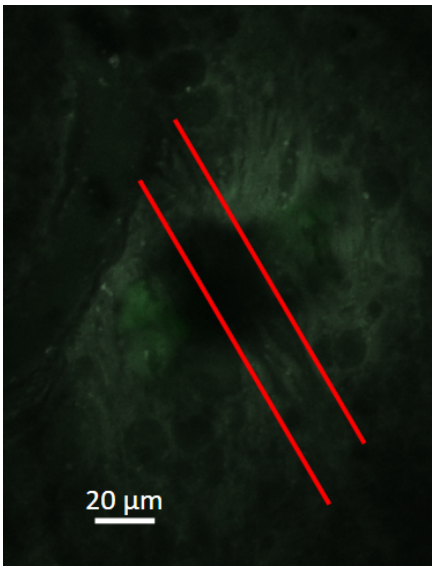

(c) Slice 59

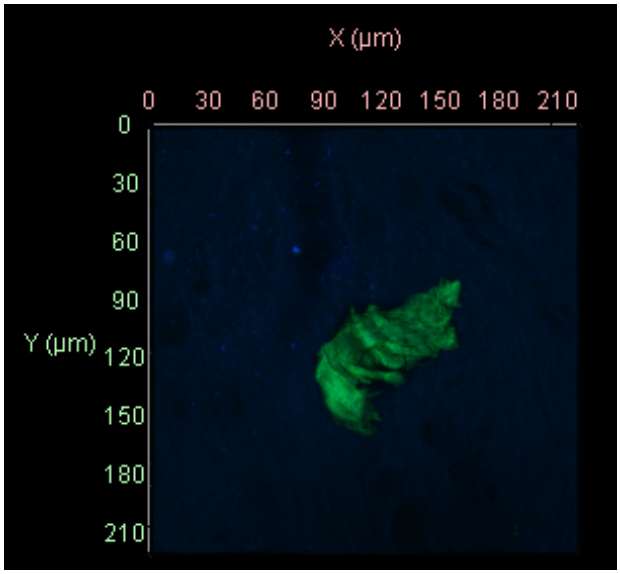

(d) 3D *en face* view.

Figure 2.13: Multiple 3D perspectives and z-slices of a deposit that appears to bend around a vessel, and the surrounding tissue. In 2.13b and 2.13c, the DAPI channel has been false coloured as white, which causes the deposit to appear brighter, and red lines indicate lateral boundaries of the presumed vessel running beneath the deposit.

(a) Slice 30: Folds indicated by red arrows

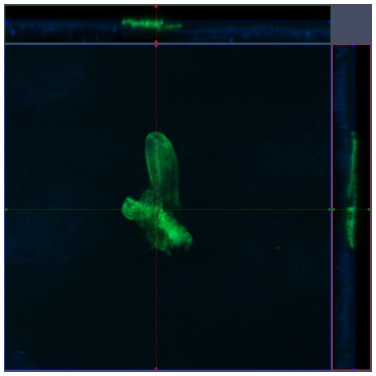

(b) Orthogonal cut to illustrate the flatness of the individual features of the deposit

Figure 2.14: A deposit with multiple folds within ≈ 2.5 μm of presumed vasculature and possibly touching it.

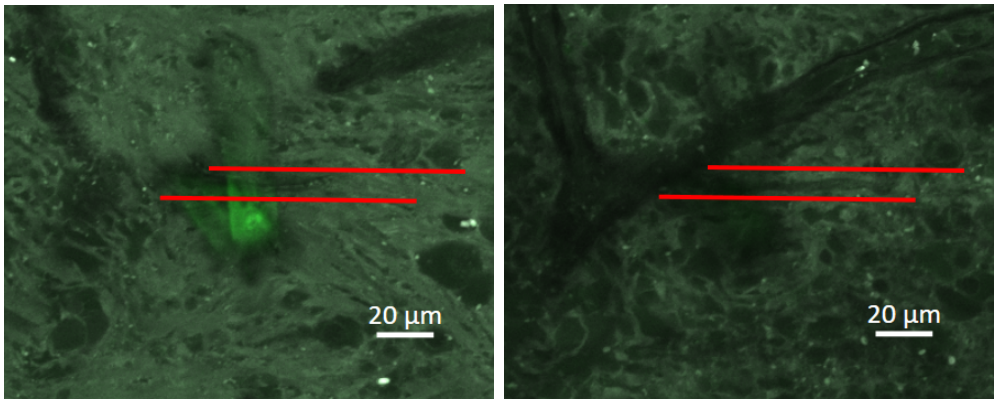

(a) Slice 38 (b) Slice 47

Figure 2.15: Two slices from the z-stack associated with the deposit shown in figure 2.14, with the field enlarged to display a possible capillary. The position of the capillary is between the red lines. The "crease" of fold B appears to connect to the capillary, though the remainder of the deposit appears to lie several microns above (i.e. more anterior than) the indicated capillary. Note that the DAPI channels were set to white to make the capillary more visible.

but does have a long flat structure, with possible banding, indicating that it may have formed within the wall of a vessel. The feature near the center of the figure appears to wrap partly around the long flat feature. The example in figure 2.17 appears to connect to a vessel (at a point indicated by the red arrow) and has features that are of widths similar to that of the vasculature in the field.

2.3.2 Images of Possible Fibrillar Bundles

Within a large number of deposits imaged using the CSLM, strands of Thioflavin-s positive features can be found (see figure 2.18). Typically, these strands are detected near the anterior side of the deposit. Measurements of these features in deposits from various retinas, imaged by several individuals, range from approximately 0.75-1.5μm[1]. This is within approximation of the broad range of fibrillar bundle sizes proposed in [77]. One possible explanation for the fibrillar strands being found on the anterior-most faces of the deposits could be that they are forming from the anterior direction, piling on layers like

[1]When imaged using a 100X objective, it was possible to see such presumed bundles with diameters less than 0.4 μm.

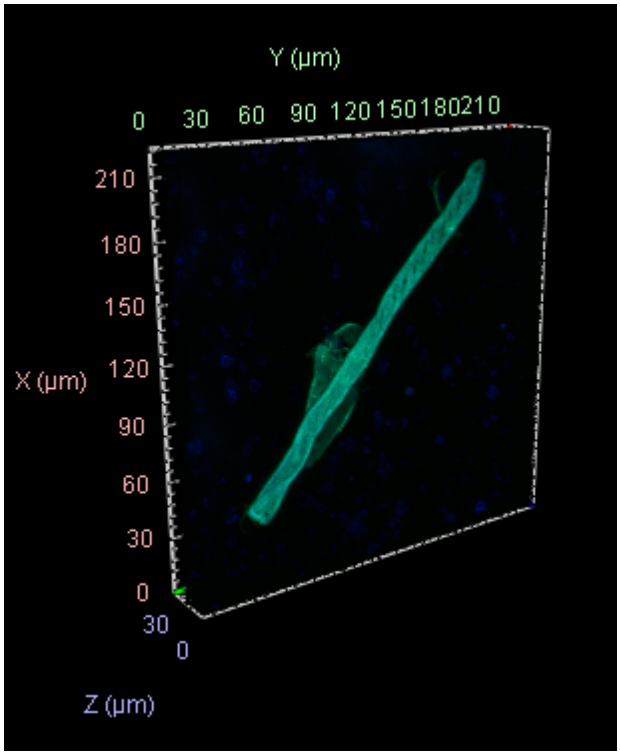

Figure 2.16: Oblique 3D view of a long flat (non-tubular) deposit, and a thinner feature wrapped around it.

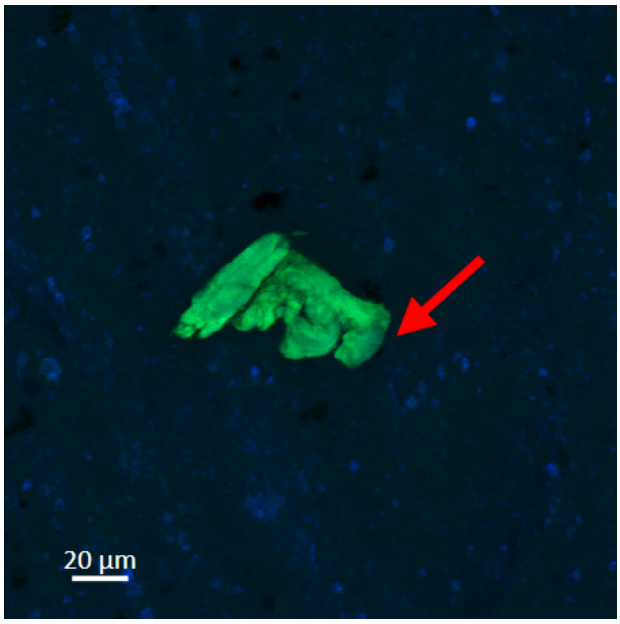

(a) Slice 20

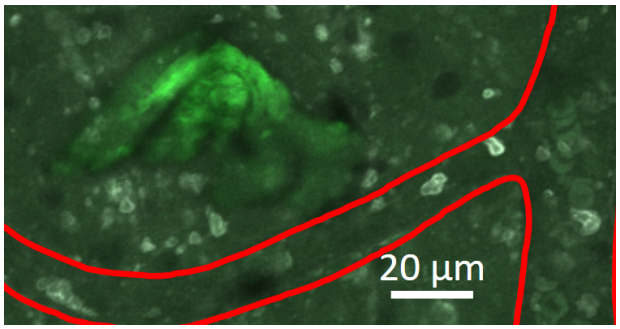

(b) Slice 27

Figure 2.17: Slices from a z-stack containing a deposit with a structure composed of several different morphological features, that appears to connect to vasculature, and may be an example of a dyshoric changes. The red arrow in 2.17a points to where the deposit appears to join the vasculature. The red lines in 2.17b indicate the position of the presumed vessel walls in the field, and the DAPI channel in 2.17b has been set to white to make the vessel more visible.

the formation of an amyloid mesh. A study by Wright *et al* found that levels of amyloid (Aβ-40, Aβ-42) and (t)Tau proteins in the vitreous of the retina were lower in human subjects with lower cognitive performance [78]. This might indicate that these proteins are evacuated out of the vitreous into the retina. In that case it would be logical that some deposits form from the anterior retinal surface downwards and that the deposits least packed features are closest to the anterior retina. A deposit was found in a retina seemingly in the ONFL, with a strand-like feature near its anterior surface, which seems to further support this hypothesis of amyloid deposition from the vitreous into the retina.

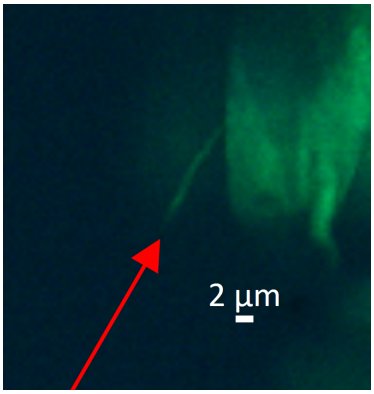

Figure 2.18: A small subsection of a deposit highlighting a feature that is possibly a bundle of amyloid fibrils.

2.3.3 Retinal Amyloid Deposits Unrelated to Vasculature

There were deposits imaged in this analysis that neither appeared in close proximity to a presumed vessel, nor had structural features that resembled vessel-associated deposits. See figures 2.19-2.21 for examples. The retinas in which the deposits in this section were found were from subjects with AD brain pathologies. One feature that can be observed in the 3D structure of several non-vessel related deposits is that of dark spots that in some cases (see figure 2.19) appear to move laterally across slices with depth. Two spots in particular, labelled by a red arrow, shift apparent position between slices, and eventually merge. In a 3D perspective, this would be visually similar to a Y-shaped dark tunnel through the deposit. Figure 3.26b illustrates several other regions that have these shifting dark spots, in the same deposit.

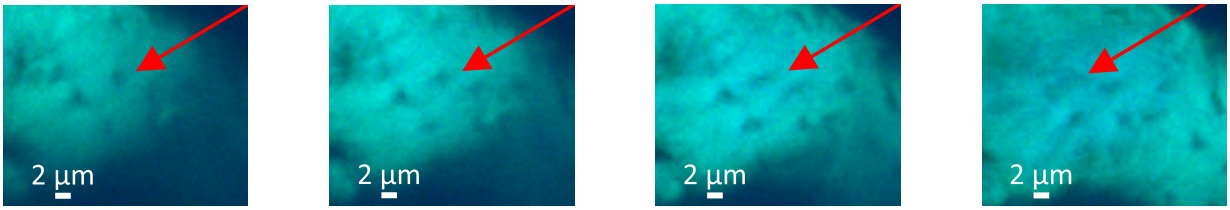

(a) Slice 46 (b) Slice 48 (c) Slice 50 (d) Slice 54

Figure 2.19: Different z-slices in a deposit that illustrate the displacement of the dark spots at the end of the red arrow.

A theory put forth by a member of our group, Steven Esau, is that these shifting dark spots are created by RGC axons. The shift in the position of such dark spots could be indicative of the manner in which the accumulation of amyloid displaces the presumed axons. The deposit in which the dark spots in figure 2.19 were found, appeared to have some regions that were possibly composed of periodically arranged fibrillar bundles of amyloid (see figure B.1 in Appendix B), so the dark spots may be equivalent to the axons pushing between these arranged bundles. Electron microscopy images found RGC axons have diameters more than covering the range of 0.5μm to 5μm [79], encompassing the range of sizes of the shifting dark spots. The proximity of the deposits to the anterior most layers in the retina, and the sizes of the dark spots, all seem to support the connection to RGC axons.

Similar to the deposit shown in figure 2.19, the deposit in figure 2.20a appears to have dark spots. A small region within figure 2.20a is shown in figure 2.20b, which more clearly displays said dark spots, which appear to lie a few microns above the presumed RGCs in figure 2.20c. Figure 2.20d shows another deposit with a dark spot in its center of roughly 3 μm diameter, and seems to align laterally a few microns below a possible RGC (see the orthogonal cross-section in figure 2.20e). These examples of deposits with dark spots seem to support the argument that dark spots in deposits unrelated to vessels are due to RGC axons.

Among the retinal deposits imaged for this chapter, the deposit in figure 2.21a is perhaps the closest to being circular in cross-section. Most other deposits are not close to spherical (see figure 2.21b), having larger dimensions in a retinal plane than their perpendicular thickness. The small size of the more spherical deposit in figure 2.21a, coupled with the fact that its thickness is not greater than that seen in the other "flat" deposits, might suggest that such deposits initially grow axially only by a small amount before growing laterally. Generally, the non-vessel associated deposits were relatively thin, with overall

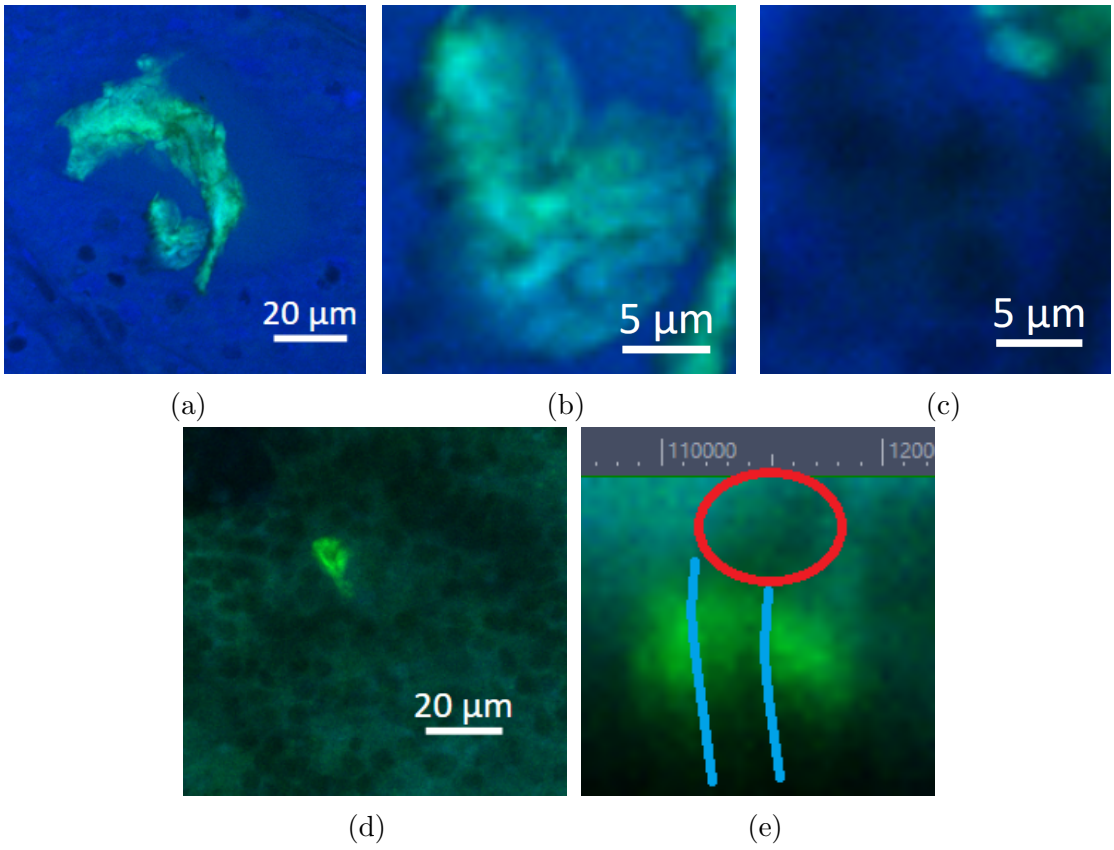

Figure 2.20: Additional deposits with dark spots that do not appear to be related to vasculature. Images are *en face* slices within z-stacks unless otherwise specified from a subject with AD brain pathology and Congo Red-positive (CRP) CAA in the frontal cortex (FC). 2.20a: a deposit that does not appear to be vessel-associated; 2.20b: Cropped region of slice 17 in 2.20a showing dark spots in the deposit; 2.20c: Cropped region of slice 28 in 2.20a, showing possible RGCs below the dark spots in 2.20b; 2.20d: Shows a dark spot within a fluorescent area; 2.20e: Orthogonal cut through 2.20d, showing a dimmer region in the deposit which corresponds to the dark spot in 2.20d (between bright blue lines). This is directly below a presumed RGC (large dark spot in red circle); scale in nanometers.

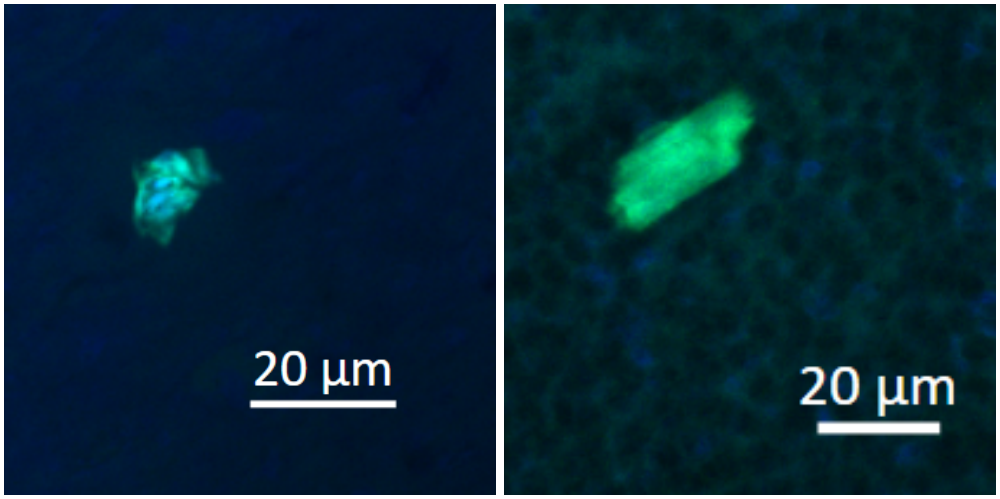

(a) (b)

Figure 2.21: Slices through retinal deposits that do not appear to be related to vasculature.

thicknesses of around 5 μm and 25 μm, respectively.

2.4 Discussion

2.4.1 Limitations of Methods

Several aspects of the procedure have noteworthy limitations. The practical limit of depth resolution as per Abbe's law is $2\lambda/NA^2$, where λ is the excitation wavelength, and NA is numerical aperture. Most z-stacks studied for this chapter were imaged using a 20X objective with NA=0.8, so with the FITC excitation wavelength at 488 nm, the axial resolution limit would have been approximately 1.5 μm, which is roughly three times the separation between consecutive z-slices. As a consequence, structures in neighbouring z-slices would not be resolved.

Presumption of vasculature within a field was made based on varying extents of apparent contrast in the retinal surround. Several of the features that have been described in this chapter as resembling those found in CAA were observed both in z-stacks that had a presumed vessel in the field and in z-stacks that did not. This likely reflects the limited capacity for vascular contrast, rather than a non-specificity of the presumably CAA-like deposit features to vessel associated deposits in the retina.

Over 100 deposit z-stacks from 15 retinas were considered for this analysis. The 100 deposits studied were located within 15 retinas each of which had between 12 and 89 amyloid deposits, for a total of over 500 deposits. Thus, this work does not give insight into the proportions of deposits with particular morphologies. Brain pathology was performed at UBC in accordance with NIA-AA guidelines [69]. These assessments include scores associated with various proteinopathies, and the overall severity of CAA and AD pathologies. CAA pathology is assessed in the frontal cortex using Congo Red, and in the hippocampus and cerebellum using IHC (amyloid-β). CAA has been reported in other regions of the brain [80], so subjects whose pathology did not include CAA in our data may still have had it in other regions of the brain.

In this chapter, the group of retinas that had AD included some that had one or both of CAA and CVD. As described in more detail below, there is substantial coincidence of subjects that have AD and CAA pathologies, and both are associated with amyloid-β. AD associated retinas that had CVD were also included as CVD is not associated with a proteinopathy. However, CVD is commonly caused by atherosclerosis [81] which involves arterial cholesterol-based plaques [82], and retinal changes in vasculature might be linked to those in the brain associated with CVD [83]. Crystalline cholesterol-laden deposits in vessel walls can reportedly produce polarization signals [84]. Although cholesterol has not been reported as thioflavin-S positive, there have been reports of co-localization of thioflavin-S positive amyloid signals and cholesterol in a mouse model of AD, suggesting some plaques may contain both amyloid and cholesterol. This is not likely to have been the case in this study as the vessel associated deposits observed herein did not appear patchy or otherwise discontinuous.

2.4.2 Vessel Associated Deposits and the Severity of Cerebral Amyloid Angiopathy in the Brain

In the brain, CAA deposits are typically described as those that form within vessels, and those associated with dyshoric changes which lead to amyloid deposits adjacent to vasculature [80]. Here, amyloid-laden deposits were classified as vessel-associated if they were found within a vessel or touching the external surface of the vessel. Vessel associated deposits were found in all nine retinas that had evidence of both AD and CAA brain pathologies with CAA severity scored as 1-3 (i.e. mild to severe). In addition, vessel associated deposits were found in all three retinas that had AD brain pathology but no CAA pathology. Presumably vessel associated deposits (figure 2.5) were found in a retina of a subject with no AD or CAA pathology (pathology noted was MSA), appearing to fill the

walls of a vessel and possibly the cavity within as well. It has previously been suggested that, in association with AD, amyloid deposits in the retina may occur prior to their occurrence in the brain [55]. Our group has previously found that the number of amyloid deposits in the retina predicts the severity of AD pathology in the brain [54]. Another group studying retinal tissue, donated by some of the same patients whose donated tissue was analyzed by our group, has reported that the total load of amyloid-β in the human retina was higher in those with more advanced CAA pathologies [64]. Our results here indicate that pathology of a CAA type in the retina may occur prior to its occurrence in the brain.

2.4.3 Comparison of Vessel-Associated Deposits in the Retina and Deposits Found in Cerebral Amyloid Angiopathy in the Brain

This chapter studied fluorescence images of retinal amyloid deposits that formed in some relation to presumed blood vessels. Several similarities between these deposits and those that have been reported in CAA were noted. There were multiple instances of deposits that appeared to have elliptical cross-sections which may have filled vessels, and other cases in which deposits had ring-like cross-sections, possibly indicating vessel walls that had been filled with amyloid. Some have reported that amyloid can fully replace sections of vessels in later stages CAA deposition [32, 62], so this effect of deposits filling vessel cavities and/or vessel walls might indicate a progressed form of CAA-like deposits within the retina.

Multiple deposits had a banded pattern, and at least one example of such a deposit appeared to form atop a vessel. Deposits with banded patterns have been reported in CAA [33, 26] with pattern reportedly due to amyloid displacing smooth muscle cells in the vessel. One difference between banded deposits found in CAA and those in the retina appears to be that banded deposits in CAA seem to wrap completely around the vessel, whereas no example of a banded deposits that also had a ring-like hollow cross-section was found in this analysis. This might be a reflection of the small sample size, but could also imply that the source of amyloid involved in retinal banded deposits comes from layers anterior to the vessels involved, and deposits atop the vessels as a result.

Other deposits were found to be connected to vessels but did not seem to have structures that resembled any cellular feature of the vessel. Deposits connected to vasculature peripherally have also been reported in CAA and tend to form at sites of damage [63]. In one case, a long deposit was found that was narrower in half of its length than in the other

half. Through cross-sectional analysis, the narrower end appears to have an effectively filled in elliptical shape, whereas the broader end has a ring-like cross-section. This may have been the result of amyloid accumulating in a vessel and progressively reducing flow through the region until eventually blocking flow altogether.

At least two deposits connected to presumed vessels had folded morphologies. It is possible that the fold in figure 2.9 is due to amyloidosis of a vessel that had undergone twist buckling [74]. Another example of a deposit with a folded morphology (imaged by **MK**) was found to connect at one end to a presumed vessel, and cross-sections of said deposit appear hollow. This deposit might therefore be an amyloid-laden segment of a vessel that has branched off from the nearby presumed vessel, which had also perhaps undergone some sort of twisting.

Thioflavin-S staining labels all amyloids (with beta-sheet structures) in the flat mounted retinal samples. This may explain why some deposits described here appeared to fill blood-vessels or their walls with a less patchy appearance than those found by Koronyo *et al* when using a stain specific to amyloid-β 1-42 [35]. This indicates that the deposits analyzed in this chapter might be composed of a mixture of amyloids. It has been reported that though both amyloid-β 1-40 and 1-42 occur in CAA in the brain, the 1-40 sequence is more common in general CAA, and the 1-42 sequence is associated with capillary CAA [63].

2.4.4 Comparison of Vessel-Associated and Non-Vessel-Associated Deposits Found in Retinas

Much fewer deposits unrelated to retinal vasculature were included in this study than those presumably related to retinal vasculature. Our group's previous work on retinal amyloid deposits has included analysis of deposits unrelated to retinal vasculature and those found in this study appear to be morphologically similar to those that have been reported in the past (in the *en face* perspective).

Comparison of Vessel and Non-Vessel-Associated Morphologies

Most deposits imaged for this chapter were thin in the *en face* (axial) direction, compared to their extents in the lateral directions. Brain deposits are commonly reported as being spherical or isotropic, which is possibly due to the relatively uniform density of brain tissue on the size scale of deposits. Conversely, the largely two-dimensional layeredness of the retina may explain why many deposits found therein appear flat and parallel to the arrangement of layers. Deposits in blood-vessels are typically elongated, having shapes and

curvatures seemingly mimicking that of the vasculature they are formed within. Some elongated deposits have previously been found by our group in the ONFL, with morphologies possibly due to the deposition forcing apart striations in the ONFL. Generally, deposits not associated with retinal vasculature or the ONFL take on a wide variety of morphologies.

The thicknesses of non-vessel associated deposit are likely constrained by the closely packed, highly ordered layers of the retina. The deposits are thus flattened and parallel to the arrangement of layers. This is in contrast to amyloid deposits in the brain which are commonly reported as being spherical or isotropic, likely due to the relatively uniform density of brain tissue which encourages isotropic growth.

Strand-like features, corresponding in size to bundles of amyloid fibrils, were imaged on the outside of deposits from both deposit categories. This may be indicative of a stage in deposit growth that is common between the two groups. Although some features of the correct dimensions were resolved (see figure 2.18 for an example), presumed bundles of fibrillar amyloid were not routinely observed within the bulks of deposits, likely due to the limits of resolution inherent in the imaging method.

2.4.5 Conclusions

Structural similarities between retinal blood-vessel associated deposits and those found in the brain in association with CAA, studied here using 3D rendered confocal z-stacks, may indicate that the retinal deposits form through mechanisms analogous to those associated with CAA in the brain. The presence of CAA-like deposits in the retinas of subjects that did not have any CAA reported in brain pathology suggests that such deposits may form in the retina before in the brain, or that their formation/presence is less connected to AD than CAA is.

Future Work

Our group is actively pursuing novel means of investigating the orderedness of deposits on a fibrillar level, led to the electron tomography project, described in section 4.4. Other future work in the optical regime could involve staining for particular amyloids to repeat an investigation similar to that which has been performed here in 3D using confocal microscopy, to determine which amyloids are associated with particular morphologies of deposits in the retina.

Chapter 3

Multifractal Analysis of Retinal Amyloid Deposits

3.1 Introduction

Amyloid deposits in the human retina have many morphologies (chapter 2). Deposit structures can vary with depth, and are presumably influenced by the environment in which they form. This chapter focuses on quantitatively characterizing the complexity and texture of deposits as a function of the pathological conditions they are associated with and, in the case of Alzheimer's Disease (AD), the severity of the disease. The severity of AD brain pathology correlates to total count of deposits [54]. Whether retinal amyloid deposits associated with different severities of AD have different structures has not yet been demonstrated.

AD is a neurological disease associated with neurodegeneration, and most specifically the loss and/or death of neural cells ([49, 85]). Amyloid-laden deposits in the neural (anterior) layers of the retina are likely associated with AD (see figure 2.1 for an electron micrograph that displays the layers of the human retina [68]). Other deposits with polarization signals seem to exist in the retina, but are found below the anterior layers in the non-neural (posterior) retina. These deposits might be associated with age-related macular degeneration (AMD), as amyloid has been found in drusen ([86, 87]). Drusen are deposits that form between the retinal pigment epithelium and Bruch's layer of the retina, perhaps in response to damage and inflammation caused by AMD [88]. Another group studied drusen in *ex vivo* retinas from some of the same subjects whose retinas have been analyzed by our group [89]. That group found that the number of intermediate hard drusen was

higher in the temporal retinas of those with AD compared to normal older adults [89], and postulated that drusen could be used to diagnose AD. Another *post mortem* study has suggested that the occurence and severity of AMD is no higher in those with AD than in those in aged-matched controls [90]. Our group wanted to test the hypothesis that deposits in the neural (anterior) layers of the retina and those in the posterior retina have different properties. Members of Campbell's lab have previously noted that deposits deeper in the retina more commonly have well-defined borders and structures than deposits in the anterior retina, when imaged using polarimetry.

Using machine learning, Nunes *et al* detected textural differences in retinal tissue in subjects with AD, Parkinson's Disease and those without pathology, based on images captured with optical coherence tomography [91]. Pirici *et al* demonstrated that the fractal dimension, a numerical measure of complexity, differentiated between: plaques in brains associated with AD from those within healthy controls; and diffuse plaques from other types [34]. Similar texture and complexity-based differences might exist for retinal amyloid deposits and the nearby tissue in association with different pathologies.

Generally speaking, fractal analysis is considered a means of describing objects that are meaningfully described by dimensions between the traditional first, second and third (topological) dimensions [34, 92]. For instance, consider an infinitesimally thin piece of paper. While that paper is flat and unaltered, it is likely well described (for most reasonable scales) as a plane with topological dimension 2. Technically speaking, this infinitesimally thin sheet would still have topological dimension 2 if it were crumpled and folded in any number of ways. This highlights a case in which the topological dimensions would not differ but clearly the crumpled sheet represents a more complicated or rougher surface. The fractal dimension of such a surface would likely be higher than it would be for the unaltered sheet as a result of this comparatively higher complexity.

Fractal analysis, which normally uses a box-counting method to estimate fractal dimension[1], can reportedly produce different results[2] using different computational precisions or estimation techniques [95]. Traditional box-counting estimates of fractal dimension are based on several assumptions [93, 94], including that the structure of the set (or image, as the case may be) is at least "statistically" self-similar at all scales. This would imply that the object may not be an exact replica of itself at different scales, but instead may have similar levels of roughness.

[1] The reason for its popularity, its advantages, and weaknesses, are described at length in [93, 94].

[2] The authors mention that their findings indicated the different results were still consistent.

3.1.1 Theory of Multifractal Analysis

Multifractal analysis (MFA) of images has been shown to require fewer assumptions than basic (*mono*)fractal analysis, allowing for the complexity or so-called roughness to change in different ways at different scales, and is useful in a variety of applications. The method represents the global roughness or dimension of an image as a function of the local properties [96] or "singularities" [97], and results in a spectrum as opposed to a single value, known as the multifractal spectrum (MFS). This gives a descriptive means for quantifying the complexity and texture [98] in an image. MFA is suited for identifying edges [98] and describing complexity in biomedical images (see [99, 100], for examples). The majority of this chapter focuses on MFA for distinguishing between retinal amyloid-laden deposits associated with different pathologies.

The process begins by measuring some aspect of an image (known as a "capacity") in regions around each pixel. The change in the measurement as a function of the region size is represented by a Hölder exponent α. These α label singularities within the image [97], based on some capacity. The value of α is calculated for each pixel, generating a Hölder image, or Hölder exponent map. The choice of capacity used in calculating α leads to differently contrasted features as each is sensitive to particular types of singularities. See figure 3.1 for Hölder images generated based on the same initial image using various capacities [101]. For the capacity labelled maximum (hereafter shorthanded as *max*), used in this chapter, the greatest value in the region of size ϵ is determined, making *max* suited for images with intensity-based contrast.

The Hölder image generated by calculating *max* can be thought of as a puzzle with each piece being a subset of the original image that all have the same α. For each such piece, the Hausdorff dimension is calculated (described below). This dimension is similar to the traditional fractal dimension and can be thought of as a means of describing the roughness of the piece. The MFA process thereby calculates a type of global complexity-linked dimension for each of the different local types of textures distributed within the image, generating a spectrum, known as a Hausdorff spectrum or more generally as an MFS.

The Hausdorff dimension of a point is zero, a line is one, and so on [103, 104]. The sets of interest are those that lie somewhere between lines and squares. The Hausdorff dimension of a set is fairly complicated to calculate and the precise approach is described elsewhere [105] and below.

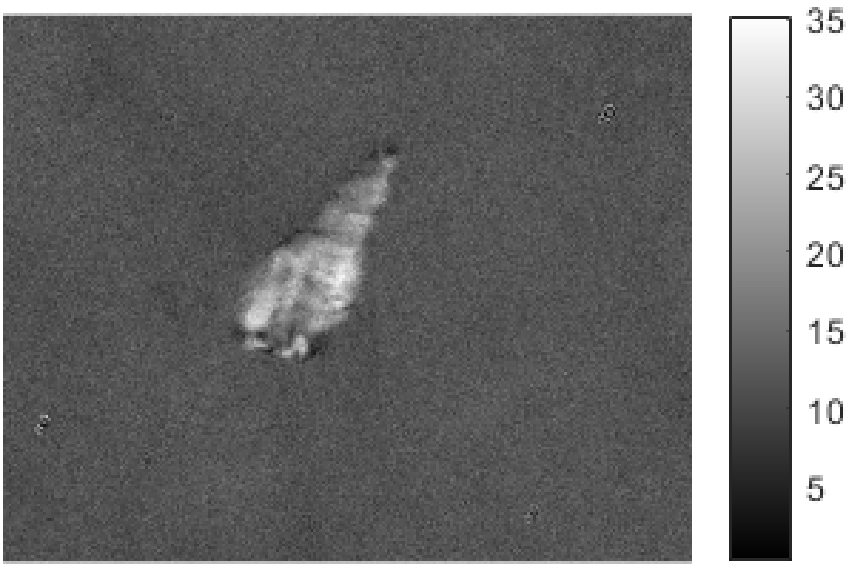

(a) R_L map, scale in degrees

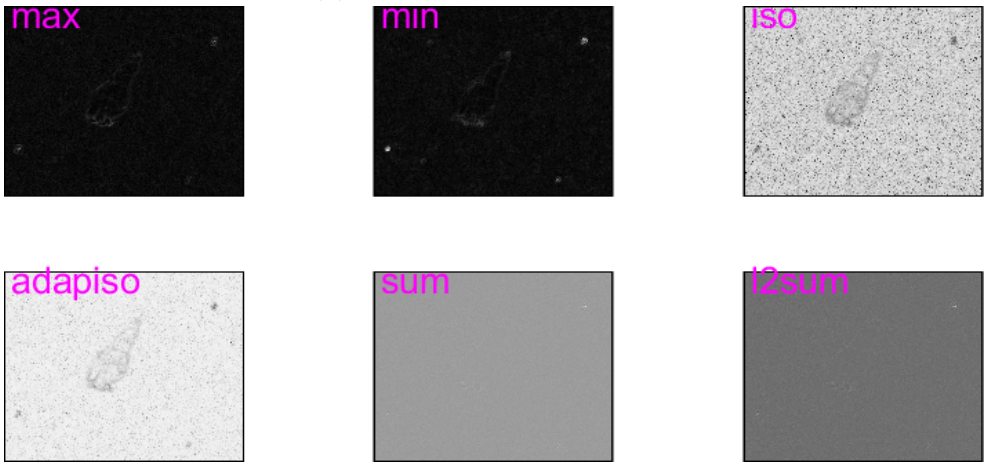

(b) Hölder exponent maps

Figure 3.1: Hölder exponents maps for the main capacities included with the Matlab plugin FracLab by Lévy-Véhel *et al* [101, 102]. From these Hölder exponent maps, the MFS is calculated by determining the Hausdorff dimension for the subset of the map with a particular Hölder exponent value.

Multifractal Spectra and Related Metrics

This chapter makes use of a suite of functions written for Matlab by Lévy-Véhel *et al*, collectively called FracLab [101, 102]. The method used in estimating the Hausdorff dimension in FracLab is not explicitly stated in the plugin's documentation but the authors have confirmed that their Hausdorff dimension calculation is based on the method in [105]. Others have cited [106] but this resource is not readily available for review. FracLab has been cited for its use in many applications, including breast cancer anomaly detection and segmentation [100, 107] and characterization of the maternal placenta surface [99]. Comparisons of different MFSs can be helpful in finding quantitative means of describing differences [99, 108]. The following statements outline the premise behind the calculation of the Hausdorff dimension, as per [105], for an arbitrary object. To calculate the Hausdorff dimension, one begins by considering some countable (finite) balls that can cover the object without overlap. There is an upper limit on the size s of balls that can be chosen, but not a lower limit. The lowest value for the sum of the diameters U of the n balls (when the upper limit of s is set to ∞), raised to some power q, is the Hausdorff content H_s^q (equation 3.1 [105]).

$$H_s^q = inf\{\sum_i^n |U_i|^q\} \tag{3.1}$$

where *inf* means to take the infinum of the sum, which in this context is effectively the minimum - the smallest sum of q^{th} powers of U_i for a countable cover of the object. For a particular s, the Hausdorff dimension is the value of q at which H_s^q switches from infinite to zero and is labelled herein as F. For q below the Hausdorff dimension, H_s^q is infinite, and for q above the Hausdorff dimension, H_s^q is 0. This is similar to trying to measure some quantity with a tool that is "thicker" or "thinner" than the object for which the measurement is taken [109] (i.e. the length or volume of a square). In such a case, since $F = 2$ for a square [110], one would find that the $q = 1$ Hausdorff content of a square is infinite, and the $q = 3$ Hausdorff content of a square is zero. Sets fully contained in two-dimensions with more intricacy or complexity tend to have greater F, and are within a range spanning from the Hausdorff dimension of a point to that of a square, or equivalently $0 < F < 2$.

The Hausdorff spectrum is calculated in FracLab by estimating F of the subset of an image covered by pixels with each unique Hölder exponent. FracLab groups all of the values into one of fifty evenly spaced bins in the inclusive range between the highest and lowest nonzero Hölder exponent values. The positions associated with pixels whose values are within a particular bin are treated as a mask. The F is calculated for this mask and then stored as the value of the spectrum at that particular bin of α. Consider figure 3.2.

The α map associated with the *max* measurement has been binned, and the value at each point is replaced by F, to illustrate which types of image features correspond to particular F. The final MFS is a plot of F against α, representing the relationship between the local and global properties of the image.

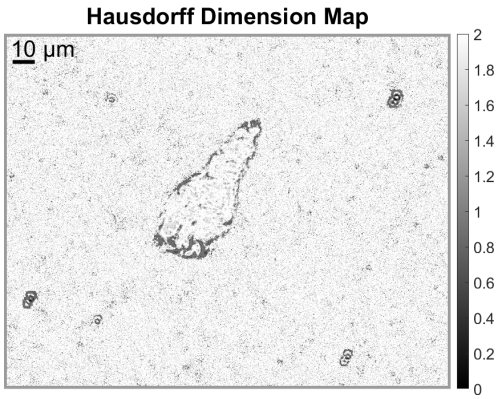

Figure 3.2: Map of Hausdorff dimensions. These values are calculated by binning the Hölder exponent map and then each pixel's value is set to the F that is calculated for the subset of the image that it belongs to, calculated using $Hvec$: 1:2:17, $Svec_{min}$ of 1, and the *max* capacity (defined in section 3.1.2).

3.1.2 Practical Multifractal Analysis of Images

Hölder Images, and MFS Peak-Related Metrics

In describing the multifractal properties of an image, it is first necessary to select a measure μ. Some μ which can be chosen are known as Choquet capacities. These capacities can be evaluated for a box of any size for a gray-scale image. Choquet capacities are always increasing and regular [102] (e.g. the value found for the Choquet capacity, *max*, should never decrease with larger regions, and remains regular). To calculate the Hölder exponents, the *max* within a growing region around a pixel in an image was evaluated. For some predetermined complete set $Hvec$ (as in *Vec*tor of *H*ölder exponent region sizes) of odd-numbered lengths in a range, square regions of each individual length ϵ are centered around a particular pixel and then *max* is measured within each region. Let the smallest and largest box lengths be $Hvec_{min}$ and $Hvec_{max}$, respectively. The overall set of box lengths can then be written as in equation 3.2, where the syntax $a : b : c$ is interpreted as

the values in the range between a and c incremented by steps of size b. See figure 3.3 for an illustration of how max could be applied. In this figure, size represents ϵ.

$$Hvec = Hvec_{min} : 2 : Hvec_{max} \tag{3.2}$$

After max has been calculated for each region around a particular pixel, the natural logarithms of max are plotted against the natural logarithms of the region sizes. This is used to model the power-law relationship between the measurement within the regions and the sizes of the regions. A linear regression is used to estimate α [111]:

$$\alpha = \frac{log(\mu(\epsilon))}{log(\epsilon)} \tag{3.3}$$

where α is the Hölder exponent at that pixel's position. When the plot of $log(\mu(\epsilon))$ versus $log(\epsilon)$ is poorly modelled by a linear trend, some inaccuracies may occur. In other box-counting estimates of fractal dimension, the presumption of self-similarity leads to a region within which a power-law relationship is only evaluated within the region in the log-log plot that is most linear. No attempt was made in this chapter to directly detect the region within the α-determining plot that is most linear before performing the regression. Some tests were performed by varying the upper and lower bounds on the region size ϵ to control the information used in the local calculation. These Hölder exponents are the x-axis of the MFS, and the Hausdorff dimensions provide the y-axis.

In addition to MFA, this chapter will briefly describe results related to tests involving another popular measure of complexity in image analysis, entropy. The entropy E of an image I is given (in Matlab [112]) by:

$$E(I) = -\sum p_i log_2 p_i \tag{3.4}$$

where p_i is the probability of the i^{th} binned value in the image's histogram. E is a measure of texture and variability across I [113].

3.1.3 Live-Eye Imaging Consideration

Our group is actively collaborating with our industry partners to develop a live-eye imaging device, a confocal scanning laser ophthalmoscope equipped with polarimetry. The polarization-sensitive scan will allow for the detection and counting of deposits by their polarization signals. Resolution in such a live-eye scan cannot be improved much beyond

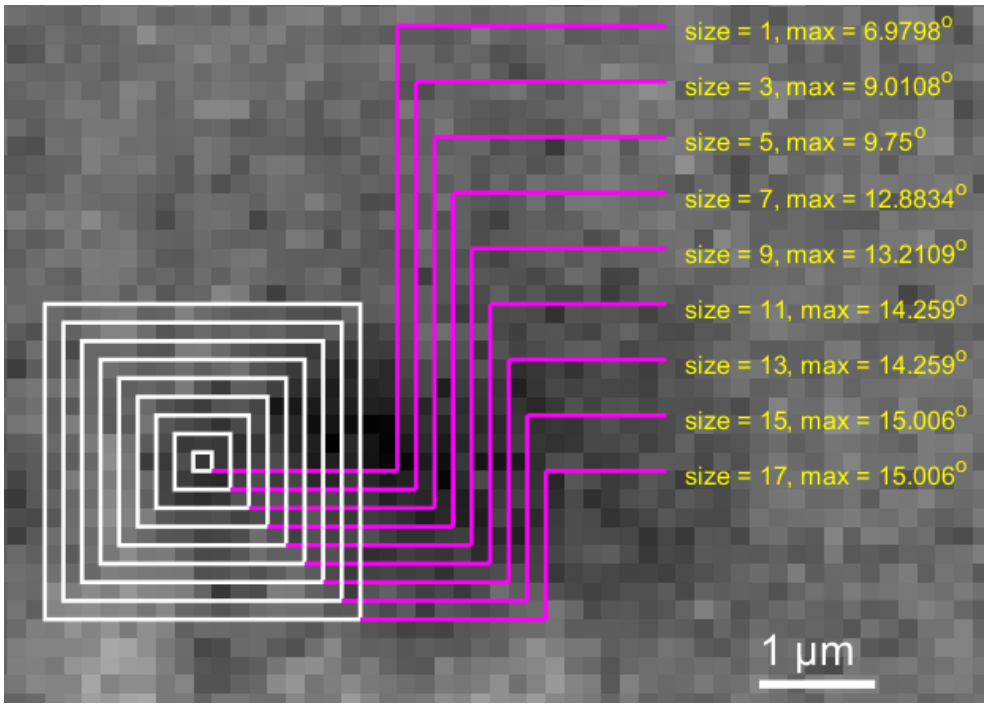

(a) Illustration of a sample α calculation, based on the *max* capacity, for a pixel in a R_L map.

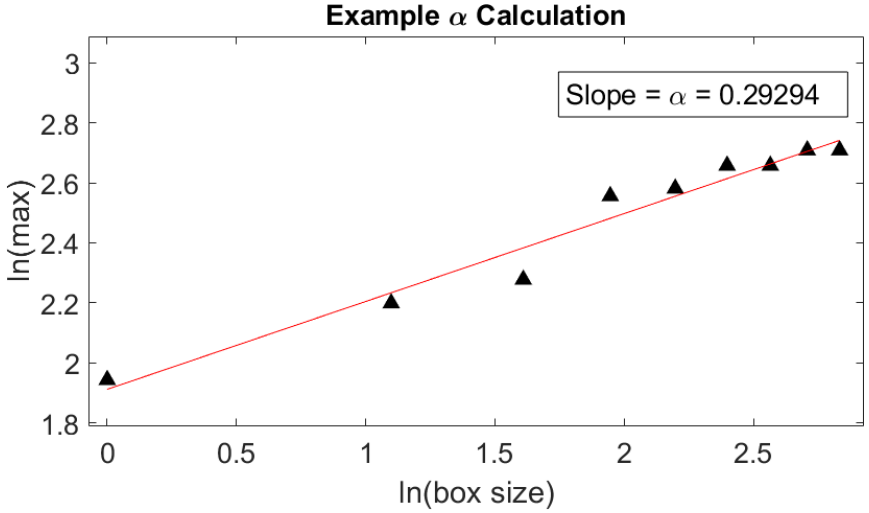

(b) Plot from which α is calculated.

Figure 3.3: Illustration of the calculation of the Hölder exponent for a particular pixel in a R_L map, using the *max* capacity.

10-15 μm without adaptive optics. This chapter will describe the analysis of *ex vivo* differences in fractal dimensions (through MFSs) associated with AD disease severity, AD versus age-related macular degeneration (AMD), and briefly AD versus other single diagnoses. Tests will then be performed to evaluate whether any differences are still within detection limits at resolutions that would be suited for live-eye imaging.

3.2 Methods

3.2.1 Main Test Groups

Several different test groups were considered for the MFA, with the aim of providing meaningful insights into differences in complexity and texture that could distinguish between deposits from two different groups. According to NIA-AA guidelines ([69]), the severity of AD pathology is determined from brain pathology based on Braak stage, neuritic plaques, and Thal phase. It has been previously shown that the number of presumed retinal amyloid-β deposits is significantly correlated to neuritic plaques, Thal phase, and overall score of severity, but not to Braak stage (related to tau protein) [54].

Three comparisons were performed in this study of retinal deposits: 1) those in anterior retinal layers associated with moderate severity of AD brain pathology versus those associated with high severity; 2) retinal deposits in anterior layers, assumed to be associated with AD with those in posterior layers, assumed to be associated with AMD and 3) anterior retinal amyloid deposits from those with AD compared to those with non-AD Neurodegenerative diseases (NDDs).

3.2.2 Numbers of Retinas and Retinal Deposits Imaged by Group

For the main group comparisons described below 12 retinas from 12 individuals with only AD (who may have also had CAA and/or CVD) were prepared. From these retinas, one subset of deposits in the anterior layers of the retina (59) was associated with intermediate severity of AD brain pathology and compared with the other subset of deposits in anterior retinal layers (297) which were associated with high severity of AD brain pathology. In the second study, the total number of anterior deposits (356, assumed to be AD associated) were compared to deposits in posterior layers (87, assumed to be AMD associated). In the third study, the total number of retinal deposits in anterior layers which were associated with AD brain pathology (356) were compared to anterior deposits (128) from five

retinas with brain pathology associated with non-AD-NDDs; from individuals without AD or CAA and each with one of amyotrophic lateral sclerosis (ALS), multiple system atrophy, frontotemporal lobular degeneration-TDP (FTLD-TDP), ALS associated with TDP, and FTLD-TDP type-C. See section 2.2.1 in chapter 2 for retinal dissection and staining protocols.

3.2.3 Statistical Analysis Comparing Groups

The average of polarization properties and properties of their multifractal spectra described below were calculated across deposits within the different groups described above. Calibrations that would optimize statistical significance of differences between MFSs of the different groups were explored by repeating the statistical tests for a series of varied settings in the MFS calculations, in each of these comparisons. All between group comparisons were performed using Kolmogorov-Smirnov (KS) tests and Wilcoxon tests.

3.2.4 Polarimetry of Retinal Deposits: Imaging Protocol

A Nikon Eclipse Ti-U inverted transmission microscope was equipped with a complete polarimeter (illustrated in figure 3.4) to perform the polarimetric measurements of each deposit and classify deposits as located in anterior or posterior layers. The polarization state generator (PSG) consists of a linear polarizer and a rotating quarter wave plate. The polarization state analyzer (PSA) is the same as the PSG with the components in reverse order. Calibration is needed prior to imaging. Illumination levels are set so that only a few pixels in the brightest image are saturated (so that all images will be fully described by the same set of levels). Objects (presumed to be deposits) that were too large to be captured in a single field at 40X were omitted from the analyses in this chapter. Rotating the PSG to four different angles generates four states that are far apart on the Poincaré sphere (a coordinate space in which all possible polarization states of light can be mapped [114]). For each of these angles, the PSA can be rotated to four different angles to analyze the signal that exits the sample (16 combinations). This leads to 16 images which are registered (using a customized version of a phase correlation method in the Fourier domain, prepared by Erik Mason [115]). The registered images are used to calculate the Mueller matrix associated with each pixel, by means of equation 1.3.

Recall that the polarization signals used in this chapter are described in chapter 1. Some polarization signal calculations can produce non-physical values. $R_L(x, y)$ can be infinite for a pixel if R_T is exactly 180 degrees. To avoid issues in the MFA in the uncommon event

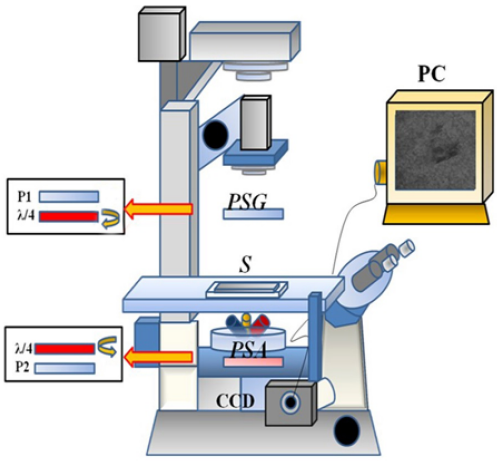

Figure 3.4: Diagram of polarimeter used in the measurement of the Mueller matrix. $PSG \rightarrow$ polarization state generator; $PSA \rightarrow$ polarization state analyzer; $P1$, $P2 \rightarrow$ stationary linear polarizers; $\lambda/4 \rightarrow$ rotating quarter wave plates; $S \rightarrow$ sample; $CCD \rightarrow$ charge coupled device; $PC \rightarrow$ monitor. Please note that $P1$ and $P2$ illustrated in this figure are unrelated to $p1$ and $p2$ which are used below to describe MFSs

that this happens, pixels with infinite values were set to 0, which would not have a major impact on the *max* capacity calculation. Though the case of infinite R_L was accounted for, there were cases with finite R_L greater than π which were not accounted for. The impact of this is discussed below. The polarimetry results and images used in this chapter were collected previously for another study, and now exists in a database shared by the group. Of the deposits that were imaged, some extended across multiple microscope fields. This chapter only included deposits that were fully enclosed within a single microscope field. Any deposits longer than ≈ 260 μm were excluded this study.

The mean polarization signals for deposits in each of the groups described in section 3.2.1 were calculated by applying masks which were based on the segmentation method created by Mason [115]. Some masks contained artifacts, likely due to dust in the imaging system. These small artifacts were removed[3].

Anterior deposits are characterized as those that begin in the anterior-most third of the retina, determined by features when visible and position of focus. Posterior deposits are those that form below the anterior layers.

3.2.5 Confocal Imaging Protocol

See section 2.2.2 in chapter 2 for the general description of sample preparation techniques. Confocal images of retinas from seven subjects with AD (six of which were included in the group of 12 on which polarimetric imaging was performed) were analyzed. For the textural analysis of multiple z-stacks of the same deposit, the rotatable scanning module within the LSM 700 was used to acquire z-stacks with six different orientations. These z-stacks were summed along the z-direction to create projections of the stacks into 2D images, for which the MFA results were compared.

3.2.6 Multifractal Analysis

The process described in section 3.1.2 is used to calculate the Hölder exponents for each pixel in each of the R_L maps (or in the projection of confocal z-stack, for example), with the exception of pixels close to boundaries. Pixels separated from any image boundary by less $\frac{Hvec_{max}}{2}$ are not included because calculation of α therein would require knowledge of pixels beyond the boundary of the image. Though it is a subtle step in the MFA, this

[3]This may have resulted in a few miscalculated masks, but only with small deposits that had low signal-to-noise ratios, which should be rare occurrences.

disregard for the pixels closest to the boundaries of the image can lead to some artificial points in the spectrum.

The sensitivity of the calculated MFS spectrum to changes in the Hölder exponent and Hausdorff dimension calculation parameters was tested. See figure 3.5 for instances in which the MFS is calculated under various settings for the region sizes used in calculating the Hölder exponents. Increasing $Hvec_{min}$ and decreasing $Hvec_{max}$ both led to broader MFSs, and loss of inflection between peaks in the spectra, which eventually leads to the erosion of the second peak altogether. For this reason, tests were performed to evaluate which values of $Hvec_{min}$ and $Hvec_{max}$ optimized the degree of differences between MFSs of several deposit groups (as detailed below).

After the Hölder exponent maps are prepared, the lower bound of the region size used in calculating F is needed. Recall that in equation 3.1 the upper limit of ball diameters is set to ∞, but such a condition is unreasonable for digital image analysis. Hence, a discrete set of values are considered for the ball diameters, S_{vec}. In FracLab the upper limit, $Svec_{max}$, is set as the smaller of 32 and $\frac{1}{4}$ of the smallest dimension in the image (rounded down). The images considered in this chapter are all larger than 128 x 128 so $Svec_{max}$ is set to 32. However, unlike the theoretical case, estimating the F of an image cannot involve balls of non-integer diameters, or diameters less than one. Instead, a minimum value $Svec_{min}$ for the calculation is set as a variable in FracLab, with 1 being the ultimate lower bound. $Svec$ is defined as the set of odd numbers between $Svec_{min}$ and $Svec_{max}$, inclusively (equation 3.5). Increasing $Svec_{min}$ generally flattens the background signal, and the resultant first peaks in the MFSs broaden. Similar to the tests performed by changing $Hvec$, other tests were performed by using different $Svec_{min}$ to determine if some differences in MFSs associated with deposits from compared groups were exacerbated in this way (see figure 3.6 for an example[4]).

Once the entire MFS has been calculated, the challenge is to extract meaning from the resultant spectrum. A series of metrics were considered that described the shapes of the MFSs, and provided insight into the complexity of the R_L maps (which are treated as images in this analysis).

$$Svec = Svec_{min} : 2 : Svec_{max} \tag{3.5}$$

These metrics are:

[4]The maps of F have been cropped to make the differences more visually obvious, and the range shown in the plot is abbreviated for a similar, yet separate, reason.

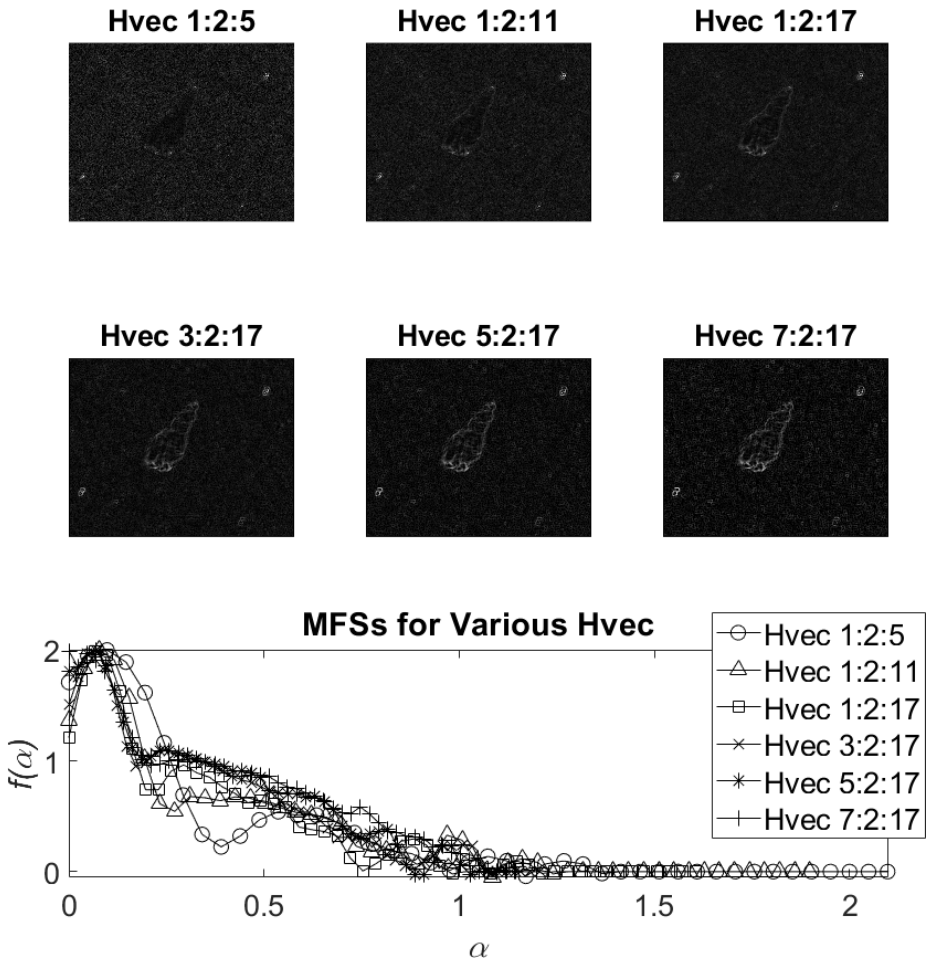

Figure 3.5: MFSs calculated for a particular deposit with six different sets of constraints on $Hvec$, with $Svec_{min}$ set to 1, and the *max* capacity. Similar variations of $Hvec$ were considered in some of the statistical group comparisons described below.

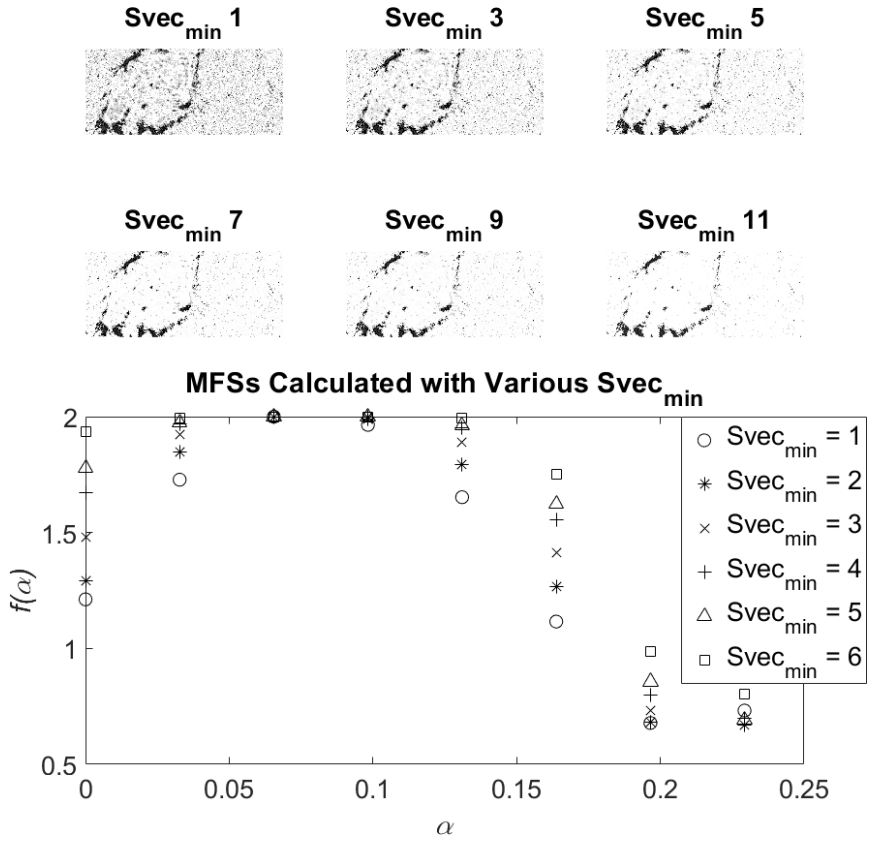

Figure 3.6: Maps of F, as in 3.2 based on different values for $Svec_{min}$, and corresponding MFSs, calculated with $Hvec$: 1:2:17 and the max capacity. Similar variations of $Svec_{min}$ were considered in some of the statistical group comparisons described below.

- $x1 \rightarrow$ the Hölder exponent associated with peak 1 (the most prominent peak of the spectrum)
- $w1 \rightarrow$ the full width at half max of peak 1
- $p1 \rightarrow$ the prominence of peak 1
- skewness[5] $\rightarrow$ measure of the extent to which the probability distribution of the spectrum is lopsided or skewed relative to a symmetric distribution, the 3rd moment of said distribution
- kurtosis[5] $\rightarrow$ measure of the tailedness of the probability distribution of the spectrum, the 4th moment of said distribution
- $MFE \rightarrow$ multifractal energy[6]; the trapezoidal integral of the MFS, a rough approximation of the area underneath the MFS.
- $MFR \rightarrow$ the difference between the greatest and lowest α bin values

Skewness and kurtosis are calculated based on a probability distribution based on frequencies of the F values in the MFS. In cases where there are at least two peaks in the spectrum, the following metrics are also considered:

- $x2 \rightarrow$ the Hölder exponent associated with peak 2 (the second most prominent peak of the spectrum)
- $w2 \rightarrow$ the full width at half max of peak 2
- $p2 \rightarrow$ the prominence of peak 2
- peak sep $\rightarrow$ the difference in the α of the peak 1 and peak 2
- peak ratio $\rightarrow$ the ratio $\frac{F(x1)}{F(x2)}$
- prom ratio $\rightarrow$ the ratio $\frac{p1}{p2}$
- width ratio $\rightarrow$ the ratio $\frac{w1}{w2}$

[5]These measurements are bias corrected, so that the systematic bias related to the number of points in the spectrum is irrelevant

[6]This measurement is not equivalent to the multifractal energy described by Xiong *et al* [116], but was inspired by their work.

The prominence and width of a peak can be understood graphically (see figure 3.7 for labelled MFSs before and after smoothing). The prominence is the minimum separation along the vertical axis that separates a peak from a neighbouring point of upward curvature. By default, the widths of the peaks are defined by Matlab [112] as the horizontal separation of two points that intercept a peak at a vertical distance below the summit of half the peak's prominence, equivalent to the "full width at half maximum". To mitigate spectral

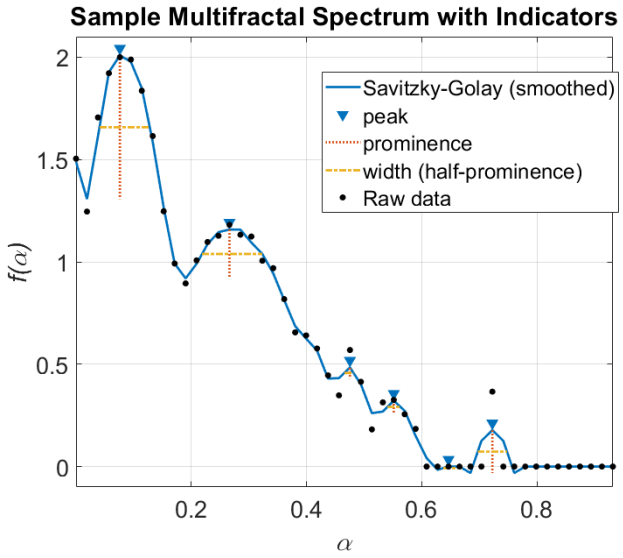

Figure 3.7: Sample MFS with labelled features.

noise and limit the influence of outliers on the peak detection, a smoothing algorithm (see figure 3.7) is applied. A Savitzky-Golay filter was used, which is a moving average filter. The extent of the filtering is evaluated for different points based on a linear least squares regression, without weights, and a polynomial fitting model (cubic in this case). The width values were stored as the number of bins of Hölder exponents spanned by the peak. Hence, since the Hölder exponent maps are binned into 50 levels, peak widths $w1$ and $w2$ are between (0,50]. The width ratio for any peak still holds the same scalar value it would have otherwise. It is also worth mentioning that there are many other manners in which the MFS could be compared, but only a subset were chosen as descriptors for this analysis.

For all MFA in this chapter (other than the depth-resolved MFA in section 3.2.8), only R_L signals were chosen because they were previously shown to provide the strongest contrast, meaning structural information about the deposits is well understood through R_L maps. The R_L maps were not segmented for the MFA calculations because the segmentation method used [115] might smooth the roughness of boundaries between deposits and

retinal surround. The mean polarization signals (associated with each of the metrics in table 1.1) are calculated across the deposits using the segmentation method by Mason [115] with the modifications described in section 3.2.4. Green contours overlaying polarization signal maps indicate the boundaries of the masks used in calculating the mean signals, which were purposefully set to overestimate the boundaries.

3.2.7 Testing Resilience against Transformations and Different Resolutions

Several aspects of MFA's resiliency to basic transformations were tested. These included comparisons of MFSs associated with: (1) digitally resampled R_L maps (to simulate lower magnifications which may be achievable in the live-eye device), (2) R_L maps calculated using images taken with various magnifications (to directly identify differences between MFS associated with various objectives and to complement the digital method), (3) z-stacks imaged with different resolutions and resampled, and (4) z-stacks of a single deposit with different orientations (in the *en face* plane). Both (3) and (4) are addressed in appendix A.

In the Matlab script used for the multifractal calculation, `imresize` was applied to each R_L map (taken with a 40X objective) twice. Using the *nearest* approach, the R_L maps were first shrunk by some factor, reducing the number of pixels and also the size of the image. Then the images are enlarged by the reciprocal of said factor, using "nearest-neighbour interpolation". The purpose of the enlarging that follows the initial loss of information is to ensure that all image dimensions remain approximately unchanged. This is critical because changes in the number of pixels would significantly impact the calculations of both α and F. This process of shrinking and enlarging the R_L maps was repeated for scaling factors between 10-90%, with an additional test at 1% (equivalent to 100x0.16 μm = 16 μm resolution).

Images taken with different objective magnifications: 4X, 10X, 20X, and 40X, were also compared. R_L maps of the 4X, 10X, and 20X objectives were enlarged and then cropped so that the fields covered nearly the same regions as the 40X R_L map. Thus, the effects of a change in optical resolution will be assessed, independent of other factors such as pixel resolution. After resizing, the approximate center of the deposit was labelled manually using a graphical data-point selection in Matlab [112]. The offset between the coordinates of the selected location and the true center were used to translate the R_L map. Afterwards, each of the maps taken at an objective O were cropped to regions of the same

extent, specified by equation 3.6:

$$x^O_{crop} = x^O \left\lfloor \frac{1}{2}(1 \pm \frac{M^O}{40}) \right\rfloor \tag{3.6}$$

where x^O_{crop} is the width of the R_L map generated based on images taken with O after cropping, x^O is the width before cropping, M^O is the magnification of objective O, and $\lfloor V \rfloor$ for some arbitrary value V is the floor of V (i.e. rounded down to the nearest integer). The equivalent expression holds for the bounds on the height of the cropped image. See section A.7 in appendix A for the derivation of equation 3.6.

3.2.8 Depth-Resolved Multifractal Analysis

Studying the slices of a z-stack was used as a means for assessing depth-dependence of deposit texture for the purpose of determining whether there might be a range of depth within deposits that produces similar MFSs. Depth-resolved fluorescence images of anterior retinal amyloid deposits were acquired using CSLM. Observations of various depth-resolved MFSs in association with corresponding z-stacks were used to give insight into the depth variation of features of the MFSs. Two z-stacks of the same deposit were taken with different voxel dimensions (0.44 μm and 1 μm, respectively) and the corresponding depth-resolved MFSs were compared as an additional test of the robustness of MFA to changes in lateral and depth resolution. The latter of these was resized (using the `imresize3` function in Matlab [112]) along all three dimensions by a factor of 1/0.44 (i.e. the ratio of the voxel sizes), using the nearest neighbour method of interpolation.

3.3 Results

3.3.1 Group Comparisons

As described in the Methods, MFA was applied to the groups described in section 3.2.1 to determine whether MFA would reveal textural differences between the respective R_L maps. Mean deposit values for each of the polarization signals listed in table 1.1 were also used to differentiate groups.

Comparison of High and Intermediate Severity of AD Brain Pathology

The anterior deposits assumed to be associated with AD, were further categorized by their associated severity of AD brain pathology (based on NIA-AA guidelines) to determine whether MFA could be used to distinguish between these groups. A preliminary test was performed for the different AD severities (figures 3.8 and 3.9). From early analysis, the metrics most likely to separate the two groups were those related to spectrum width. Deposits that exemplify these differences in their MFSs were chosen for figures 3.8 (intermediate severity of AD pathology) and 3.9 (high severity of AD pathology). Deposits with intermediate severity of AD pathology had MFSs with much broader width. The MFSs shown were calculated with $Svec_{min}$ at 1 and $Hvec = 1, 3$, meaning only two very small region sizes were used to do the Hölder exponent calculations. Though the separation is still strong for larger $Hvec_{max}$ values, low $Hvec_{max}$ gives the most significant p-values, indicating that considering highly local texture improves results.

The tables of results below are presented with insignificant p-values replaced by dashes. In total, 14 MFS-related metrics were considered for the comparison of deposits associated with AD versus presumably AMD, and for each metric tested, 17 different sets of MFA parameters were used in producing the associated MFSs. The Bonferroni corrected significance threshold was thus $\frac{0.05}{14*17} \approx 0.0002$.

Statistical Results

The deposits associated with different severities of AD brain pathology were most significantly separated for low $Hvec_{max}$. This implies that the textural features presenting differences (at least as measured by MFE and MFR) are on smaller scales than the textural features that distinguish AD from AMD deposits. It is $x1$ (which represents the position of the most prominent peak in the MFS) that seems to be the metric most robust to changes in parameters in this comparison, being highly significant for all tested values in $Hvec_{max}$ when $Hvec_{min} = 1$. Results for MFE, MFR, and $x1$ all appear to be highly significant for all tested values of $Svec_{min}$ when $Hvec = 1 : 2 : 17$.

Polarimetry Results

The results of the statistical tests which compared the averages and cumulative distributions of polarimetry-based metrics for the anterior deposits associated with high and intermediate severities of AD are shown in table 3.3. All metrics with differences in at least one of the statistical tests that were significant below the Bonferroni corrected threshold of $0.05/24 \approx 0.0021$ are presented. D_T, diattenuation, is the polarization metric associated with the greatest separation between deposits from subjects with intermediate and high severities of AD. Deposits associated with high severity of AD pathology had greater D_T.

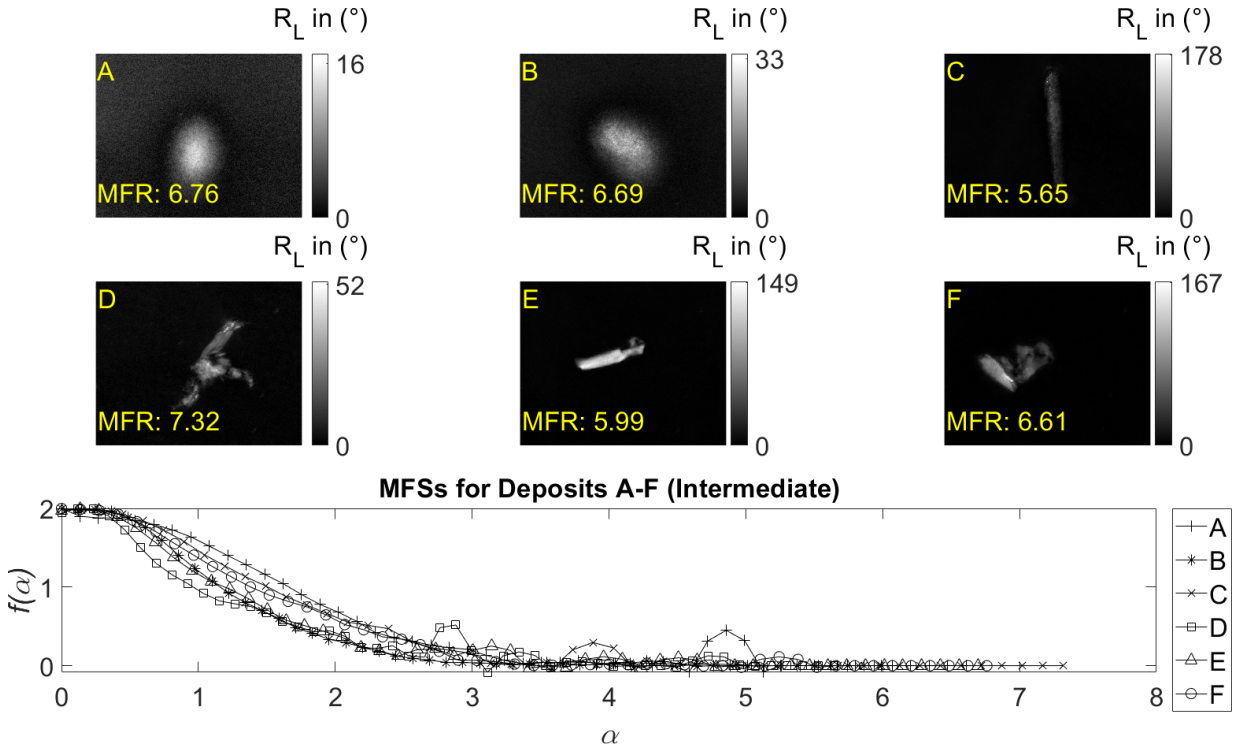

Figure 3.8: R_L maps for six deposits in retinal tissue samples from subjects with intermediate severity of AD pathology. A-C are from a single retina and D-F are from another.

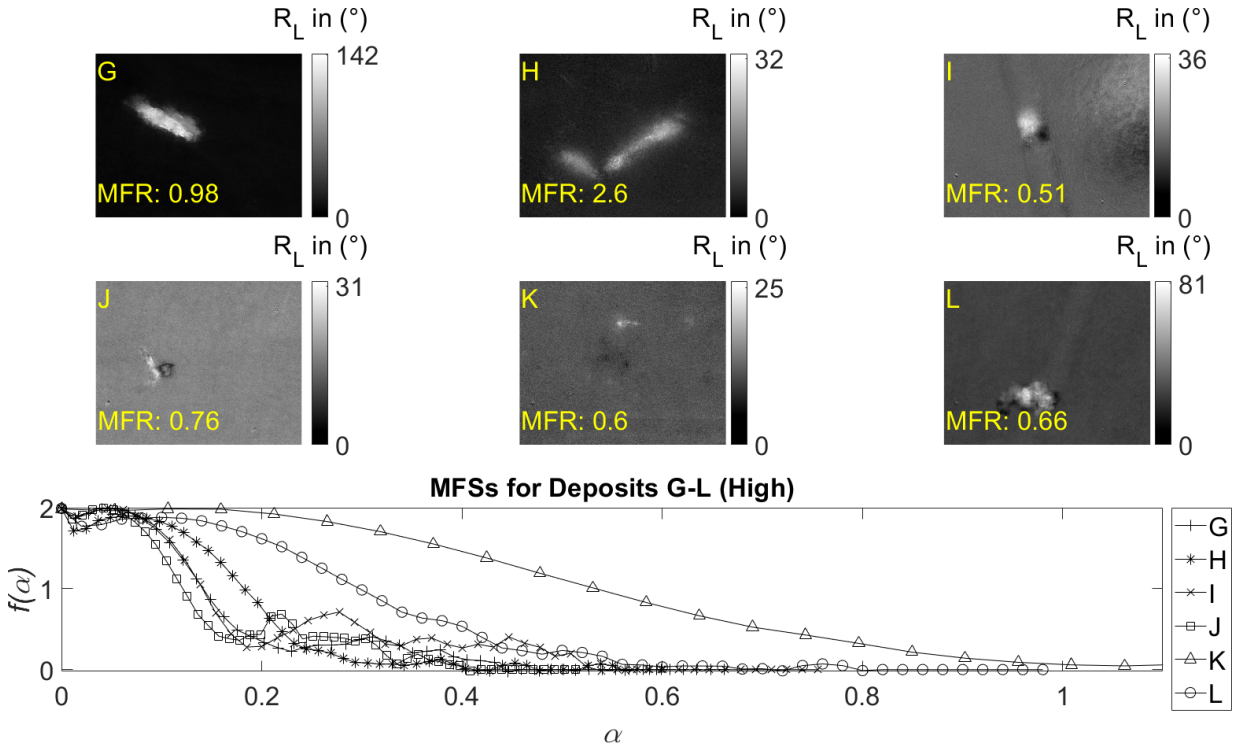

Figure 3.9: R_L maps for six deposits in retinal tissue samples from subjects with high severity of AD pathology, each from a different retina.

$Hvec_{min}, Hvec_{max}, Svec_{min}$	$Kurtosis$	$Skewness$	$PeakRatio$	$PeakSep$	$PromRatio$	$WidthRatio$	$x1$	$x2$	$w1$	$w2$	$p1$	$p2$	MFE	MFR
1,11,1	6.E-07	4.E-05	-	6.E-06	-	-	2.E-10	2.E-06	-	-	1.E-05	-	1.E-12	3.E-11
1,17,1	5.E-08	-	-	3.E-07	-	2.E-05	5.E-10	6.E-08	3.E-07	-	1.E-05	-	7.E-10	5.E-09
1,23,1	9.E-09	-	8.E-05	6.E-07	-	3.E-05	3.E-11	7.E-08	5.E-08	-	-	-	8.E-07	4.E-06
3,11,1	3.E-09	1.E-07	-	-	-	-	-	-	-	-	-	-	9.E-05	-
3,17,1	2.E-08	-	-	-	-	-	6.E-11	-	5.E-05	-	-	-	-	-
3,23,1	2.E-06	-	-	-	-	1.E-05	2.E-11	-	3.E-08	-	-	-	-	-
1,5,1	4.E-06	8.E-06	-	-	-	-	2.E-07	-	-	-	-	-	3.E-13	6.E-12
5,11,1	2.E-08	3.E-07	-	-	-	-	-	-	-	-	-	-	-	-
5,17,1	2.E-08	-	-	-	-	-	-	-	-	-	-	-	-	-
5,23,1	4.E-06	-	-	-	-	-	4.E-09	-	5.E-05	-	-	-	-	-
1,11,3	3.E-06	-	2.E-04	8.E-12	-	-	7.E-09	3.E-12	2.E-05	-	-	-	7.E-12	3.E-11
1,17,3	4.E-07	-	6.E-05	1.E-09	-	4.E-05	2.E-11	2.E-10	3.E-07	-	-	-	3.E-09	5.E-09
1,23,3	5.E-08	-	5.E-05	2.E-06	-	8.E-06	7.E-12	2.E-07	1.E-08	-	-	-	5.E-06	4.E-06
1,17,5	3.E-07	-	2.E-05	2.E-11	-	1.E-04	5.E-10	4.E-12	2.E-07	-	-	-	2.E-09	5.E-09
1,17,7	2.E-07	-	8.E-06	4.E-11	-	-	3.E-08	4.E-12	1.E-06	-	-	-	2.E-09	5.E-09
5,35,1	-	-	-	-	-	4.E-05	4.E-09	-	1.E-07	-	-	-	-	-
1,3,1	8.E-06	8.E-06	-	-	-	-	3.E-12	1.E-07	-	-	-	-	2.E-13	4.E-12

Table 3.1: Wilcoxon 2-sided p-values associated with multifractal peak-related metrics for the comparison of deposits associated with different severities of AD; dashes are shown in place of p-values that were not significant below the Bonferroni corrected threshold of $\approx 2 * 10^{-04}$.

$Hvec_{min}, Hvec_{max}, Svec_{min}$	$Kurtosis$	$Skewness$	$PeakRatio$	$PeakSep$	$PromRatio$	$WidthRatio$	$x1$	$x2$	$w1$	$w2$	$p1$	$p2$	MFE	MFR
1,11,1	1.E-07	-	-	1.E-07	-	2.E-04	1.E-09	1.E-08	2.E-04	-	6.E-06	-	0.E+00	2.E-09
1,17,1	2.E-08	-	-	3.E-08	-	7.E-06	3.E-08	3.E-08	3.E-07	-	2.E-07	-	4.E-10	4.E-07
1,23,1	5.E-08	-	6.E-06	4.E-09	-	1.E-06	3.E-09	1.E-09	1.E-08	-	-	-	6.E-08	2.E-05
3,11,1	6.E-10	2.E-08	-	-	-	-	-	9.E-05	-	-	-	-	8.E-07	-
3,17,1	4.E-10	-	-	-	-	-	9.E-09	-	9.E-06	-	3.E-05	-	-	-
3,23,1	6.E-08	-	-	-	-	8.E-05	2.E-09	-	1.E-10	-	3.E-05	-	-	-
1,5,1	3.E-07	5.E-08	-	-	-	-	6.E-08	2.E-05	-	-	5.E-05	-	0.E+00	7.E-10
5,11,1	9.E-09	4.E-08	-	-	-	-	-	-	-	-	-	-	-	-
5,17,1	3.E-10	-	-	-	-	-	-	-	1.E-04	-	-	-	-	-
5,23,1	1.E-07	-	-	-	-	-	1.E-09	-	2.E-05	-	-	-	-	-
1,11,3	9.E-08	-	2.E-04	1.E-10	-	8.E-05	6.E-09	4.E-10	1.E-04	-	-	-	2.E-10	2.E-09
1,17,3	2.E-07	-	2.E-05	1.E-09	-	6.E-06	7.E-10	1.E-09	3.E-07	-	-	-	1.E-09	4.E-07
1,23,3	2.E-06	-	5.E-06	1.E-08	-	3.E-07	0.E+00	2.E-08	7.E-09	-	-	-	1.E-06	2.E-05
1,17,5	1.E-07	-	3.E-05	9.E-10	-	7.E-06	5.E-09	6.E-10	9.E-07	-	-	-	2.E-09	4.E-07
1,17,7	4.E-08	-	7.E-06	3.E-09	-	1.E-04	1.E-08	2.E-09	1.E-05	-	-	-	2.E-08	4.E-07
5,35,1	-	-	-	-	-	-	6.E-09	-	3.E-07	-	-	-	-	-
1,3,1	7.E-07	2.E-07	-	-	-	-	0.E+00	2.E-08	-	-	-	-	0.E+00	2.E-10

Table 3.2: KS asymptotic p-values associated with multifractal peak-related metrics for the comparison of deposits associated with different severities of AD brain pathology; dashes are shown in place of p-values that were not significant below the Bonferroni corrected threshold of $\approx 2 * 10^{-04}$.

Metric	p_{2WIL}	p_{KSA}
x	-	4.24E-05
R_T	4.36E-04	1.96E-04
R_C	-	3.46E-05
P_T	7.78E-09	5.60E-07
P_L	3.60E-08	7.29E-07
P_C	8.42E-08	3.72E-08
D_T	2.68E-13	0
D_L	7.34E-07	9.15E-08
D_C	9.43E-06	4.84E-09
A_T	2.51E-06	5.50E-06
A_θ	7.32E-05	4.41E-04
A_C	7.08E-07	3.43E-07

Table 3.3: P-values associated with polarization signals for separating deposits from subjects with intermediate and high severity of AD pathology. p_{2WIL} corresponds to a 2-sided Wilcoxon p-value, and p_{KSA} corresponds to an asymptotic Kolmogorov-Smirnov p-value. Values that were not significant below the Bonferroni corrected threshold of 0.0021 are replaced with dashes.

Deposits in more advanced stages of the disease might have a greater tendency to attenuate polarized light with some preferential axis, which could indicate those deposits are more packed, ordered, and/or thicker than those in moderate severities. However, as previously found by our group for retinal amyloid deposits, average diattenuation in both groups is small. In the D_T maps (figures 3.10 and 3.11), background signals around deposits associated with intermediate severity of AD pathology are lower than in the high severity deposit maps. For each of the properties whose means and KS distributions are different with disease severity, the distributions of the means across deposits overlap.

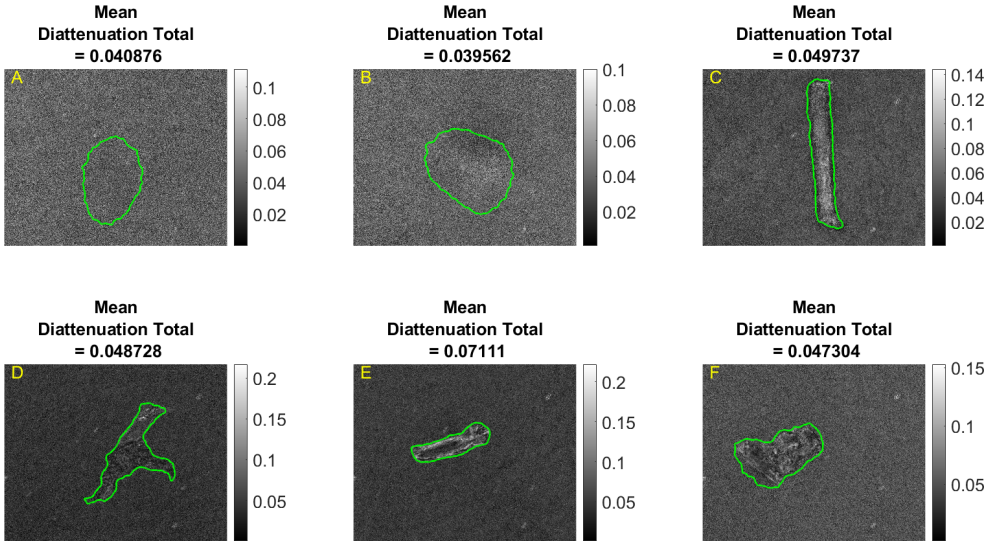

Figure 3.10: D_T maps for six deposits in anterior layers of retinal tissue samples from subjects with intermediate severity of AD brain pathology. Green contours represent the boundaries of the masks used in calculating the mean polarization signals, and were based on the Euclidean distance image method by Mason [115]. Note that although the mean values differ significantly, between groups, the individual values overlap.

Anterior and Posterior Deposits

For the application of distinguishing between deposits that formed in the anterior layers, presumed to be associated with AD, and posterior layers of retinas, presumed to be associated with AMD in *ex vivo* AD human tissue, tests were performed to determine which metrics best separated the groups, and under which MFA parameters the separation was optimized, based on Wilcoxon and KS tests.

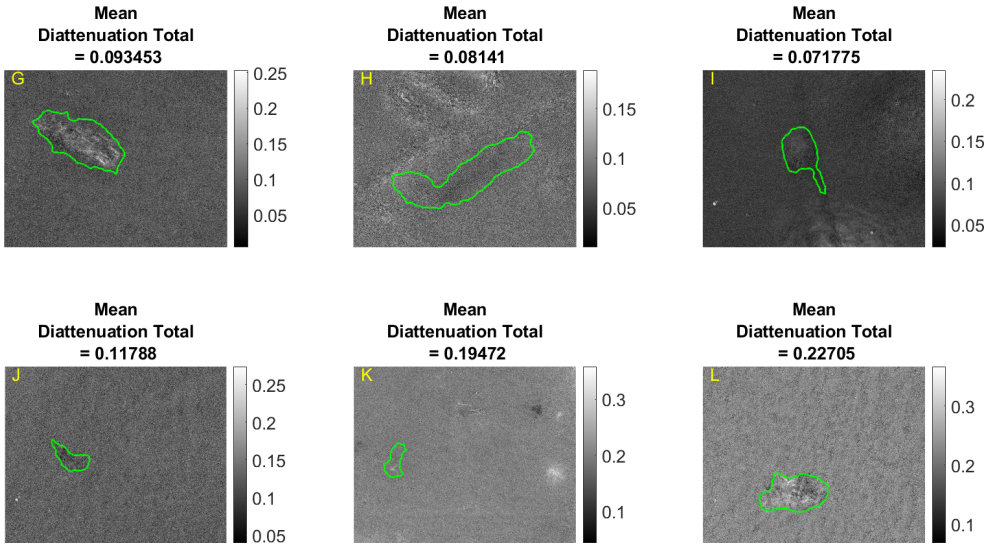

Figure 3.11: D_T maps for six deposits in anterior layers of retinal tissue samples from subjects with high severity of AD brain pathology. Green contours represent the boundaries of the masks used in calculating the mean polarization signals, and were based on the Euclidean distance image method by Mason [115].

Before proceeding with the statistical analysis, some qualitative comparisons were performed to acquire a sense of which of the multifractal metrics would most aptly characterize differences between deposits that form in the anterior and posterior retina (see figures 3.12, 3.14, and 3.13). The properties of all of the anterior deposits were compared to all of the posterior deposits. The tables of results below are presented with insignificant p-values replaced by dashes, based on comparisons of 14 MFS-related metrics and entropy E, through 17 different sets of MFA parameters, of deposits presumably associated with AD versus those presumably associated with AMD. The Bonferroni corrected statistical significance threshold was nearly the same as in the comparison of deposits associated with different severities of AD brain pathology, $0.05/(15 * 17) \approx 0.0002$.

Statistical Results

The statistical differences between the deposits associated with AD and those presumably associated with AMD were significant for a range of calibrations (in the MFS parameters) for several metrics. From the Wilcoxon tests, several metrics, including the peak-width related metrics, were highly significant ($p < 0.00001$) with $Hvec_{max} = 17$ and higher. This was also true for low values of $Hvec_{min}$ and $Svec_{min}$. In the results of the Kolmogorov-Smirnov tests, highly significant p-values were again found for high values of $Hvec_{max}$

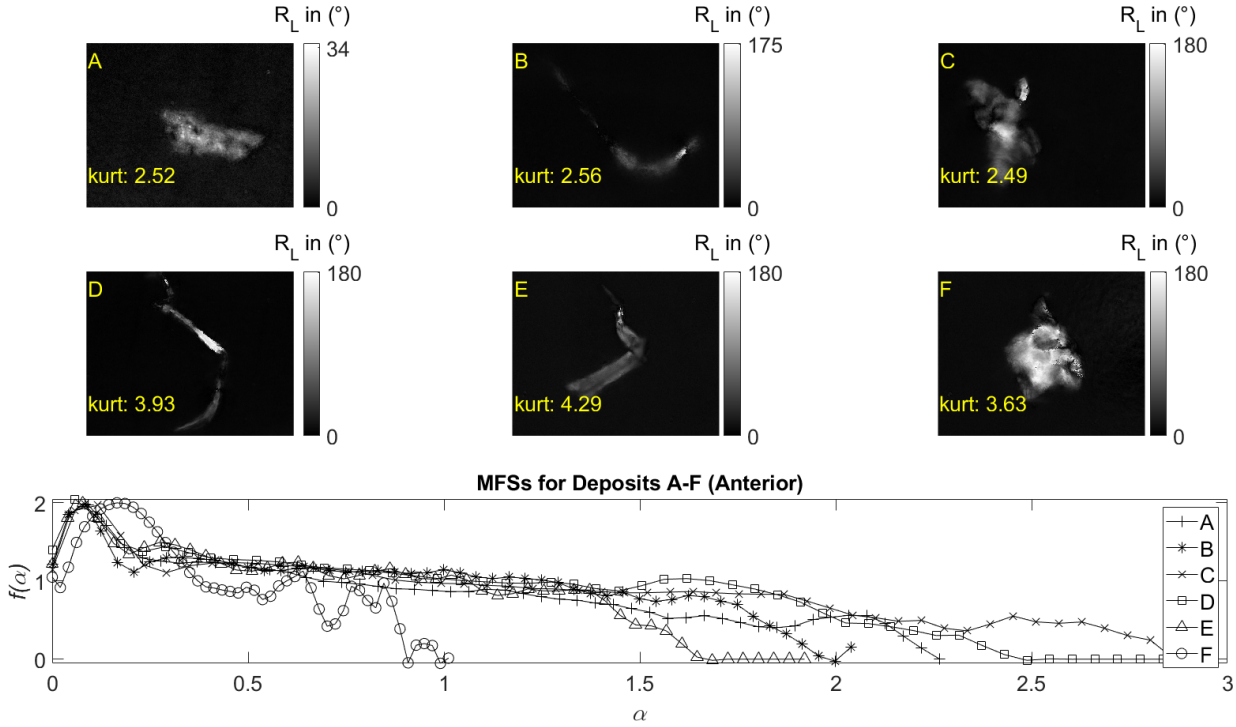

Figure 3.12: R_L maps for six deposits with well-defined boundaries, located in the anterior layers of various retinal tissue samples. The settings used for this figure's MFSs as well as those in 3.13 and 3.14 were $Hvec_{min} = 3$, $Hvec_{max} = 29$, $Svec_{min} = 3$, capacity: *max*; *kurt* denotes the kurtosis as defined earlier in this chapter. Although the means of kurtosis for the anterior deposits are significantly different from those for posterior deposits, their values overlap.

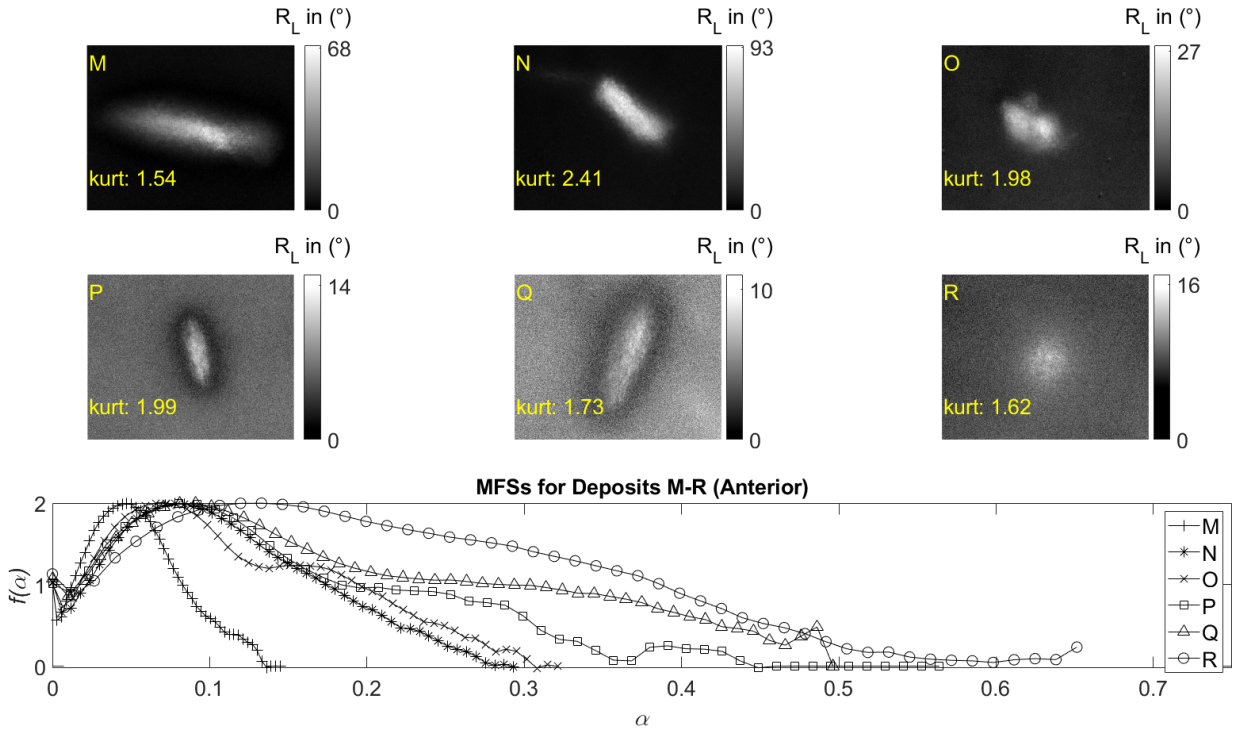

Figure 3.13: R_L maps for six deposits with poorly-defined boundaries, located in the anterior layers of various retinal tissue samples, *kurt* denotes the kurtosis as defined earlier in this chapter. Although the means of kurtosis for the anterior deposits are significantly different from those for posterior deposits, their values overlap.

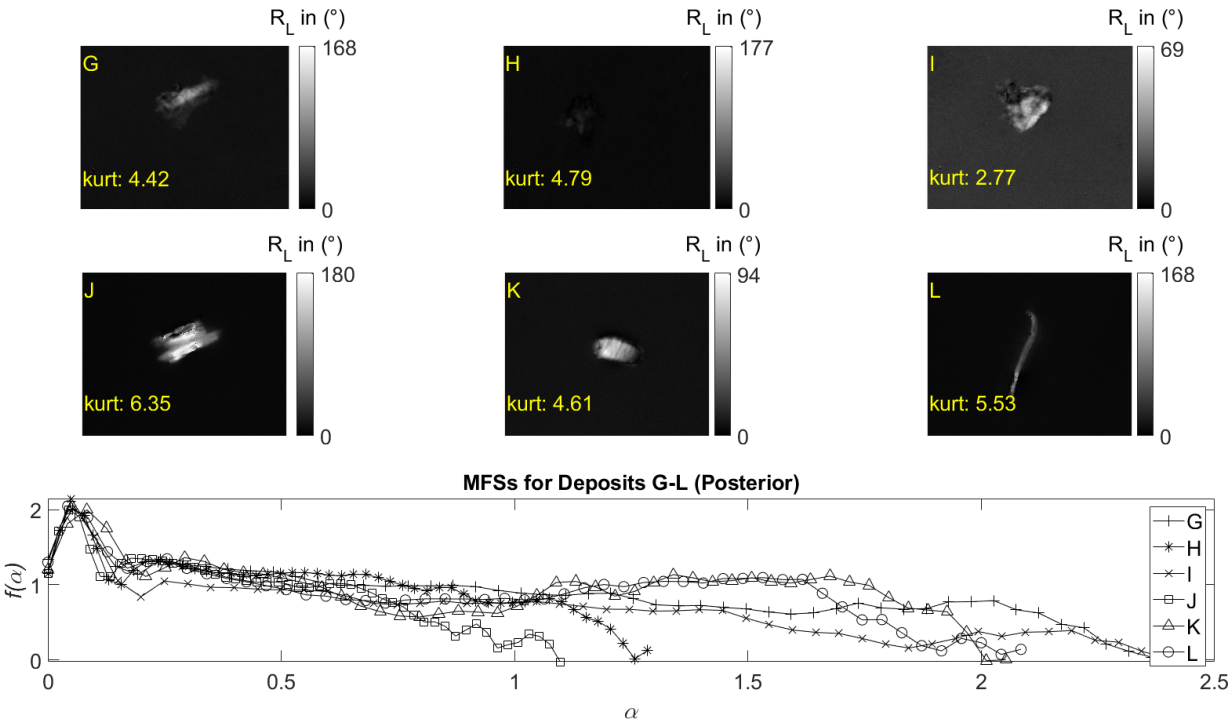

Figure 3.14: R_L maps for six deposits with well-defined boundaries, located in the posterior layers of various retinal tissue samples; *kurt* denotes the kurtosis as defined earlier in this chapter. Although the means of kurtosis for the anterior deposits are significantly different from those for posterior deposits, their values overlap.

$Hvec_{min}, Hvec_{max}, Svec_{min}$	$Kurtosis$	$Skewness$	$PeakRatio$	$PeakSep$	$PromRatio$	$WidthRatio$	$x1$	$x2$	$w1$	$w2$	$p1$	$p2$	MFE	MFR
1,5,1	1.E-06	1.E-06	-	-	-	-	-	3.E-05	-	-	-	8.E-05	3.E-07	2.E-05
1,11, 1	3.E-06	-	1.E-06	6.E-05	9.E-06	3.E-07	7.E-08	2.E-05	2.E-05	1.E-04	-	4.E-06	1.E-04	-
1,17,1	8.E-05	-	2.E-07	4.E-05	4.E-08	5.E-11	2.E-08	1.E-05	3.E-07	4.E-07	-	3.E-08	-	-
1,23,1	-	-	9.E-07	-	4.E-08	2.E-10	2.E-08	1.E-04	3.E-08	2.E-06	-	2.E-08	-	-
3,11,1	4.E-10	3.E-06	6.E-05	-	-	-	-	-	-	-	-	2.E-04	-	-
3,17,1	1.E-09	-	2.E-04	-	1.E-04	1.E-05	2.E-05	-	8.E-08	-	-	-	-	-
3,23,1	4.E-06	-	-	-	-	4.E-10	3.E-08	-	2.E-10	-	-	-	-	-
3,29,1	1.E-04	-	-	-	-	5.E-08	3.E-08	-	2.E-11	-	-	-	-	-
3,35,1	-	-	-	-	-	1.E-07	1.E-08	-	1.E-11	-	1.E-04	-	-	-
5,11,1	9.E-09	-	-	-	-	-	-	-	-	-	-	-	-	-
5,17,1	3.E-09	-	-	-	-	-	-	-	-	-	-	-	-	-
5,23,1	1.E-06	-	-	-	-	-	-	-	1.E-05	-	-	-	-	-
1,11,3	9.E-07	-	8.E-05	3.E-05	2.E-06	1.E-07	1.E-05	2.E-05	7.E-06	3.E-05	-	5.E-06	6.E-05	-
1,17,3	2.E-05	-	3.E-07	1.E-05	2.E-09	1.E-10	1.E-08	5.E-06	2.E-07	2.E-07	-	2.E-08	-	-
1,23,3	2.E-04	-	4.E-08	1.E-05	2.E-09	3.E-11	2.E-08	2.E-06	1.E-08	2.E-07	-	1.E-08	-	-
1,17,5	2.E-06	-	3.E-06	6.E-06	2.E-08	6.E-10	2.E-06	2.E-06	1.E-06	2.E-07	4.E-05	4.E-07	-	-
1,17,7	3.E-07	-	5.E-07	6.E-07	1.E-07	4.E-05	-	9.E-08	-	-	2.E-04	2.E-06	-	-

Table 3.4: Wilcoxon 2-sided p-values associated with multifractal peak-related metrics for the comparison of deposits in the anterior and posterior layers of the retina; dashes are shown in place of p-values that were not significant below the Bonferroni corrected threshold.

$Hvec_{min}, Hvec_{max}, Svec_{min}$	$Kurtosis$	$Skewness$	$PeakRatio$	$PeakSep$	$PromRatio$	$WidthRatio$	$x1$	$x2$	$w1$	$w2$	$p1$	$p2$	MFE	MFR
1,5,1	5.E-07	2.E-06	5.E-05	5.E-05	-	-	2.E-04	6.E-06	-	-	-	-	2.E-06	2.E-05
1,11,1	3.E-06	1.E-04	3.E-08	4.E-05	1.E-05	2.E-06	5.E-07	2.E-05	7.E-06	6.E-05	-	2.E-06	1.E-05	-
1,17,1	-	-	3.E-07	5.E-06	1.E-08	2.E-09	7.E-08	3.E-06	8.E-07	4.E-07	-	6.E-09	-	-
1,23,1	-	-	1.E-06	1.E-04	6.E-09	9.E-08	2.E-08	7.E-05	9.E-07	1.E-05	-	4.E-09	-	-
3,11,1	2.E-09	-	4.E-05	-	-	-	-	6.E-05	-	-	-	-	-	-
3,17,1	1.E-09	-	-	2.E-04	-	-	4.E-06	1.E-05	4.E-07	-	-	-	-	-
3,23,1	6.E-05	-	-	-	-	-	3.E-08	9.E-09	-	1.E-09	-	-	-	-
3,29,1	-	-	-	-	-	-	5.E-06	9.E-08	-	4.E-09	-	2.E-05	-	-
3,35,1	-	-	-	-	-	-	2.E-05	3.E-08	-	9.E-10	-	7.E-05	-	-
5,11,1	9.E-08	-	-	-	-	-	-	-	-	-	-	-	-	-
5,17,1	2.E-08	-	-	-	-	-	-	-	-	-	-	-	-	-
5,23,1	5.E-06	-	-	-	-	-	1.E-04	6.E-06	-	-	-	-	-	-
1,11,3	9.E-08	3.E-05	8.E-05	2.E-05	4.E-05	6.E-07	2.E-05	2.E-05	2.E-06	2.E-05	5.E-05	2.E-05	1.E-05	-
1,17,3	1.E-04	-	2.E-07	3.E-06	1.E-07	3.E-09	6.E-08	2.E-06	2.E-06	2.E-07	2.E-05	8.E-08	-	-
1,23,3	-	-	7.E-08	5.E-06	5.E-08	8.E-08	7.E-09	2.E-06	8.E-07	8.E-07	2.E-04	3.E-08	-	-
1,17,5	2.E-06	-	3.E-07	6.E-07	3.E-09	3.E-09	4.E-06	5.E-07	2.E-06	2.E-06	6.E-06	8.E-09	-	-
1,17,7	5.E-08	-	1.E-06	7.E-08	5.E-08	1.E-04	-	2.E-08	-	-	5.E-05	8.E-07	-	-

Table 3.5: KS asymptotic p-values associated with multifractal peak-related metrics for the comparison of deposits in the anterior and posterior layers of the retina; dashes are shown in place of p-values that were not significant below the Bonferroni corrected threshold.

Metric	p_{2WIL}	p_{KSA}
x	5.67E-06	2.90E-06
t	-	3.67E-04
b	8.40E-07	1.21E-05
T	1.23E-12	5.53E-11
R_T	3.01E-05	3.19E-04
R_C	6.13E-07	2.56E-06
P_T	4.43E-06	1.07E-08
P_L	8.20E-06	1.37E-08
P_C	6.44E-07	2.54E-06
D_T	1.45E-05	8.58E-04
D_θ	1.27E-05	2.51E-05
D_C	3.78E-07	1.16E-06
A_T	1.13E-04	2.16E-04
A_C	1.30E-03	6.61E-05
$A*$	-	4.98E-05

Table 3.6: P-values associated with polarization signals for separating anterior and posterior deposits. p_{2WIL} corresponds to a 2-sided Wilcoxon p-value, and p_{KSA} corresponds to an asymptotic Kolmogorov-Smirnov p-value. Values that were not significant below the Bonferroni corrected threshold of 0.0021 are replaced with dashes.

and low values of $Hvec_{min}$. These tests had less sensitivity to changes in $Svec_{min}$ than the Wilcoxon tests, remaining highly significant in multiple metrics for $Svec_{min} = [1, 7]$. Note that E was also measured for each of these deposits but means for these two groups were not significantly different on average for these two groups, with p_{2WIL} and p_{KSA} both > 0.001 which is greater than the Bonferroni corrected significance threshold of ≈ 0.0002.

Polarimetry Results

Several polarization signals were able to separate in the KS statistics, however fewer were able to separate in both statistical tests. The metrics associated with the most significant separations (with p-values less than 10^{-5}) are listed in table 3.6 below, as are the associated p-values (reported by SAS [117, 118]). The p-values (table 3.6) for mean T are the most significant, with $p_{2WIL} < 10^{-12}$ and $p_{KSA} = 0$. This difference is not apparent from the T maps shown for anterior and posterior deposits in figures 3.15 and 3.16. The mean transmission values for the deposits in the different groups overlapped. Posterior deposits

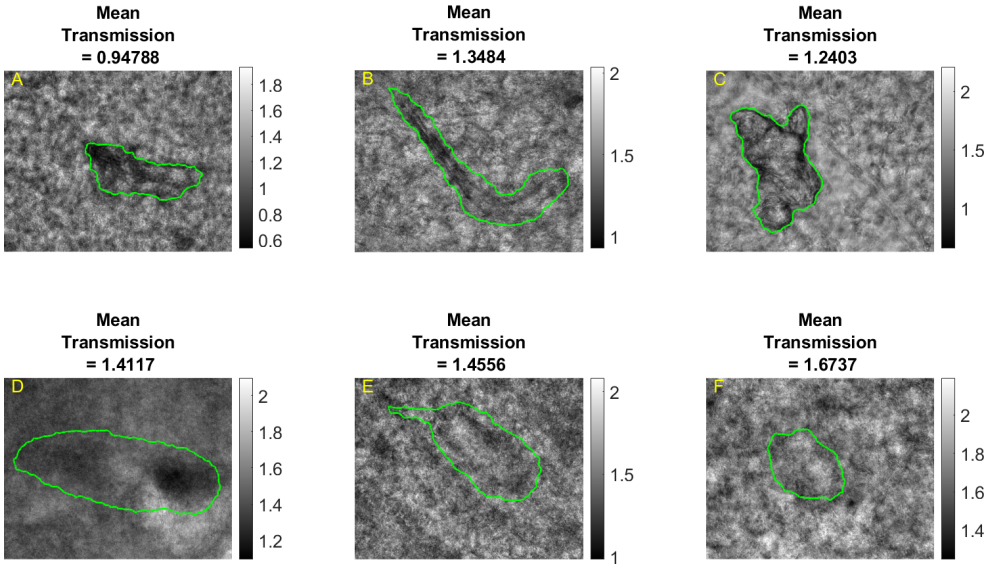

Figure 3.15: Transmission maps for six deposits in anterior layers of retinal tissue samples from subjects with AD. Green contours represent the boundaries of the masks used in calculating the mean polarization signals, and were based on the Euclidean distance image segmentation method by Mason [115].

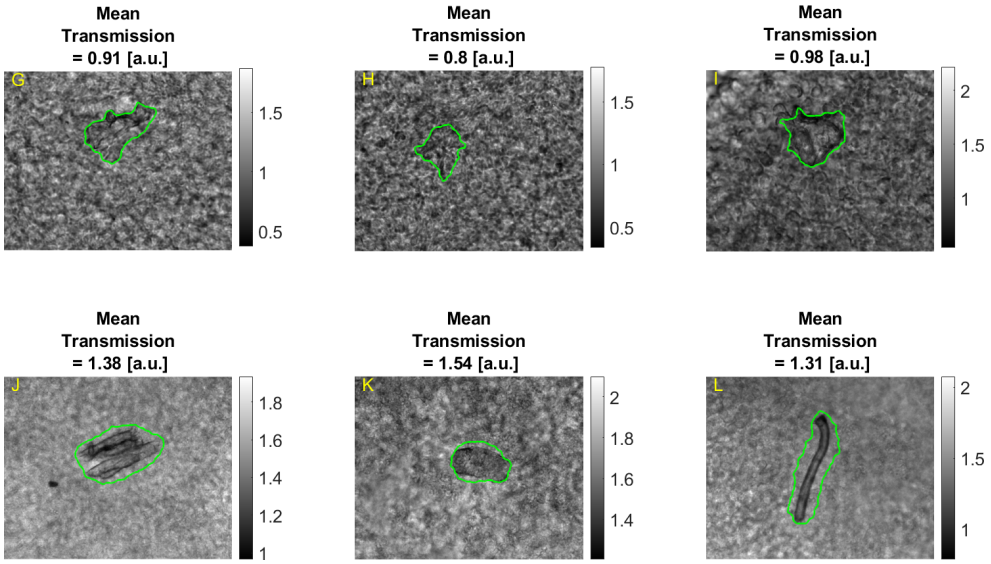

Figure 3.16: Transmission maps for six deposits in posterior layers of retinal tissue samples from subjects with AD, presumably associated with AMD. Green contours represent the boundaries of the masks used in calculating the mean polarization signals, and were based on the Euclidean distance image segmentation method by Mason [115].

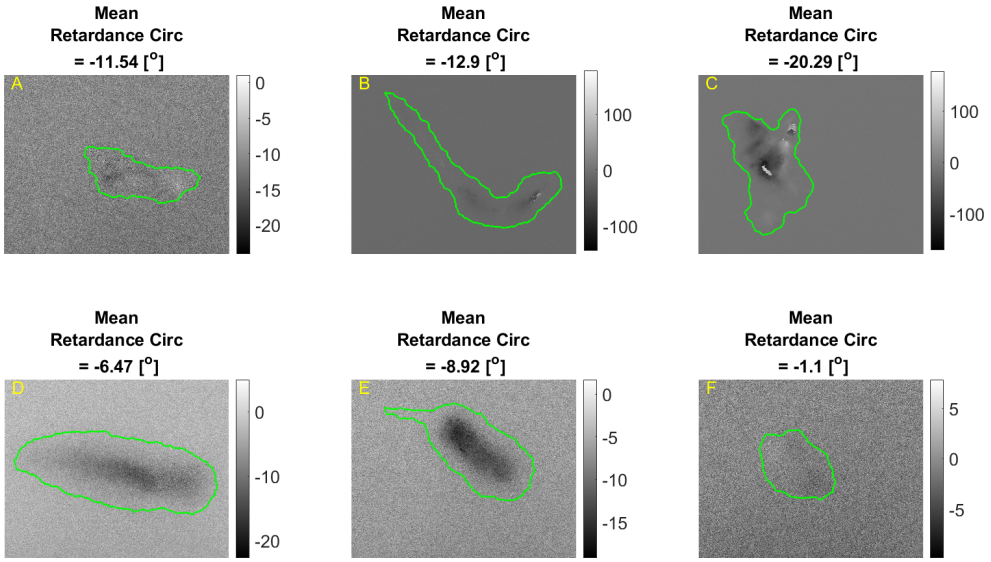

Figure 3.17: R_C maps for six deposits in anterior layers of retinal tissue samples from subjects with AD. Green contours represent the boundaries of the masks used in calculating the mean polarization signals, and were based on the Euclidean distance image method by Mason [115].

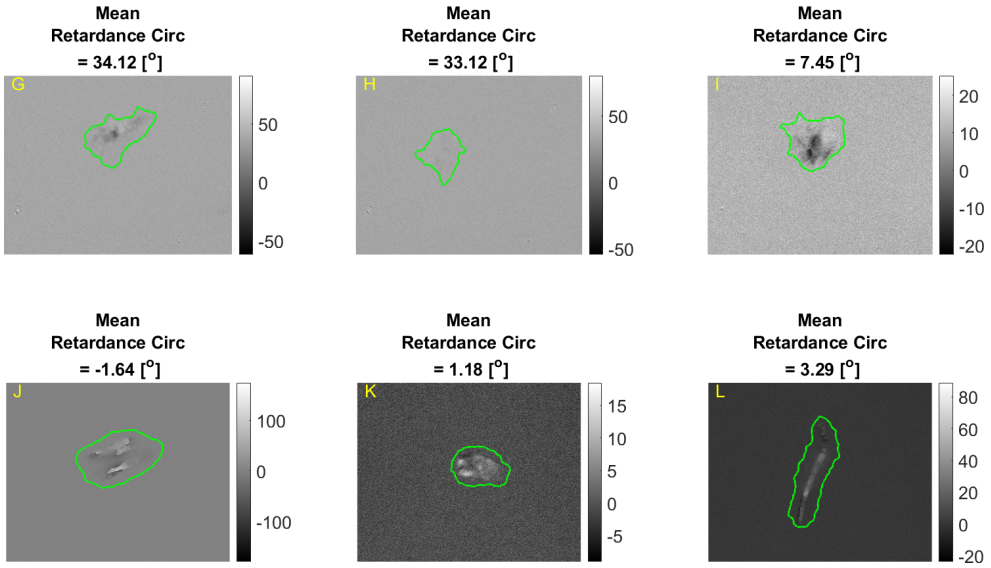

Figure 3.18: R_C maps for six deposits in posterior layers of retinal tissue samples from subjects with AD, presumably associated with AMD. Green contours represent the boundaries of the masks used in calculating the mean polarization signals, and were based on the Euclidean distance image segmentation method by Mason [115].

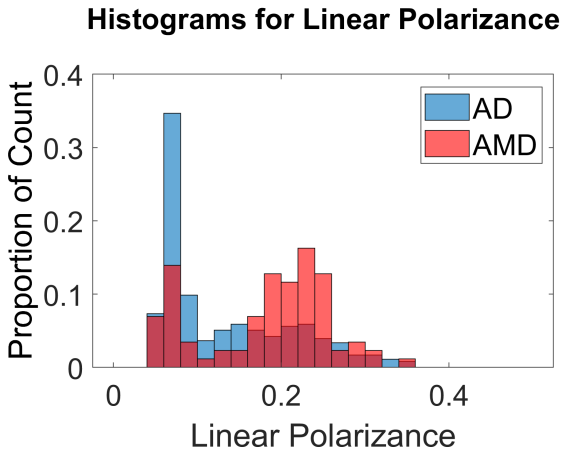

Figure 3.19: Linear polarizance (P_L) histograms for deposits associated with AD brain pathology and those presumably related to AMD, illustrating the overlap between the two sets of values associated with the respective groups of deposits. Note that the values of each bin in either histogram is represented here as the ratio of the number of observations within that bin to the total number of observations for that group, as a means of normalizing the proportions of deposits with particular P_L values. Both mean values and distributions of values are significantly different.

have significantly lower mean transmission values than anterior deposits.

There is a difference on average but some overlap in the examples shown in figures 3.17 and 3.18, which illustrate the R_C signals from the same deposits as in figures 3.15 and 3.16. The mean R_C values for the posterior deposits are greater than those of anterior deposits which have more values less than zero. After transmission, the three most significant p_{KSA} values were for circular signals. In the Wilcoxon tests, the three most significant p-values were all based on polarizance signals. In spite of the highly significant statistical difference between these groups of deposits and the others considered in this chapter, there was still substantial overlap between the ranges of values observed for both groups, both in polarimetry and MFA. See figure 3.19 for an illustration of this effect based on the results for mean P_L measurements of the deposits in both AD and AMD groups. The extent of overlap in this case and other metrics considered in this chapter led to some consideration of other techniques for increasing the extent of separation between compared groups of retinal amyloid deposits.

Alzheimer's Disease and Other Neurodegenerative Diseases

The group of 356 AD associated deposits (which were the anterior deposits used in the comparison of AD versus presumed AMD and intermediate severity of brain pathology versus high severity) were used as a single group again and compared to 127 deposits associated with other neurodegenerative diseases (NDDs). A few deposits whose MFS had a single peak were excluded from some of the MFA statistics. Of the MFA metrics, those related to peak-width provided the most significant statistical separation of deposits in these two groups. Since similar metrics were well suited for the statistical separation of AD versus AMD as well, an additional textural metric, entropy E (a non-MFA metric), was calculated for each R_L map in both groups. E was calculated using the built-in Matlab `entropy` function [112] based on the expression shown in equation 3.4. Deposits associated with non-AD NDD brain pathologies had statistically higher E than those associated with AD brain pathologies, with $p_{2WIL} < 10^{-10}$ and $p_{KSA} < 10^{-08}$ both much less than the Bonferroni significance threshold for the texture metrics of $0.05/15 \approx 0.0033$ (as there were 14 MFS-related metrics as well as entropy that were used to compared textures of the deposits associated with these two groups). Conversely, E was not different on average for the deposits associated with AD brain pathology and deposits presumably associated with AMD, with p_{2_WIL} and p_{KSA} both > 0.001 and the associated Bonferroni corrected threshold set to $0.05/(17 * 15) \approx 0.0002$ (17 sets of MFA parameter configurations and the same 15 measures of complexity).

Polarization signals differ between the groups much more significantly than the MFA test that was performed. In particular, mean R_L highly significantly separates AD brain pathology associated deposits from non-AD NDD brain pathology associated deposits (see figure 3.20). This might indicate differences in thickness and/or the birefringence properties of the two groups, which in turn is plausibly connected to different structures and deposition mechanisms. Recall that mean R_L was not different on average between the deposits associated with AD brain pathology and those presumably associated with AMD. Future multivariate analysis could investigate whether the combination of MFS-related metrics, E, and polarimetry, could distinguish between deposits associated with AD, AMD, and non-AD NDDs simultaneously (see table 3.7).

3.3.2 Composite Metrics

Statistical tests revealed that both MFA and polarimetry distinguished between the key groups. Combinations of metrics were considered briefly and showed promise for furthering the extent of separation between key groups, which is of importance as values for several

Metric	p_{2WIL}	p_{KSA}
x	-	2.80E-04
t	1.51E-14	0
b	3.11E-13	3.56E-10
T	1.81E-23	0
R_T	1.06E-21	0
R_L	3.80E-55	0
R_C	5.31E-16	0
Q	-	7.33E-04
P_T	3.72E-15	0
P_θ	4.88E-05	4.44E-08
P_L	1.50E-14	0
P_C	1.58E-15	0
D_T	8.86E-18	0
D_θ	1.34E-11	2.97E-09
D_L	4.94E-07	4.71E-06
D_C	3.10E-21	0
DI	-	2.50E-04
A_T	3.12E-24	0
A_θ	1.64E-04	-
A_L	2.34E-08	2.51E-06
A_C	1.49E-20	0
$A*$	4.22E-15	0
E	3.43E-11	2.17E-09
kurtosis	2.73E-08	7.17E-09
peak ratio	7.74E-09	1.91E-07
peak sep	2.65E-03	8.52E-05
prom ratio	2.81E-06	2.15E-05
width ratio	2.44E-12	0
$x1$	3.42E-05	1.02E-05
$w1$	1.74E-11	5.23E-11
$x2$	2.45E-03	9.98E-05
$w2$	6.82E-07	3.42E-05
$p2$	5.44E-06	7.47E-06

Table 3.7: P-values associated with polarization signals and MFA peak-related metrics, for separating deposits from subjects with AD (and possibly CVD and/or CAA) and those from subjects with various single non-AD NDD pathologies. p_{2WIL} corresponds to a 2-sided Wilcoxon p-value, and p_{KSA} corresponds to an asymptotic Kolmogorov-Smirnov p-value. Dashes for the polarimetry metrics represent p-values that were not below the Bonferroni corrected threshold of 0.0021 and in the MFA results the dashes represent p-values that were not below the Bonferroni corrected threshold of $0.05/15 \approx 0.0033$.

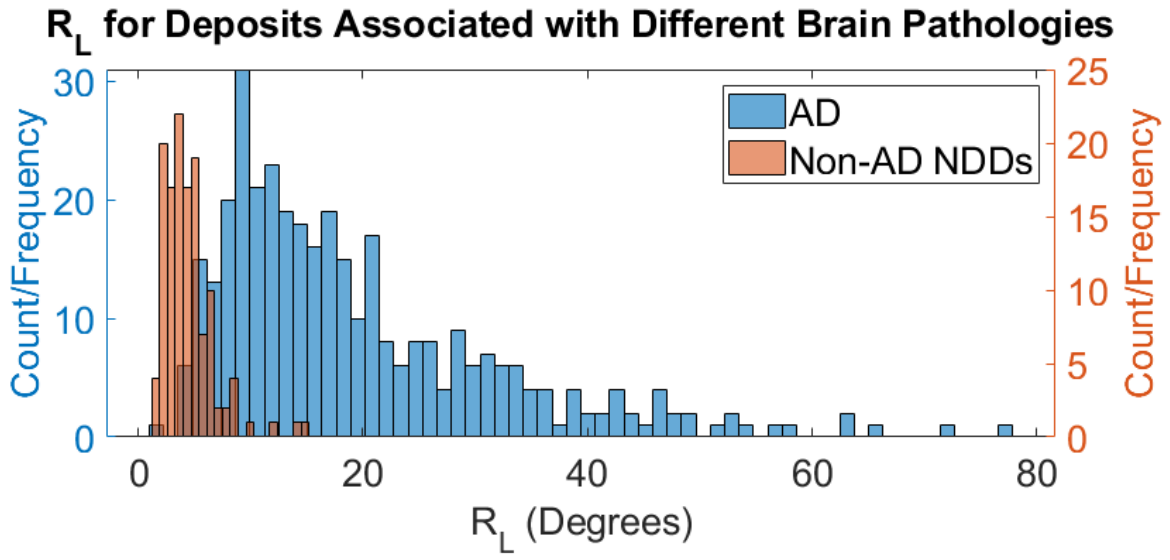

Figure 3.20: Histograms for mean R_L of deposits associated with AD brain pathology and other non-AD NDD brain pathologies. The darker orange region indicates overlap between the histograms. Both the means and distributions of deposits differ.

of the tested metrics showed substantial overlap between compared groups. For instance, deposits associated with AD brain pathologies were statistically separated from those associated with other NDD brain pathologies by D_T and MFS width ratio in different directions (i.e. the "AD" group had higher D_T and lower width ratios than group "non-AD"). There is substantial overlap in the histograms associated with both metrics (figures 3.21a, and 3.21b). A composite figure-of-merit of width ratio divided by D_T was calculated and is shown in figure 3.21c. This figure-of-merit provided greater separation between the histograms, and this approach could be considered in the future as a means of improving the statistical differences between groups and developing more specific identifying metrics for categorizing deposits based on their MFSs and polarization signals.

3.3.3 Resolution Tests

The results from the digitally reduced resolution tests are shown in figures 3.22a-3.22d. Most of the p-value trends associated with peak-related metrics became less significant with decreased rescaling factors (i.e. lower simulated magnification). This was expected because the metrics are linked to texture and complexity, and lower rescaling factor meant less

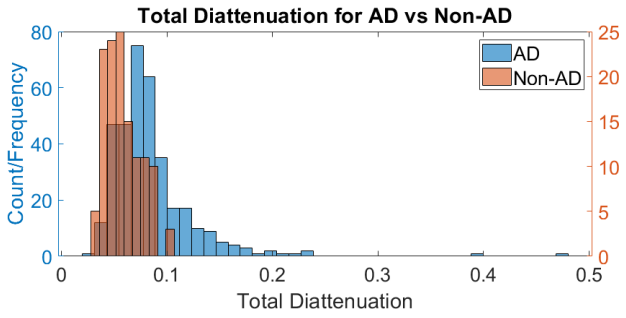

(a)

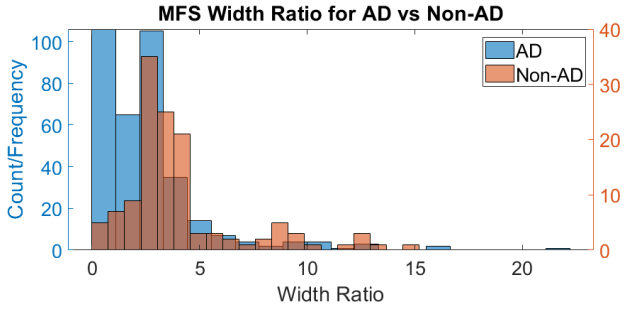

(b)

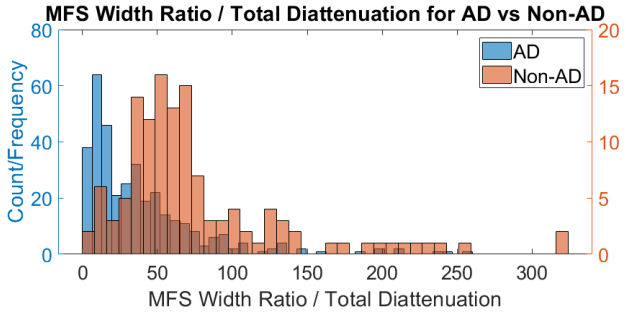

(c)

Figure 3.21: Illustration of histograms for the results of total diattenuation (D_T) and the MFS width ratio. The AD group represents deposits from subjects that had AD brain pathology and may have also had CVD and/or CAA, whereas the non-AD group were deposits from subjects that had other non-AD NDD brain pathologies. The results in 3.21a and 3.21b show substantial overlap in spite of statistically significant differences in means and distributions between the AD and non-AD NDD groups. In 3.21c, the histogram represents a figure-of-merit calculated by $widthratio/D_T$ which appears to separate the histograms of the AD and non-AD NDD groups more substantially than either individual metric.

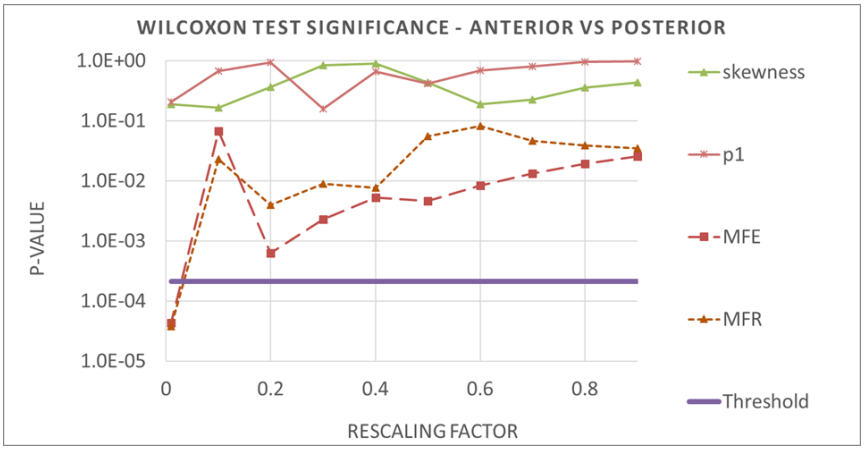

(a)

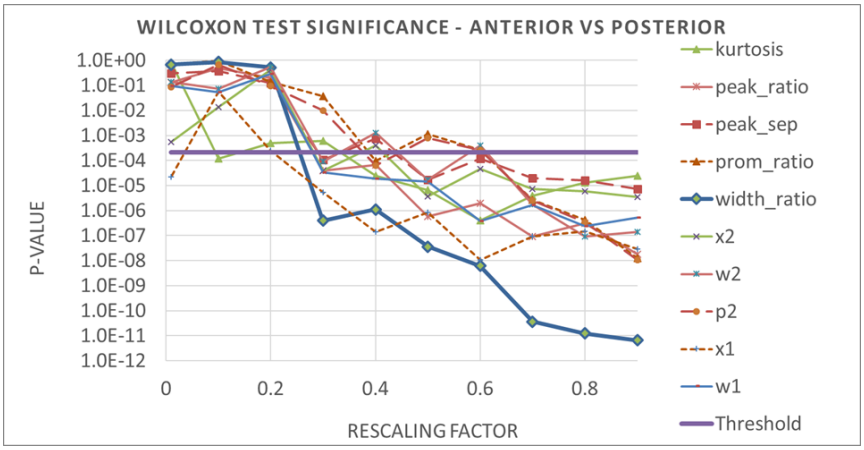

(b)

textural information was retained. Consider the MFSs shown in figure 3.23. As the scaling factor decreases from 0.9 to 0.2, the MFSs broaden but are still very similar, especially for $\alpha < 0.3$ in this case. However, for the rescaling factor of 0.1, the inflection between the two peaks in the MFS is effectively lost, and when the scaling factor is decreased further to 0.01, the MFS produced does not resemble the other MFSs in the figure. With this disconnect in mind, it is reasonable that most of the metrics behaved differently between the smaller two rescaling factors than they did through the remainder of rescaling factors.
Other tests were performed based on R_L maps taken with different objectives. These were processed by first increasing the number of pixels corresponding to the deposit at lower magnifications so that each R_L map had roughly the same number of pixels describing the

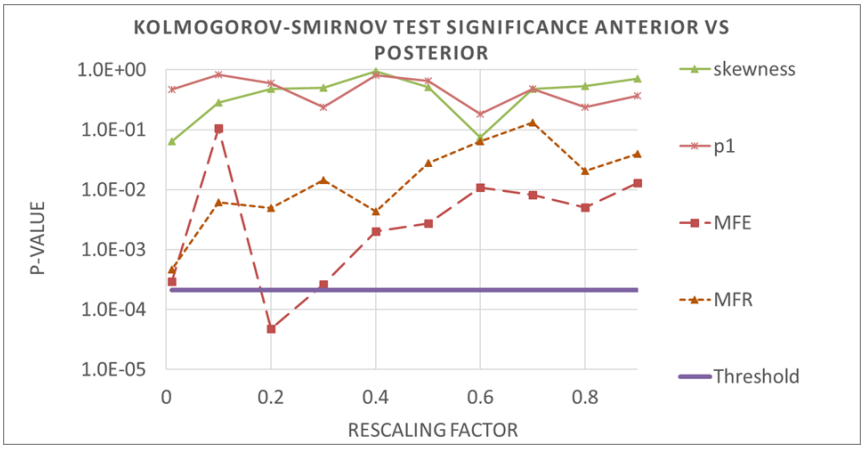

(c)

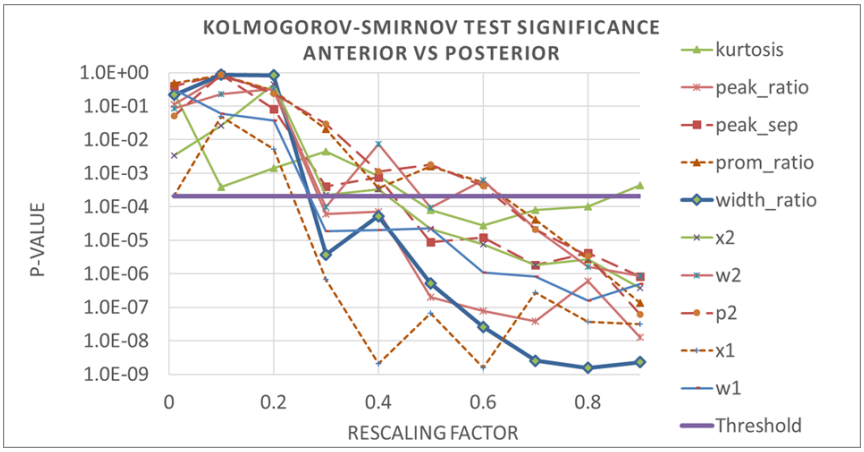

(d)

Figure 3.22: Plots of p-values as a function of rescaling factors for statistical tests that compared MFS-related metrics related to anterior deposits associated with AD and posterior ones presumably associated with AMD. The horizontal "Threshold" line represents the Bonferroni corrected significance threshold. The metrics are shown in groups with similar responses to the rescaling factor changes. R_L maps were shrunken by the rescaling factor to simulate having fewer pixels associated with the region enclosing the deposit, as would be the case if the raw images were taken with a lower magnification objective. The R_L maps were then enlarged by the reciprocal factor to ensure that the final number of pixels in each R_L map was approximately the same, which is important for the MFA.

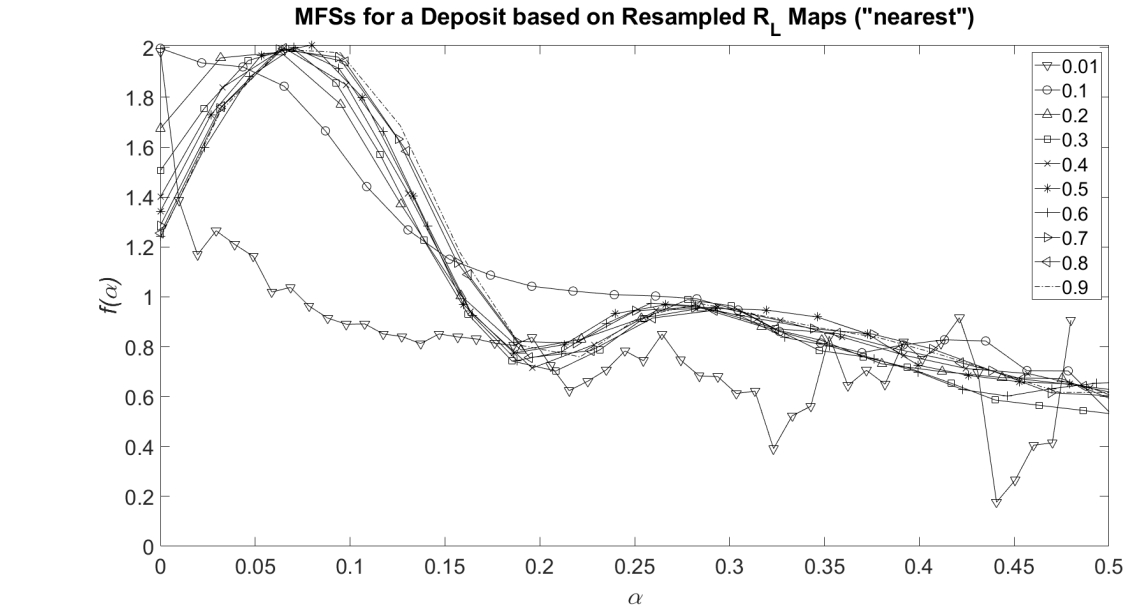

Figure 3.23: MFSs created based on R_L maps resized with different scaling factors. The factors shown are those by which the R_L maps were shrunken before being enlarged by the reciprocal factor. This ensured that the pixel dimensions of the image were nearly unchanged but information was still lost during the image-shrinking, simulating lower magnifications. The spectra were calculated using $Hvec$: 1:2:17, $Svec_{min}$: 1, capacity: max.

deposits. Since the lower magnifications also cover a larger physical area within the retina, they were then cropped so that their spatial dimensions were equivalent to those in the 40X R_L maps. See figure 3.24 for an example (as well as figure A.7 in Appendix A). The R_L

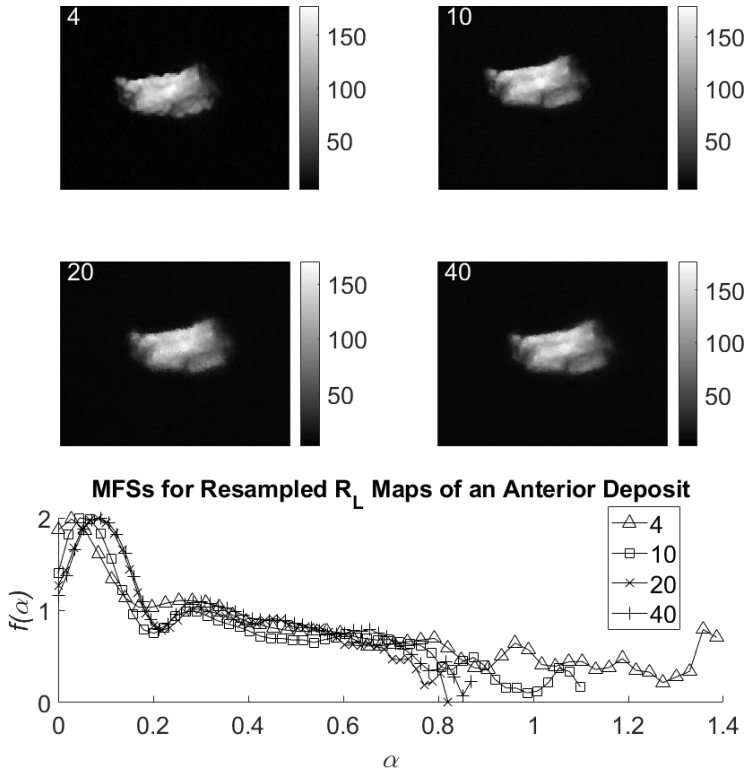

Figure 3.24: R_L maps calculated for a Mueller matrix based on images taken with different magnifications (see figure labels), and the corresponding MFSs indicating the impact of physically different resolutions. The factors shown are those by which the R_L maps were shrunken before being enlarged by the reciprocal factor. The spectra were calculated using $Hvec$: 1:2:17, $Svec_{min}$: 1, capacity: max

maps associated with the 4X objective, and thus the most substantial interpolation (and enlarging), generally had less smooth features, presumably due to a pixelization effect - an artifact of the interpolation. However, the MFSs are very similar for the examples in figure 3.24, especially for $\alpha < 0.8$. This may indicate that MFS related metrics that are more heavily influenced by the low α portion of the MFS will be more robust for the live-eye device. Across these tests it was observed that the sharpness of the peaks decreased with lower objectives, with an apparent smoothing of the MFSs. Note that the raw data for 4X

objective images corresponds to pixel dimensions of ≈1.6μm which is still much smaller than the presumed optical resolution of a live-eye imaging device.

Other examples of MFS tests for R_L maps taken using different objectives revealed that in some cases the background features were visibly different in the lower objective R_L maps. This was likely due to major differences in depth of focus as the cellular structures change with depth, and as described in chapter 2 so too can the structure of the deposit.

3.3.4 Depth-Resolved Multifractal Analysis

The differences in MFSs based on R_L maps taken with different objectives was a substantial motivator for the depth-resolved MFA. The primary intention of this was to study the manner in which texture changes with depth within the FITC channel of several confocal z-stacks, and also to determine whether there could possibly be a range of depth within the deposit that produces similar MFSs.

For the deposit shown in figure 2.11a, the depth-resolved MFS of the FITC channel (shown in figure 3.25) had interesting features, including a peak in spectrum width at slice 34. This sharp peak implies that the MFS becomes much broader within a narrow depth region surrounding slice 34. Incidentally, the histogram of levels in the FITC channel, as tracked by ZEN software, revealed that the width of histogram of FITC gray levels also peaked in this region, either at slices 34 or 35 approximately. This implies, as one would expect, that the slices with more grey levels tend to have the possibility for sharper image singularities, and hence higher Hölder exponents.

The region associated with Hölder exponents greater than ≈ 0.25 in this case is the portion of the spectra most likely to be substantially influenced by the finer details in the z-stack. Within this region of broader α, there are a few consecutive slices with lower Hausdorff dimension F. These slices also seem to correspond with the range in which the textural features of the deposit are most well defined. Hence, this particular example seems to contain a region of several slices with similar MFS around the depth in which the deposit is best focused.

The deposit shown in figure 3.26b has its depth-resolved MFS shown in figure 3.27. This deposit appears to be composed of several structures that might have coalesced into a single deposit due to their proximity. The large scale structure of this deposit changed between slices 25, 45, and 65 but in general, the texture of the deposit remained unchanged until little of the deposit is visible (see figures 3.26a to 3.26c which illustrate several slices with different features). These large scale structural changes may correspond with z-slices that had broader MFS. For slices less than 70 in which the deposit is well-defined, the actual

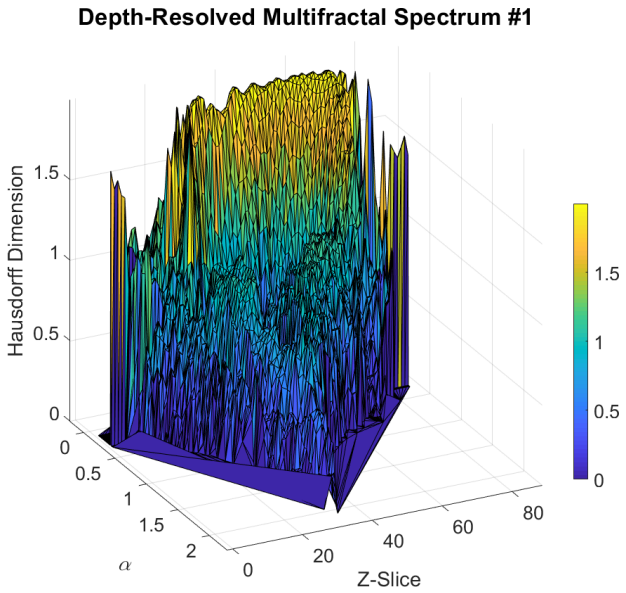

Figure 3.25: Surface representation of the MFS for each slice in the FITC channel of a z-stack (see figure 2.11a); $Hvec$ 1:2:17, $Svec_{min}$ 1, capacity: *max*. Notice the dip in Hausdorff dimension near slice 34.

Hausdorff spectra do not change dramatically, with the exception of the noted changes in spectrum width. This suggests that though the features contained in the different layers vary the overall texturedness and complexity of the deposit does not change substantially.

The depth-resolved MFS of the deposit shown in figure 2.13 was also analyzed. As discussed in chapter 2, this deposit appears to bend around a vessel. Due to the lack of symmetry in the z-direction, one might expect the associated MFSs to differ substantially layer-to-layer. The depth-resolved MFS is shown in figure 3.28. The widths peak at slices 26 and 49, but the actual Hausdorff spectra associated with these slices and those between do not vary substantially (figure 3.28), with the exceptions of a few slices that have notably lower F (in the lower α regions of the MFS). The general smoothness of this MFS is likely an indication of the continuity of texture across the deposit, in spite of the fact that different portions of the deposit are visible in any particular slice.

There were cases in which deposits within the same retina had similar spectra but this does not appear to be the norm. The deposits in figures 2.2 and 2.11d (in a retina associated with AD) appear to be an example of deposits with similar MFSs (figures 3.29a and 3.29b). Common features between these two depth-resolved MFSs include the regions

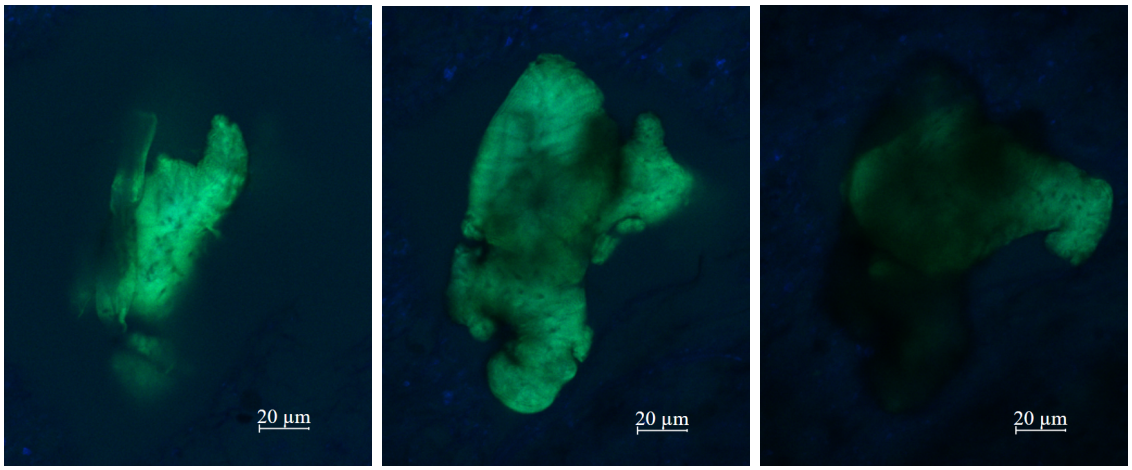

(a) Slice 25 (b) Slice 45 (c) Slice 65

Figure 3.26: Slices from the z-stack associated with the depth resolved MFS in figure 3.27.

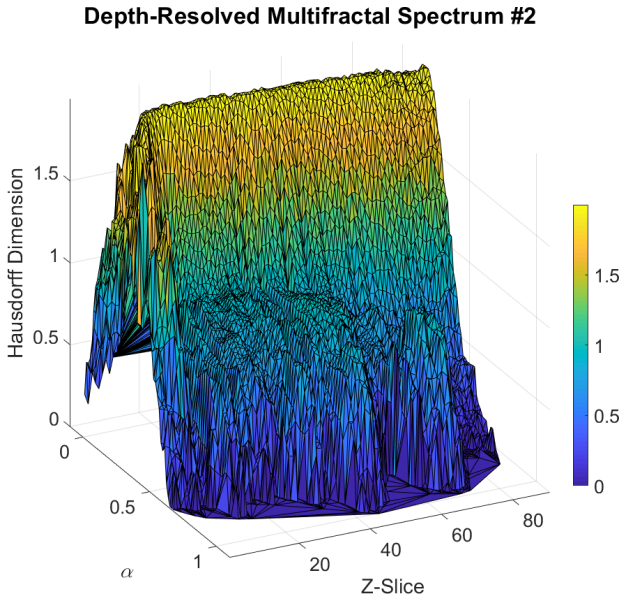

Figure 3.27: Surface representation of the MFS for each slice in the FITC channel of a z-stack. Very little deposit is visible beyond slice 70 (see figure 3.26); $Hvec$ 1:2:17, $Svec_{min}$ 1, capacity: *max*.

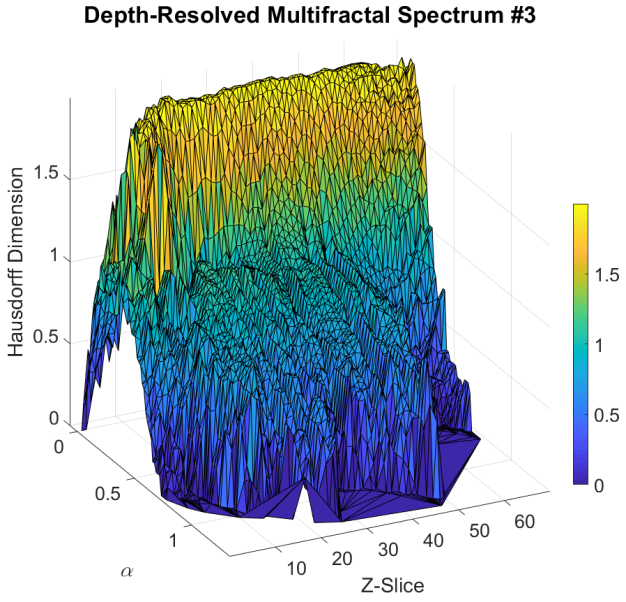

Figure 3.28: Surface representation of the MFS for each slice in the FITC channel of a z-stack (see figure 2.13d for a 3D view in the *en face* direction); $Hvec$ 1:2:17, $Svec_{min}$ 1, capacity: *max*.

associated with primarily background pixels (here shown in yellow). Also, the first peaks in the spectra remain around the same width at different depths, and both have broadest spread of Hölder exponents around slice 15-25 and minimum spectrum widths around slices 30-35.

Another two examples of deposits from a single retinal sample for which the depth resolved MFSs are similar, are illustrated in figures 3.29c and 3.31. Again the range of Hölder exponents that are present changes with depth in similar ways between the two deposits. Beyond the spread of Hölder exponents, the first peak, or ridge in the context of the three dimensional visual, changes in similar ways, with the peak broadening with depth, but also shifts towards lower Hölder exponents around the 30^{th} slice.

Contrary to the predicted behaviour, MFSs for deposits from the same retina are not typically similar to this extent. More commonly deposits within a particular retina can have different depth-resolved MFSs, with differing locations and extents of peaks. For example, consider the deposits shown in figures 3.32a and 3.32b which are deposits with visibly similar structure. Despite their macro-scale similarities, the depth-resolved MFSs (see figures 3.33a and 3.33b) differ in most aspects. Though both spectra reach similar ranges of Hölder exponent values (between 1.5 and 1.7), the deposit shown in figure 3.32a

has broader spectra for most slices, whereas the deposit in figure 3.32b only has a few slices with such broad spectra, implying only a few slices have this level of variance in texture. Additionally, the deposit shown in figure 3.32a has a more clearly defined second ridge, which extends through 25 slices as opposed to the other deposit which has a weaker set of second peaks that are only distinct in approximately slices 10-15. One possible reason for the broadness of the MFS of the deposit shown in figure 3.32a is evenness of the tissue surrounding the deposit.

The analysis described earlier which compared the MFSs of deposits associated with different pathologies indicated that there are similarities between deposits that share pathological associations, so further analysis is required to determine how this is manifested in the depth-resolved MFSs. The depth-resolved MFSs described herein were all calculated using $Hvec = 1 : 2 : 17$ and $Svec_{min} = 1$, and have voxel sizes of 0.44μm as opposed to the 0.16μm pixels used in the polarimetry analysis. This depth resolved analysis could be repeated with the MFA settings for $Hvec$ and $Svec_{min}$ adjusted to account for the differences of the pixel dimensions, so that it could be used to investigate depth-resolved properties of textures on similar scales to those present in the polarimetry images.

Voxel Magnification Test

A test was performed to compare the depth-resolved MFSs of two z-stacks taken of the same deposit with different voxel sizes. The spectra are shown in figures 3.34 and 3.35. The difference in voxel dimensions and resampling process had a significant effect on the crispness of the edges in the *en-face* projection belonging to the z-stack that was imaged with 1.00 μm voxels. However, the MFSs are still strikingly similar, having peak spectral widths at similar slices, and with similar F within each spectrum. This result of a larger depth voxel agrees with the suggestion that the differences in MFSs for R_L maps generated for single deposits with different objectives were primarily due to differences in depth of focus. In figures 3.34 and 3.35 the MFSs clearly change with depth. However, the rate of change in MFSs associated with consecutive slices appears to be gradual and largely continuous. This observation, paired with the similarities in the MFSs in spite of the difference in initial pixel dimensions, suggests that the MFA described earlier for separating deposits associated with different pathologies may be robust to changes in image depth, and different foci.

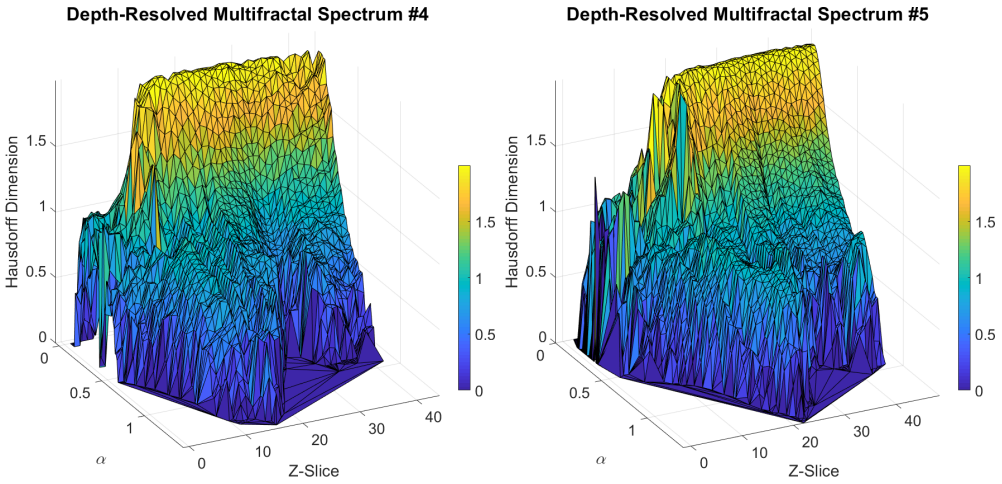

(a) (see figure 2.2)

(b) (see figure 2.11d)

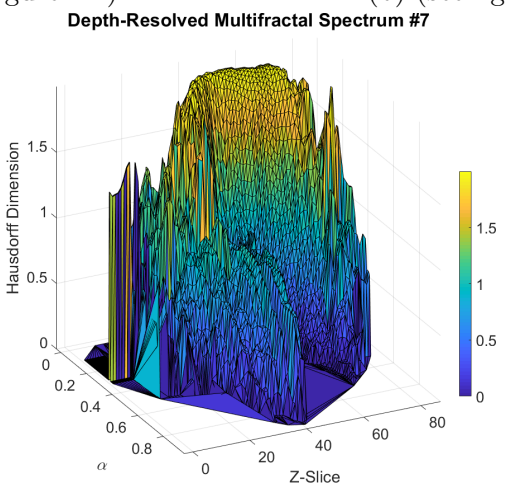

(c) (see figure 2.11f)

Figure 3.29: Surface representations of the MFS for each slice in the FITC channel of z-stacks, with $Hvec$ 1:2:17, $Svec_{min}$ 1, capacity: max.

Figure 3.30: Slice 38 of the z-stack associated with the depth-resolved MFS in figure 3.31.

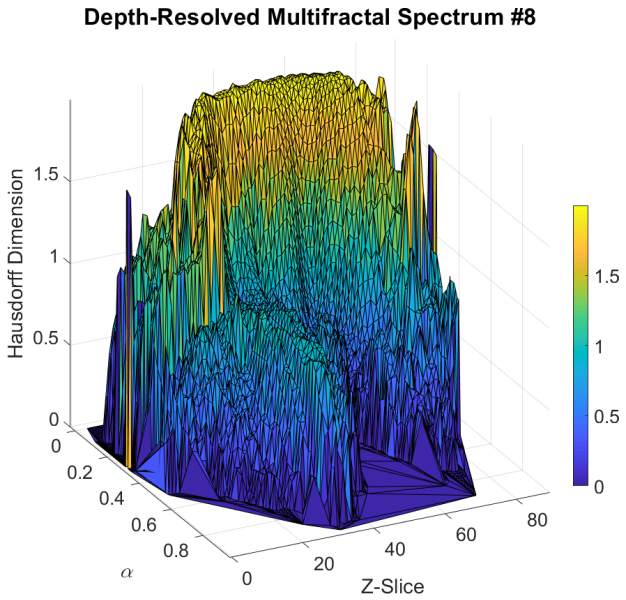

Figure 3.31: Surface representation of the MFS for each slice in the FITC channel of a z-stack (see figure 3.30); $Hvec$ 1:2:17, $Svec_{min}$ 1, capacity: max.

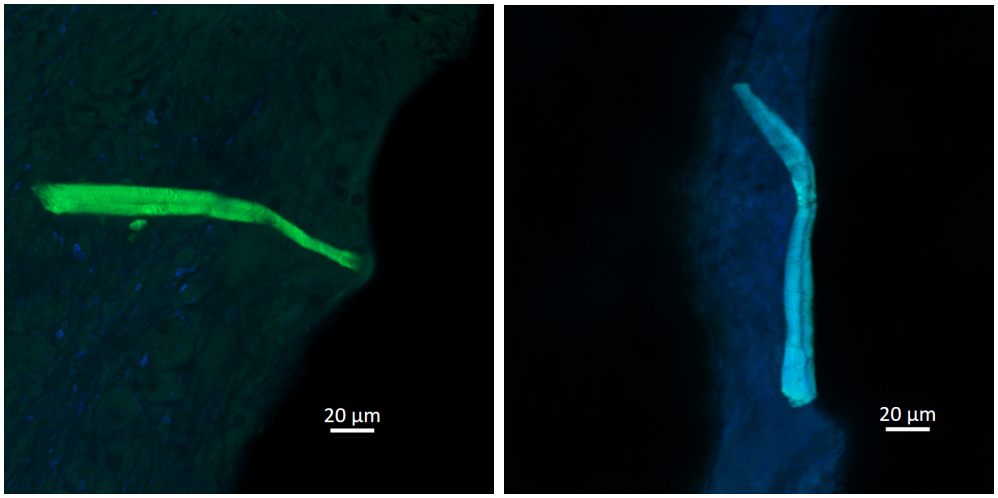

(a) (see figure 3.33a) (b) (see figure 3.33b)

Figure 3.32: Slice 20 of the deposits associated with the depth resolved MFS shown in figures 3.33a and 3.33b, respectively. Note that both deposits have morphologies that may be consistent with vessel-association (more obvious for the deposit on the right).

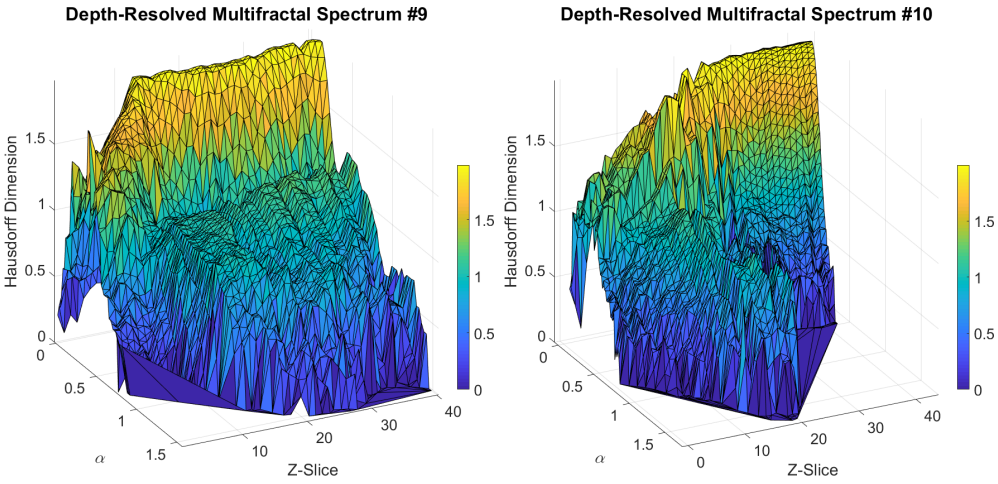

(a) (see figure 3.32a) (b) (see figure 3.32b)

Figure 3.33: Surface representations of the MFS for each slice in the FITC channel of z-stacks, with $Hvec$ 1:2:17, $Svec_{min}$ 1, capacity: max.

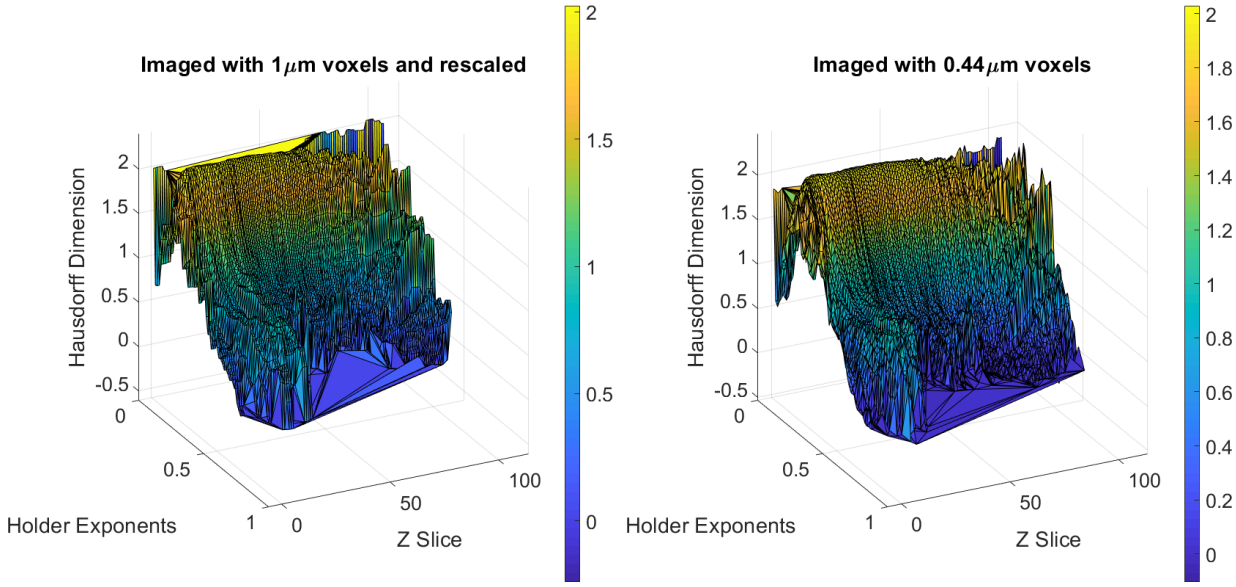

Figure 3.34: Depth-resolved MFSs for two z-stacks of the same deposit, 3D view.

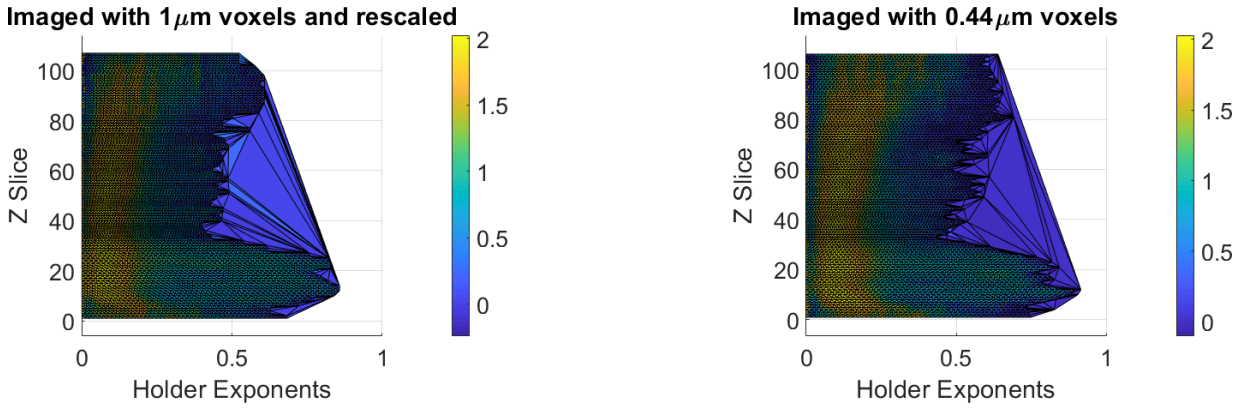

Figure 3.35: Depth-resolved MFSs for two z-stacks of the same deposit, 2D view of 3.34 (from above); colours correspond to F.

3.4 Discussion

3.4.1 Multifractal and Polarimetric Analyses of Different Pathologies

In this chapter, it was shown that multifractal analysis and polarimetry had significantly different average values between deposits associated with different severities of AD brain pathology, with AD brain pathology and those presumably associated with AMD, and with AD brain pathology and those associated with other NDDs. In this work, the statistical differences in the averages of various MFS and polarimetric properties were assessed to determine which properties might be useful in the future in giving a high accuracy of classification of the deposits. The next step would be to perform such a classification using multiple properties. Ultimately, the results of these group comparisons indicated the potential for complexity/texture analysis and polarimetry as a means of distinguishing between deposits associated with different pathologies.

3.4.2 Differences in Amyloid Deposit Properties with Severity of Alzheimer's Disease pathology

We have previously shown that the number of amyloid deposits is correlated with the severity of AD brain pathology, including overall pathology and amyloid pathology [54]. Here we studied some of the retinas included in that study to determine if there are differences in the properties of the individual deposits. The properties of retinal amyloid deposits that were highly significantly different between individuals with an intermediate severity of AD brain pathology and high severity of AD brain pathology were the MFS metrics related to overall broadness of the spectrum and spectrum kurtosis and the polarimetry metric total diattenuation. Similar to the analysis of the number of amyloid deposits in the retina [54], the results of this chapter indicate that properties of individual retinal amyloid deposits differ as a function of severity of AD brain pathology. The significant difference in diattenuation with severity suggest either a change in structure of the deposits that causes differential absorption of polarized light states. This is consistent with the observation that there is also a statistical difference in the mean total retardance values for the deposits found in association with different severities of AD brain pathology (though the other component retardance signals did not have statistically significant Wilcoxon test p-values).

Transmission, MFA metrics related to individual peak widths, and peak separation, were significantly different for retinal deposits associated with AD brain pathology compared to those presumably associated with AMD. MFSs associated with deposits in the posterior retina more commonly had multiple distinct peaks, sharper first peaks, broader second peaks, and less separation between peaks. This is consistent with deposits imaged in the posterior retina having more well-defined edges and structural features. The polarimetric properties that best separated the two sets of deposits were polarizance-based signals and circular signals as well (i.e. circular retardance, etc.). Although the averages of these properties were highly statistically different for the two groups, the values among the groups still overlapped (see figure 3.19 for an example).

Besides our group, others have reported the occurrence of retinal amyloid in association with AD [55, 35, 49, 56] and AMD [87]. Connections and pathophysiological similarities between AD and AMD have been reported on extensively [119, 120]. One such group analyzed retinal tissue from some members of the same population studied by our group and found that intermediate hard drusen in the temporal retina was more commonly found in retinas associated with AD brain pathology than in retinas from older normal subjects [89]. Our results that the anterior amyloid retinal deposits expected to be associated with AD differ in shape, textural properties and their interaction with polarized light from those found in the posterior retina (expected to be associated with AMD) is consistent with the two sets of deposits representing different pathologies, associated with AD and AMD. The evidence within this chapter that amyloid occurs in the retina in different morphologies in association AD and AMD and that deposits of both kinds can form in the same retina could be due to similar underlying risk factors, pathophysiology [120], and general unhealthy ageing.

This study assumed that amyloid deposits in the anterior retina were related to AD because amyloid deposits in the brain commonly form through the cleaving of the amyloid precursor protein across neural cell membranes [121]. In contrast drusen are associated with AMD, and are found between the retinal pigment epithelium and Bruch's membrane [88]. Some drusen have previously been reported to contain amyloid [86, 87]. The conclusions drawn here would be strengthened if studies could be performed on retinas where there was a differential diagnosis of AD pathology in the brain (as in the samples used here) and a differential diagnosis of AMD prior to death.

3.4.3 Differences Between Amyloid Deposits due to Alzheimer's Disease and those due to Other Neurodegenerative Brain Pathologies

An attempt was made to separate amyloid deposits found in retinas of those with AD brain pathology and those with other NDD brain pathologies. This was a proof of concept study in which only a single set of MFA settings was tested. A highly significant difference was found in the average values of metrics related to widths of individual peaks and R_L. Because the MFA metrics which gave significant differences for AD versus non-AD NDDs and AD versus AMD overlapped, entropy E was considered for both comparisons. This metric was only statistically different on average between AD brain pathology related deposits and those related to other NDD brain pathologies, and not significantly different between deposits associated with AD brain pathology and those presumably associated with AMD, as was the case for R_L.

3.4.4 Potential for Distinguishing Between Multiple Conditions in a Single Analysis

Comparisons of properties of retinal amyloid deposits were performed across paired groups of different pathological conditions. In each case, there were highly statistically different properties. The ones with the highest significance also differed for different pairs of conditions, except for the ones associated with the widths of individual peaks which were different on average for two pairs of conditions. Entropy then provided a measure which was only significantly different for one of those pairs. Composite metrics were considered briefly and improved separation in the comparison of deposits associated with AD brain pathology and those related to other NDDs. The analysis presented here suggests that a more complex linear discriminant or machine learning analysis could separate all of the conditions considered above on the basis of MFA and polarimetry properties. The techniques described above, once implemented in live-eye imaging (see below) could be used to track changes in the properties of individual deposits over time (for example as the brain severity of disease in AD increased over time) or as a function of therapeutic treatments which might ameliorate the severity of disease.

3.4.5 Applicability of the Techniques Studied to Live-eye Imaging

The utility of MFA has been demonstrated for a variety of biomedical imaging applications. For example, MFA has previously been shown to be capable of identifying/segmenting microcalcifications in mammograms [107], and other abnormalities in breast tissue samples in observations of fluorescence *in situ* hybridization [100]. One of the aims of this work was to explore whether techniques of differentiating the various conditions studied would be usable at the lower magnifications associated with live-eye imaging. Polarimetry proved a powerful technique for diagnosing glaucoma via the detection of the thickness of the optical nerve fiber layer in the living eye [122, 123]. Depth-resolved MFA has been performed (through an approach distinct from that presented herein) on optical coherence tomography (OCT) images in living eyes of subjects that had ocular diseases and healthy controls [124]. That group concluded that depth-resolved analysis of the "multifractality" of OCT images could be used for early detection of retinal diseases. Though the specific form of MFA and techniques used were different, their work supports the prediction that characterization of texture and complexity of retinal amyloid deposits through MFA could be relevant for distinguishing between deposits associated with different pathologies, as is the main result from this chapter.

Both multifractal analysis and polarimetry may perform differently in the live-eye than in tissue for a variety of reasons including resolution, focus, and differences between live-eye and fixed tissue. In testing the potential for live-eye imaging, the lower magnifications used needed to be tested. It was found that although simulating lower magnifications by reducing the number of pixels in the R_L maps led to less significant statistical separation of the anterior and posterior deposits, some multifractal metrics were highly significantly statistically different between AD and AMD deposits in spite of simulated changes in magnification of over 0.5 (or 50%). This indicates a degree of resilience against changes in magnification that could be important for a live-eye polarimeter. Furthermore, comparisons of multifractal spectra based on images taken with physically different magnifications (from different objectives) for a small subset of the deposits showed that the spectra may change in predictable ways at lower magnifications, with some similarities between spectra apparent for images taken with objectives that differ in magnification by a factor of 4 from the initial microscopy images (used in the bulk of the analysis presented in this chapter). Most MFSs broaden at lower resolutions, likely due in part to the loss of the finer details in the images. However, other differences between groups are expected to persist at lower resolutions, because in simulating lower magnifications of the deposits associated with AD brain pathology and those presumably related to AMD, some tests with pixel dimensions

equivalent to approximately 16 μm still found MFA metrics that produced statistically significant differences.

Depth-resolved multifractal analysis of confocal z-stacks of deposits revealed that there appears to be a range of slices within deposits that correspond to similar multifractal spectra. This suggests that the technique may be robust against slight changes in foci, which would be important for the live-eye device. This is also consistent with short range order in the deposits. Textural changes in retinal surround in *ex vivo* tissue caused by tissue preparation could alter the multifractal spectra somewhat as its calculation involves the tissue immediately around the deposit. In microscopic polarimetry measurements, the deposit structure is very similar to that of pure deposits on glass so the influence of the surrounding tissue appears small. However, the metric "transmission", used with the polarimetric metrics is the transmission of white light through the deposit and this would be affected by tissue above and below the deposit. Confirmation of the relationship between the MFSs of deposits and the surrounding tissue (or possibly lack thereof) could be performed by comparing MFS of segmented images of deposits in tissue to segmented images of pure deposits.

3.4.6 Conclusion

Texture analysis performed using MFA, and polarization signal analysis, both produce average values significantly different for deposits associated with different pathologies. Tests performed by resampling R_L maps, and considering z-stacks of confocal images suggested that MFA may be resilient against some changes in magnification and foci, respectively. The major impact of this chapter is thus the finding that MFA and polarimetry may be suited for distinguishing between deposits in the live-eye imaging device, and for providing diagnostic insight therein.

Chapter 4

Discussion

4.1 Morphological Analysis

Consideration of confocal microscopy z-stacks provided insights into the three-dimensional (3D) morphology of amyloid deposits in the anterior layers of human retinas from subjects with Alzheimer's Disease (AD). Some deposits in the retina were associated with presumed vasculature, and had structural features that resembled deposits that form in the brain in association with cerebral amyloid angiopathy (CAA). These included: deposits with ring-like cross-sections (figure 2.3b) which appeared to either fill vessel walls, or form between layers therein; deposits with banded patterns (figure 2.11b), presumably due to amyloid displacing smooth muscle in vessels (resembling those presented in [26]); cylinder-like deposits that possibly filled vessel lumina; and deposits that may have resulted from dyshoric changes, with the appearance of now being outside but touching presumed vasculature (figure 2.17), or both inside and outside the vessel (figure 2.14), consistent with some brain deposits in CAA. In CAA deposits usually begin by forming in the basement membrane [61], and then in severe cases proceed to replace full segments of vessels with amyloid, with the possibility of eventually disrupting the vessel and escaping into the surrounding neuropil [63]. The variance between these morphologies may correspond to different stages of vascular amyloidosis as has been described in CAA.

Vessel associated deposits were found in all examined retinas from subjects that had evidence of AD and CAA brain pathologies, in one retina that had AD and CVD pathologies but no evidence of CAA, and in one retina that AD with no evidence of CAA. These results may indicate that amyloid deposits form in association with retinal blood vessels through similar mechanisms as those that form in CAA in the brain, as suggested by Ko-

ronyo [35]. A vessel associated deposit was also found in a retina that was associated with multiple system atrophy but not with AD or CAA brain pathologies. The formation of vessel associated deposits in retinas from subjects whose brains had no evidence of CAA pathology may indicate that CAA pathology forms in the retina prior to its formation in the brain.

Some non-vessel associated deposits appear to have dark spots that shift laterally with depth. In some cases, these dark spots (or dark tunnels) were observed in deposits that were directly above or directly below retinal ganglion cells (RGCs). This indicates that the dark tunnels may be due to amyloid that has formed around (or been perforated by) RGC axons.

Strand-like features with diameters on the order of one micron, which may have been fibrillar bundles of amyloid, were found in several cases on the most anterior faces of deposits (both those that did and did not appear to be vessel related). It is also possible that some of the larger strand-like features in vessel associated deposits are actually amyloid that has accumulated in a capillary (which occurs in the brain in CAA of capillaries [33]), but most of the strand-like features observed herein were smaller than would be expected of an amyloid-filled capillary.

Lower amyloid levels in the vitreous are reportedly associated with decreased cognitive ability [78]. One of the possible fibrillar bundles of amyloid was found on the anterior surface of a deposit that was in or possibly on the optical nerve fiber layer (ONFL). This may suggest that amyloid deposits forming from the vitreous onto the retina, which is consistent with previous findings from our group that atomic force microscopy revealed the presence of thioflavin-S positive deposits close to the anterior surface of the retina [125].

4.2 Multifractal Analysis

4.2.1 Main Findings

Chapter 3 demonstrated the aptitude of multifractal analysis (MFA) for distinguishing between groups of deposits associated with different pathologies. These group comparisons were of deposits with different severities of AD brain pathology, those associated with AD brain pathology versus those presumably associated with AMD, those with different severities of AD brain pathology, and those with AD brain pathology versus those with other NDDs. For these comparisons, the group labelled as associated with AD brain

pathology could have also had cerebrovascular disease (CVD) and/or CAA in addition to AD. This is because CVD is not expected to be associated with a proteinopathy (though it may be connected to cholesterol), and CAA brain pathology is highly coincident with AD brain pathology [31, 33, 126, 127]. Differentiating between deposits from subjects who have differing single diagnoses of NDDs and others who have multiple brain pathologies would be the next major steps for these experiments. A combination of the morphological analysis, MFA, and polarimetry may be useful for this application, presuming deposits associated with different conditions have specific 3D macrostructures with differing interactions with polarized light.

4.2.2 Connections to Literature

Pirici *et al* found that fractal dimension analysis on amyloid deposits in human brains revealed differences in the complexity of immunostained amyloid-β signals (total and [1-42]) in diffuse plaques from those of other plaque phenotypes, and that the fractal dimensions of amyloid-β [1-40] deposits in brains associated with AD pathology were different from those found in brains of aged controls [34]. Fodera *et al* developed a model which determined that through electrostatic interactions, amyloid forms multifractal structures, predicting spherulite formation, and fibrils [128]. The extension that fibrils then proceed to form deposits through a multifractal growth process was not made. Though MFA of images does not require that the structure being imaged be truly multifractal, the hypothesis that retinal amyloid deposits form through multifractal growth processes paired with the results of chapter 3 which indicate that multifractal measures are suited for distinguishing between deposits associated with different pathologies, may be useful for future work in modelling the growth of retinal amyloid deposits and predicting multifractal signals of importance for particular applications.

Miyawaki *et al* performed both morphological and fractal analyses of amyloid-β plaques in canine brains [129]. Several similarities between this thesis and their work are noteworthy. They performed 3D analysis using a confocal scanning laser microscope to evaluate the morphologies of plaques. They calculated fractal dimensions (FD) of plaque silhouettes (not MFSs of the gray-scale images as calculated in chapter 3 for polarimetric images) for each image in their z-stacks, producing a representation similar to the depth-resolved MFSs shown in this work. Their study involved separate labels for amyloid-β [1-40] and amyloid-β [1-42](43). They concluded that the FD depth-dependent trend-line associated with amyloid-β [1-42](43) was approximately constant with depth. Though the plaques they presented have different morphologies to those studied using depth-resolved MFA in chapter 3, the notion that complexity of deposits may not change in depth was of interest.

By comparison, in retina, the results of chapter 3 suggested a slow change in complexity with depth. In turn, this may aid in the application of MFA to live-eye images, relaxing the precision with which a particular slice through the deposit must be imaged.

4.2.3 Statistics

The differences between multifractal spectra (MFSs), and polarization signals, of retinal amyloid deposits associated with different pathologies were characterized using Wilcoxon and Kolmogorov-Smirnov statistics. Histogram representations for the metrics associated with deposits from different pathologies often had substantial overlap, in spite of the highly significant statistical differences in their averages and distributions. Linear discriminant analysis (LDA) is a method for identifying linear combinations of observations that best separate the measurements into two classes (in our case, of differing pathologies) [130]. LDA requires that the data being analyzed be normally distributed, which is not the case for the polarization signals or MFS-related metrics in any of the groups studied in Chapter 3. Thus, a non-parametric equivalent of LDA, as a means of determining which combinations of metrics, both polarimetric and multifractal, are able to provide the greatest separation between the aforementioned groups of retinal amyloid deposits associated with different pathologies is being investigated. Textural/complexity-based differences between linear retardance maps of deposits associated with different pathologies were detected through MFA. Making use of both polarization signals and MFS-related metrics may provide a view into new means of classifying deposits for diagnostic purposes in the future live-eye imaging device.

4.3 Impact

On average, differences in structural and textural features of amyloid deposits in the retina appear to be related to different pathologies, including different brain pathologies. Differences between the morphologies of retinal amyloid deposits that form related to blood vessels and those that do not, point towards possibly different etiologies and constraints on the deposits from their environment. Resemblances between the blood vessel associated deposits in the retina and those found in the brain in association with CAA based on 3D morphological analysis suggests that they may form through similar mechanisms. Amyloid deposits associated with CAA and AD in the brain reportedly form through distinct pathways [131], with CAA reportedly forming as a result of failures in perivascular drainage pathways [32, 132]. The results of this thesis seem to support a similar hypothesis for

retinal amyloid deposits. In addition, structural features of amyloid deposits (including their interactions with polarized light), and their textural features which may be robust to changes in magnification, may be useful in a differential diagnosis of these conditions without need for expensive brain scans.

4.4 Future Work: Electron Microscopy for High Resolution Tomograms of Amyloid Deposits in Retinal Tissue

4.4.1 Motivation and Project Summary

Our group has predicted short range ordering amongst amyloid fibrils in retinal deposits [60]. The resolution of our optical microscopy techniques is inadequate for resolving fibrillar textures in deposits. To investigate fibrillar ordering, we are collaborating with another research group to perform electron tomography. Typical electron microscopes are able to attain resolutions of a few nanometers, and even less than 0.1 nm when aberration corrected. Recently, scanning transmission electron microscopes (STEM) have become very popular, and this technique will be used for this project.

4.4.2 Scanning Transmission Electron Microscopy

Transmission electron microscopy (TEM) at 100 kEV [133] works with very thin samples, on the order of 5-500 nm thickness that lay over a mesh grid. Electrons from the beam are incident upon the entire imaging region of the sample. Contrast is due to the Coulomb interactions between the accelerated electrons and the nuclei of the atoms they pass [133]. Electron beams are collimated by electromagnetic lenses. These beams can also be translated using scanning coils, and then focused with other electromagnetic objectives. The result of this is a STEM.

STEMs are able to attain sub-Angstrom resolution [134, 135, 136] once aberration corrected. The exiting beam can be focused further and passed through a magnetic prism (or a series of prisms) that spatially separates the electrons associated with different energy losses. A moving slit then selects a portion of the spatially spread electrons associated with each resolvable energy interval for detection [137]. Through this detection method, it is possible to measure the characteristic electron energy loss spectra (EELS) associated with

a sample. The combination of this spectroscopy and high spatial resolution can allow for researchers to both resolve the general crystal structure of a sample and to identify which atoms are at each position.

4.4.3 Electron Tomography

To collect an electron tomogram, a sample is mounted on a tiltable-stage[1]. Micrographs are acquired using the STEM for each angle. These images are combined to form a 3D rendition of the sample by means of a back-projection process [38]. In a study by Kollmer *et al* [38], amyloid deposits were grown within a cell culture. This study made use of an electron tomography technique, and led to several substantial results. Researchers were able to identify several different categorical arrangements of amyloid fibrils within deposits. They also found that fibrils were ordered, at least locally, which would support our group's presumption that there may be short range ordering between fibrils in different layers of deposits. Extracting equivalent information from retinal deposits will allow our group to evaluate their content and our hypotheses related both to the mechanisms through which retinal deposits form, and to better predict favourable polarization signals. Koronyo *et al* [35] included some experiments with a TEM in their analysis of retinal amyloid deposits, but we are unaware of any group that has yet performed any form of 3D electron microscopy imaging on retinal amyloid samples. EELS measurements with STEM indicate another avenue for this research - mapping the types of amyloid present in different retinal deposit features. EELS has been used previously to identify regions in a micrograph associated with different proteins based on sulfur content [138]. This combination of methods could eventually be used to gain specific information about the amyloids (and possibly other proteins or neuritic material) contained within a deposit[2].

4.4.4 Ongoing Work

We have begun collaborating with Grandfield and her students at McMaster University. Laura Emptage and I determined a sequence of ethanol baths that could adequately dehydrate a retinal tissue sample, and have tested this with canine and porcine tissues. A porcine tissue sample has been stained for the electron microscopy, and embedded in resin by Grandfield's group. We are currently testing these embedded porcine samples to ensure

[1] Multi-directional tilts are used in some cases but only a mono-directional tilts are adequate for our application.

[2] A 4D correlative analysis of this form has been performed previously by Grandfield's group [139].

that the deposit polarization signals remain distinct. Next, white light microscopy will be used to determine the tissue's post-staining integrity. A micrometer will then be used to measure the specific locations of several deposits within the samples. The samples will be polished to remove as much of the embedding resin from above the sample as possible. Afterwards, rectangular volumes will be lifted out of the bulk using a focused-ion beam technique. Once the lift-out is complete, the sample is loaded into the STEM for the electron tomography. If this is all successful, we will repeat the process with canine and human retinas.

Bibliography

[1] Ellen A Kramarow and Betzaida Tejada-Vera. "National Vital Statistics Reports". In: *National Vital Statistics Reports* 68.2 (2019).

[2] Alzheimer's Society Canada. *Dementia Numbers in Canada*. 2019. URL: https://alzheimer.ca/en/Home/About-dementia/What-is-dementia/Dementia-numbers (visited on 11/19/2019).

[3] Statistics Canada. *Neurological conditions in household population - Table 13-10-0467-01*. 2019. URL: https://www150.statcan.gc.ca/t1/tbl1/en/tv.action?pid=1310046701 (visited on 11/26/2019).

[4] Dennis J Selkoe. "Alzheimer disease and aducanumab: adjusting our approach." In: *Nature reviews. Neurology* (2019).

[5] Ron Brookmeyer et al. "Forecasting the global burden of Alzheimer's disease". In: *Alzheimer's & dementia* 3.3 (2007), pp. 186–191.

[6] GBD 2016 Dementia Collaborators et al. "Global, regional, and national burden of Alzheimer's disease and other dementias, 1990–2016: a systematic analysis for the Global Burden of Disease Study 2016". In: *The Lancet Neurology* 18.1 (2019), pp. 88–106.

[7] Kiren Ubhi and Eliezer Masliah. "Current state of the art in preclinical research in Alzheimer's disease–a focus on mode of action in pharmacological and non-pharmacological approaches". In: *European Neurological Review* 7.4 (2012), pp. 216–223.

[8] LW Chu et al. "Alzheimer's disease: early diagnosis and treatment". In: *Hong Kong Med J* 18.3 (2012), pp. 228–237.

[9] Susanne G Mueller et al. "Ways toward an early diagnosis in Alzheimer's disease: the Alzheimer's Disease Neuroimaging Initiative (ADNI)". In: *Alzheimer's & Dementia* 1.1 (2005), pp. 55–66.

[10] John Hornberger et al. "Clinical and cost implications of amyloid beta detection with amyloid beta positron emission tomography imaging in early Alzheimer's disease–the case of florbetapir". In: *Current medical research and opinion* 33.4 (2017), pp. 675–685.

[11] David Bissig et al. *The Relationship of Amyloid Beta in the Retina to that of the Brain is Burden-specific (P5. 1-024)*. 2019.

[12] Jennifer S Keppler and Peter S Conti. "A cost analysis of positron emission tomography". In: *American Journal of Roentgenology* 177.1 (2001), pp. 31–40.

[13] George W Torrance and David Feeny. "Utilities and quality-adjusted life years". In: *International journal of technology assessment in health care* 5.4 (1989), pp. 559–575.

[14] J Scott Sloka and Peter D Hollett. "Cost effectiveness of positron emission tomography in Canada." In: *Medical science monitor* 11.10 (2005), PH1–PH6.

[15] John Hardy. "The relationship between amyloid and tau". In: *Journal of Molecular Neuroscience* 20.2 (2003), pp. 203–206.

[16] Henry W Querfurth and Frank M LaFerla. "Mechanisms of disease". In: *N Engl J Med* 362.4 (2010), pp. 329–344.

[17] Elizabeth Drolle et al. "Atomic force microscopy to study molecular mechanisms of amyloid fibril formation and toxicity in Alzheimer's disease". In: *Drug metabolism reviews* 46.2 (2014), pp. 207–223.

[18] Moira E Bruce and H Fraser. "Amyloid plaques in the brains of mice infected with scrapie: morphological variation and staining properties". In: *Neuropathology and Applied Neurobiology* 1.2 (1975), pp. 189–202.

[19] Jay Rasmussen et al. "Amyloid polymorphisms constitute distinct clouds of conformational variants in different etiological subtypes of Alzheimer's disease". In: *Proceedings of the National Academy of Sciences* 114.49 (2017), pp. 13018–13023.

[20] Marcus Fändrich et al. "Amyloid fibril polymorphism: a challenge for molecular imaging and therapy". In: *Journal of internal medicine* 283.3 (2018), pp. 218–237.

[21] Sofie Nyström et al. "Evidence for age-dependent in vivo conformational rearrangement within Aβ amyloid deposits". In: *ACS chemical biology* 8.6 (2013), pp. 1128–1133.

[22] Karin Söderlund Leifler. "Chameleon molecules can see differences in plaque". In: (2017).

[23] Melanie Meyer-Luehmann et al. "Rapid appearance and local toxicity of amyloid-β plaques in a mouse model of Alzheimer's disease". In: *Nature* 451.7179 (2008), p. 720.

[24] Jasmin K Hefendehl et al. "Long-term in vivo imaging of β-amyloid plaque appearance and growth in a mouse model of cerebral β-amyloidosis". In: *Journal of Neuroscience* 31.2 (2011), pp. 624–629.

[25] Steffen Burgold et al. "In vivo imaging reveals sigmoidal growth kinetic of β-amyloid plaques". In: *Acta neuropathologica communications* 2.1 (2014), p. 30.

[26] Gregory J Zipfel et al. "Cerebral amyloid angiopathy: progressive disruption of the neurovascular unit". In: *Stroke* 40.3_suppl_1 (2009), S16–S19.

[27] Tracey C Dickson and James C Vickers. "The morphological phenotype of β-amyloid plaques and associated neuritic changes in Alzheimer's disease". In: *Neuroscience* 105.1 (2001), pp. 99–107.

[28] Michael R D'Andrea and Robert G Nagele. "Morphologically distinct types of amyloid plaques point the way to a better understanding of Alzheimer's disease pathogenesis". In: *Biotechnic & Histochemistry* 85.2 (2010), pp. 133–147.

[29] Alberto Serrano-Pozo et al. "Stable size distribution of amyloid plaques over the course of Alzheimer disease". In: *Journal of Neuropathology & Experimental Neurology* 71.8 (2012), pp. 694–701.

[30] Andrei G Vlassenko et al. "Amyloid-beta plaque growth in cognitively normal adults: Longitudinal [11C] Pittsburgh compound B data". In: *Annals of neurology* 70.5 (2011), pp. 857–861.

[31] Jorge Ghiso et al. "Cerebral amyloid angiopathy and Alzheimer's disease". In: *Hirosaki igaku= Hirosaki medical journal* 61.Suppl (2010), S111.

[32] Abby Keable et al. "Deposition of amyloid β in the walls of human leptomeningeal arteries in relation to perivascular drainage pathways in cerebral amyloid angiopathy". In: *Biochimica et Biophysica Acta (BBA)-Molecular Basis of Disease* 1862.5 (2016), pp. 1037–1046.

[33] SD Preston et al. "Capillary and arterial cerebral amyloid angiopathy in Alzheimer's disease: defining the perivascular route for the elimination of amyloid β from the human brain". In: *Neuropathology and applied neurobiology* 29.2 (2003), pp. 106–117.

[34] Daniel Pirici et al. "Fractal analysis of amyloid plaques in Alzheimer's disease patients and mouse models". In: *Neurobiology of aging* 32.9 (2011), pp. 1579–1587.

[35] Yosef Koronyo et al. “Retinal amyloid pathology and proof-of-concept imaging trial in Alzheimer’s disease”. In: *JCI insight* 2.16 (2017).

[36] Tao Jin et al. “Mapping the birefringence of amyloid deposits found in retinas in association with Alzheimer’s disease”. In: *Frontiers in Optics*. Optical Society of America. 2016, FTh5D–4.

[37] Melanie CW Campbell et al. “Polarization properties of amyloid beta in the retina of the eye as a biomarker of Alzheimer’s disease”. In: *Bio-Optics: Design and Application*. Optical Society of America. 2015, BM3A–4.

[38] Marius Kollmer et al. “Electron tomography reveals the fibril structure and lipid interactions in amyloid deposits”. In: *Proceedings of the National Academy of Sciences* 113.20 (2016), pp. 5604–5609.

[39] Honghui He et al. “A possible quantitative Mueller matrix transformation technique for anisotropic scattering media/Eine mögliche quantitative Müller-Matrix-Transformations-Technik für anisotrope streuende Medien”. In: *Photonics & Lasers in Medicine* 2.2 (2013), pp. 129–137.

[40] Rafael Espinosa-Luna and Eusebio Bernabeu. “On the Q (M) depolarization metric”. In: *Optics communications* 277.2 (2007), pp. 256–258.

[41] Jose Jorge Gil Perez and Razvigor Ossikovski. *Polarized light and the Mueller matrix approach*. CRC press, 2017.

[42] José Jorge Gil and Eusebio Bernabeu. “Depolarization and polarization indices of an optical system”. In: *Optica Acta: International Journal of Optics* 33.2 (1986), pp. 185–189.

[43] Shih-Yau Lu and Russell A Chipman. “Interpretation of Mueller matrices based on polar decomposition”. In: *JOSA A* 13.5 (1996), pp. 1106–1113.

[44] Nicole Rusk. “The fluorescence microscope”. In: *Nature Cell Biology* 11.1 (2009), S8–S9.

[45] Marvin Minsky. *Microscopy apparatus*. US Patent 3,013,467. 1961.

[46] Christoph Cremer and Thomas Cremer. “Considerations on a laser-scanning-microscope with high resolution and depth of field”. In: *Microscopica acta* (1974), pp. 31–44.

[47] WB Amos and JG White. “How the confocal laser scanning microscope entered biological research”. In: *Biology of the Cell* 95.6 (2003), pp. 335–342.

[48] Nadav J Hart et al. “Ocular indicators of Alzheimer’s: exploring disease in the retina”. In: *Acta neuropathologica* 132.6 (2016), pp. 767–787.

[49] Chiara La Morgia et al. “Melanopsin retinal ganglion cell loss in Alzheimer disease”. In: *Annals of neurology* 79.1 (2016), pp. 90–109.

[50] Carol Yim-lui Cheung et al. “Microvascular network alterations in the retina of patients with Alzheimer’s disease”. In: *Alzheimer’s & Dementia* 10.2 (2014), pp. 135–142.

[51] Lajos Csincsik et al. “Peripheral retinal imaging biomarkers for Alzheimer’s disease: a pilot study”. In: *Ophthalmic research* 59.4 (2018), pp. 182–192.

[52] Dilraj S Grewal et al. “Assessment of differences in retinal microvasculature using OCT angiography in Alzheimer’s disease: a twin discordance report”. In: *Ophthalmic Surgery, Lasers and Imaging Retina* 49.6 (2018), pp. 440–444.

[53] Melanie CW Campbell et al. “Amyloid as a biomarker of Alzheimer’s disease in post-mortem retinas in human and dog models of Alzheimer’s disease”. In: *Alzheimer’s & Dementia: The Journal of the Alzheimer’s Association* 12.7 (2016), pp. 319–320.

[54] Melanie CW Campbell et al. “The relationship between amyloid in the retina and a brain-based post-mortem diagnosis of Alzheimer’s Disease”. In: *Alzheimer’s & Dementia: The Journal of the Alzheimer’s Association* 13.7 (2017), pp. 284–285.

[55] Maya Koronyo-Hamaoui et al. “Identification of amyloid plaques in retinas from Alzheimer’s patients and noninvasive in vivo optical imaging of retinal plaques in a mouse model”. In: *Neuroimage* 54 (2011), S204–S217.

[56] Yuchun Tsai et al. “Ocular changes in TgF344-AD rat model of Alzheimer’s disease”. In: *Investigative ophthalmology & visual science* 55.1 (2014), pp. 523–534.

[57] Jurre den Haan et al. “Amyloid-beta and phosphorylated tau in post-mortem Alzheimer’s disease retinas”. In: *Acta neuropathologica communications* 6.1 (2018), p. 147.

[58] Christian Schön et al. “Long-term in vivo imaging of fibrillar tau in the retina of P301S transgenic mice”. In: *PLoS One* 7.12 (2012), e53547.

[59] Cheng-Ying Ho et al. “Beta-Amyloid, Phospho-Tau and Alpha-Synuclein Deposits Similar to Those in the Brain Are Not Identified in the Eyes of A lzheimer’s and P arkinson’s Disease Patients”. In: *Brain pathology* 24.1 (2014), pp. 25–32.

[60] Tao Jin. *Polarimetric and birefringence analysis of presumed amyloid-beta deposits in the retina in association with Alzheimer’s disease*. 2018. URL: http://hdl.handle.net/10012/13938.

[61] Masahito Yamada and Hironobu Naiki. “Cerebral amyloid angiopathy”. In: *Progress in molecular biology and translational science*. Vol. 107. Elsevier, 2012, pp. 41–78.

[62] Masahito Yamada. "Cerebral amyloid angiopathy: emerging concepts". In: *Journal of stroke* 17.1 (2015), p. 17.

[63] Johannes Attems. "Sporadic cerebral amyloid angiopathy: pathology, clinical implications, and possible pathomechanisms". In: *Acta neuropathologica* 110.4 (2005), pp. 345–359.

[64] Brandon James McIlmoyle et al. "Retinal amyloid beta load is associated with cerebral amyloid angiopathy." In: *Investigative Ophthalmology & Visual Science* 58.8 (2017), pp. 5127–5127.

[65] Thomas Liebmann et al. "Three-dimensional study of Alzheimer's disease hallmarks using the iDISCO clearing method". In: *Cell reports* 16.4 (2016), pp. 1138–1152.

[66] Bernhard Baumann et al. "Visualization of neuritic plaques in Alzheimer's disease by polarization-sensitive optical coherence microscopy". In: *Scientific reports* 7 (2017), p. 43477.

[67] Eric P Meyer et al. "Altered morphology and 3D architecture of brain vasculature in a mouse model for Alzheimer's disease". In: *Proceedings of the national academy of sciences* 105.9 (2008), pp. 3587–3592.

[68] Brian B Boycott, John E Dowling, and Helga Kolb. "Organization of the Primate Retina: Light Microscopy". In: *Philosophical Transactions of the Royal Society of London. Series B, Biological Sciences* (1969), pp. 109–184.

[69] Bradley T Hyman et al. "National Institute on Aging–Alzheimer's Association guidelines for the neuropathologic assessment of Alzheimer's disease". In: *Alzheimer's & dementia* 8.1 (2012), pp. 1–13.

[70] Sigma-Aldrich. *Fluoroshield™ with DAPI - Frequently Asked Questions*. 2019. URL: https://www.sigmaaldrich.com/catalog/product/sigma/f6057?lang=en&region=US (visited on 12/03/2019).

[71] Tyler A Kokjohn, Chera L Maarouf, and Alex E Roher. "Is Alzheimer's disease amyloidosis the result of a repair mechanism gone astray?" In: *Alzheimer's & Dementia* 8.6 (2012), pp. 574–583.

[72] David T Winkler et al. "Spontaneous hemorrhagic stroke in a mouse model of cerebral amyloid angiopathy". In: *Journal of Neuroscience* 21.5 (2001), pp. 1619–1627.

[73] YC Pao, JT Lu, and EL Ritman. "Bending and twisting of an in vivo coronary artery at a bifurcation". In: *Journal of biomechanics* 25.3 (1992), pp. 287–295.

[74] Hai-Chao Han. "Twisted Blood Vessels: Symptoms, Etiology and Biomechanical Mechanisms". In: *Journal of Vascular Research* 49 (2012), pp. 185–197.

[75] William R Brown and Clara R Thore. "Cerebral microvascular pathology in ageing and neurodegeneration". In: *Neuropathology and applied neurobiology* 37.1 (2011), pp. 56–74.

[76] Junichi Masuda et al. "Autopsy study of incidence and distribution of cerebral amyloid angiopathy in Hisayama, Japan." In: *Stroke* 19.2 (1988), pp. 205–210.

[77] Rita Carrotta et al. "Large size fibrillar bundles of the Alzheimer amyloid β-protein". In: *European Biophysics Journal* 36.7 (2007), pp. 701–709.

[78] Lauren M Wright et al. "Association of Cognitive Function with Amyloid-β and Tau Proteins in the Vitreous Humor". In: *Journal of Alzheimer's Disease* Preprint (2019), pp. 1–10.

[79] Thomas FitzGibbon and Simon F Taylor. "Mean retinal ganglion cell axon diameter varies with location in the human retina". In: *Japanese journal of ophthalmology* 56.6 (2012), pp. 631–637.

[80] Johannes Attems et al. "Sporadic cerebral amyloid angiopathy". In: *Neuropathology and applied neurobiology* 37.1 (2011), pp. 75–93.

[81] Janet L Wilterdink and J Donald Easton. "Vascular event rates in patients with atherosclerotic cerebrovascular disease". In: *Archives of neurology* 49.8 (1992), pp. 857–863.

[82] Jagdish Kakadiya. "Causes, symptoms, pathophysiology and diagnosis of atherosclerosis–a review". In: *PharmacologyOnline* 3 (2009), pp. 420–442.

[83] Delia Cabrera DeBuc, Gabor Mark Somfai, and Akos Koller. "Retinal microvascular network alterations: potential biomarkers of cerebrovascular and neural diseases". In: *American Journal of Physiology-Heart and Circulatory Physiology* 312.2 (2017), H201–H212.

[84] Seonghee Cho et al. "High-Contrast Imaging of Cholesterol Crystals in Rabbit Arteries Ex Vivo Using LED-Based Polarization Microscopy". In: *Sensors* 18.4 (2018), p. 1258.

[85] Pete A Williams et al. "Retinal ganglion cell dendritic degeneration in a mouse model of Alzheimer's disease". In: *Neurobiology of aging* 34.7 (2013), pp. 1799–1806.

[86] J Mario Isas et al. "Soluble and mature amyloid fibrils in drusen deposits". In: *Investigative ophthalmology & visual science* 51.3 (2010), pp. 1304–1310.

[87] Tzvete Dentchev et al. "Amyloid-β is found in drusen from some age-related macular degeneration retinas, but not in drusen from normal retinas". In: *American journal of ophthalmology* 136.4 (2003), pp. 787–787.

[88] Lincoln V Johnson et al. "Complement activation and inflammatory processes in Drusen formation and age related macular degeneration". In: *Experimental eye research* 73.6 (2001), pp. 887–896.

[89] Kresimir Ukalovic et al. "Drusen in the peripheral retina of the Alzheimer's eye". In: *Current Alzheimer Research* 15.8 (2018), pp. 743–750.

[90] Gordon J Smilnak et al. "Comorbidity of age-related macular degeneration with Alzheimer's disease: A histopathologic case-control study". In: *PloS one* 14.9 (2019).

[91] Ana Nunes et al. "Retinal texture biomarkers may help to discriminate between Alzheimer's, Parkinson's, and healthy controls". In: *PloS one* 14.6 (2019), e0218826.

[92] Benoit B Mandelbrot. "Stochastic models for the Earth's relief, the shape and the fractal dimension of the coastlines, and the number-area rule for islands". In: *Proceedings of the National Academy of Sciences* 72.10 (1975), pp. 3825–3828.

[93] Jian Li, Qian Du, and Caixin Sun. "An improved box-counting method for image fractal dimension estimation". In: *Pattern Recognition* 42.11 (2009), pp. 2460–2469.

[94] Renaud Lopes and Nacim Betrouni. "Fractal and multifractal analysis: a review". In: *Medical image analysis* 13.4 (2009), pp. 634–649.

[95] Eduardo Fernandez and Herbert F Jelinek. "Use of fractal theory in neuroscience: methods, advantages, and potential problems". In: *Methods* 24.4 (2001), pp. 309–321.

[96] Hadrien Salat, Roberto Murcio, and Elsa Arcaute. "Multifractal methodology". In: *Physica A: Statistical Mechanics and its Applications* 473 (2017), pp. 467–487.

[97] Wil OC Ward and Li Bai. "Multifractal analysis of microvasculature in health and disease". In: *2013 35th Annual International Conference of the IEEE Engineering in Medicine and Biology Society (EMBC)*. IEEE. 2013, pp. 2336–2339.

[98] Jacques Lévy-Véhel. *Introduction to the multifractal analysis of images*. 1998.

[99] Akihiko Kikuchi et al. "Multifractal description of the maternal surface of the placenta". In: *Gynecologic and obstetric investigation* 66.2 (2008), pp. 127–133.

[100] Branimir Reljin et al. "Breast cancer evaluation by fluorescent dot detection using combined mathematical morphology and multifractal techniques". In: *Diagnostic pathology*. Vol. 6. 1. BioMed Central. 2011, S21.

[101] Jacques Lévy-Véhel and Pierrick Legrand. "Signal and Image processing with FracLab". In: *Thinking in Patterns, World Scientific, Singapore* (2004), pp. 321–323.

[102] Jacques Lévy-Véhel and Robert Vojak. "Multifractal analysis of Choquet capacities". In: *Advances in applied mathematics* 20.1 (1998), pp. 1–43.

[103] Dierk Schleicher. "Hausdorff dimension, its properties, and its surprises". In: *The American Mathematical Monthly* 114.6 (2007), pp. 509–528.

[104] Timothy Collier. "Fractal Dimension-Measuring Complexity and Scaling". In: (2015).

[105] Christopher J Bishop and Yuval Peres. *Fractals in probability and analysis*. Vol. 162. Cambridge University Press, 2017.

[106] Jacques Lévy-Véhel and C Canus. "Hausdorff dimension estimation and application to multifractal spectrum computation". In: *INRIA, June* (1996).

[107] Tomislav Stojić, Irini Reljin, and Branimir Reljin. "Adaptation of multifractal analysis to segmentation of microcalcifications in digital mammograms". In: *Physica A: Statistical Mechanics and its Applications* 367 (2006), pp. 494–508.

[108] Jelena Andjelkovic et al. "Classifications of digital medical images with multifractal analysis". In: *Proc. 8th WSEAS Int. Conf. on Signal, Speech and Image Processing*. 2008, pp. 23–25.

[109] Edward Vrscay. *PMATH 370, Lecture 30: Measuring the sizes of fractal sets in R^k*.

[110] Alexandre Joel Chorin. "The evolution of a turbulent vortex". In: *Communications in Mathematical Physics* 83.4 (1982), pp. 517–535.

[111] Dawei Qi and Lei Yu. "Multifractal spectrum theory used to medical image from CT testing". In: *2008 IEEE/ASME International Conference on Advanced Intelligent Mechatronics*. IEEE. 2008, pp. 68–73.

[112] MATLAB. *version 9.6.0.1114505 (R2019a) Update 2*. Natick, Massachusetts: The MathWorks Inc., 2019.

[113] Rafael C. Gonzalez and Richard E. Woods. *Digital Image Processing*. 3rd ed. Pearson, 2007.

[114] Zhi-Cheng Ren et al. "Generalized poincaré sphere". In: *Optics express* 23.20 (2015), pp. 26586–26595.

[115] Erik Mason and Melanie CW Campbell. "Euclidean distance method for retinal amyloid polarimetry segmentation". In: *Investigative Ophthalmology & Visual Science* 60.9 (2019), pp. 179–179.

[116] Gang Xiong, Shuning Zhang, and Xiaoniu Yang. "The fractal energy measurement and the singularity energy spectrum analysis". In: *Physica A: Statistical Mechanics and its Applications* 391.24 (2012), pp. 6347–6361.

[117] SAS Institute. *Tests Based on the Empirical Distribution Function*. URL: https://support.sas.com/documentation/cdl/en/statug/63347/HTML/default/viewer.htm#statug_npar1way_a0000000202.htm (visited on 12/07/2019).

[118] Anupama Narayanan and Donna Watts. "Exact methods in the NPAR1WAY procedure". In: *Proceedings of the Twenty-First Annual SAS Users Group International Conference, Cary, NC: SAS Institute Inc.* 1996, pp. 1290–1294.

[119] Shaun Frost et al. "Alzheimer's disease and the early signs of age-related macular degeneration". In: *Current Alzheimer Research* 13.11 (2016), pp. 1259–1266.

[120] Leonardo Biscetti et al. "Associations of Alzheimer's disease with macular degeneration". In: *Front. Biosci.(Elite Ed.)* 9 (2017), pp. 174–191.

[121] Gopal Thinakaran and Edward H Koo. "Amyloid precursor protein trafficking, processing, and function". In: *Journal of Biological Chemistry* 283.44 (2008), pp. 29615–29619.

[122] Manuele Michelessi et al. "Optic nerve head and fibre layer imaging for diagnosing glaucoma". In: *Cochrane Database of Systematic Reviews* 11 (2015).

[123] Felipe A Medeiros et al. "Comparison of the GDx VCC Scanning Laser Polarimeter, HRT II ConfocalScanning Laser Ophthalmoscope, and Stratus OCT Optical Coherence Tomographfor the Detection of Glaucoma". In: *Archives of Ophthalmology* 122.6 (2004), pp. 827–837.

[124] Nandan Kumar Das et al. "Investigation of alterations in multifractality in optical coherence tomographic images of in vivo human retina". In: *Journal of Biomedical Optics* 21.9 (2016), p. 096004.

[125] Melanie CW Campbell et al. "Imaging of Amyloid-Beta Deposits in the Postmortem Retina in Alzheimer's Disease". In: *Investigative Ophthalmology & Visual Science* 51.13 (2010), pp. 5778–5778.

[126] Patricia A Boyle et al. "Cerebral amyloid angiopathy and cognitive outcomes in community-based older persons". In: *Neurology* 85.22 (2015), pp. 1930–1936.

[127] Christopher G Janson. "AD and CAA: Independent risk factors for dementia". In: *Science Translational Medicine* 7.318 (2015), 318ec214–318ec214.

[128] Vito Foderà et al. *Electrostatics controls the formation of amyloid-like superstructures in protein aggregation.*

[129] Kyoko Miyawaki et al. “Three-dimensional and fractal analyses of assemblies of amyloid β protein subtypes [Aβ40 and Aβ42 (43)] in canine senile plaques”. In: *Acta neuropathologica* 103.3 (2002), pp. 228–236.

[130] Suresh Balakrishnama and Aravind Ganapathiraju. “Linear discriminant analysis-a brief tutorial”. In: *Institute for Signal and information Processing* 18 (1998), pp. 1–8.

[131] Eleni Gkanatsiou et al. “A distinct brain beta amyloid signature in cerebral amyloid angiopathy compared to Alzheimer’s disease”. In: *Neuroscience letters* 701 (2019), pp. 125–131.

[132] Roy O Weller et al. “Cerebral amyloid angiopathy in the aetiology and immunotherapy of Alzheimer disease”. In: *Alzheimer’s research & therapy* 1.2 (2009), p. 6.

[133] Ludwig Reimer. *Transmission electron microscopy: physics of image formation and microanalysis*. Vol. 36. Springer, 2013.

[134] Peter D Nellist et al. “Direct sub-angstrom imaging of a crystal lattice”. In: *Science* 305.5691 (2004), pp. 1741–1741.

[135] Hidetaka Sawada et al. “Achieving 63 pm resolution in scanning transmission electron microscope with spherical aberration corrector”. In: *Japanese journal of applied physics* 46.6L (2007), p. L568.

[136] Hidetaka Sawada et al. “STEM imaging of 47-pm-separated atomic columns by a spherical aberration-corrected electron microscope with a 300-kV cold field emission gun”. In: *Journal of electron microscopy* 58.6 (2009), pp. 357–361.

[137] Ondrej L Krivanek et al. “Progress in ultrahigh energy resolution EELS”. In: *Ultramicroscopy* 203 (2019), pp. 60–67.

[138] Richard D Leapman, Michal Jarnik, and Alasdair C Steven. “Spatial distributions of sulfur-rich proteins in cornifying epithelia”. In: *Journal of structural biology* 120.2 (1997), pp. 168–179.

[139] Xiaoyue Wang et al. “Biomineralization at titanium revealed by correlative 4D tomographic and spectroscopic methods”. In: *Advanced Materials Interfaces* 5.14 (2018), p. 1800262.

Appendix A

Multifractal Analysis Considerations

A.1 Capacities

As mentioned in chapter 3, the choice of capacity is of the utmost importance for MFA. The capacity identifies the local property that will be evaluated in the regions of various sizes around each pixel in order to calculate the local regularity or Hölder exponent α, which are then used in calculating the global regularity or Hausdorff dimension F. That chapter focused on the *max* capacity as it seemed the most effective from preliminary comparisons of deposits associated with Alzheimer's disease (AD) brain pathologies versus those presumably related to age-related macular degeneration (AMD). The results in chapter 3 indicated that max-based MFA was able to differentiate between deposits associated with various pathologies, however it is possible that other comparisons of diagnostic interest will not be well differentiated by this method, in which case consideration could be given to other metrics that highlight more pertinent textural differences. The *iso* capacity is another approach towards characterizing the local regularity of the image. Whereas *max* represents the dependence of the maximum value in a vicinity around a pixel as a function of the size of said vicinity, *iso* is similar to a measure of the uniqueness of values within those vicinities. To measure *iso* the following equation can be used:

$$\mu_{iso}(x, y) = \#[I(x, y) == Mo(I(x, y))] \tag{A.1}$$

where x,y denote the horizontal and vertical range of values being considered, each with length ϵ of course, # denotes a count or cardinal, and Mo is the mode. In plain language, *iso* represents the number of values in a region of size ϵ, centered at x, y in image I that are the most frequent members of the region. As the authors of FracLab [101] indicate,

μ_{iso} in a region without repeated gray levels is 1 as 1 is the greatest number of occurrences of a particular value in the region, whereas a region that is all a single value, or flat in a sense, will have μ_{iso} equal to the number of pixels in the region (i.e. ϵ^2). One important comment on the use of *iso* which may have hindered its success in early tests is that the uniqueness of R_L values is widespread in most of the R_L maps, due to the high decimal precision used in our calculations. To achieve a meaningful distinction between textural features of deposits associated with different pathological groups, further tests should begin by considering lower decimal precision in R_L values.

A.2 Note on Image Boundaries for MFA

There are minor issues that arise from the exclusion of pixels near the border of an image when calculating the Hölder exponent map. Avoiding the pixels closest to the boundary creates a dark frame around the field, with the excluded pixels receiving Hölder exponents of zero, and corresponds to F values slightly larger than that of a straight line (1.212 in figure 3.2).

The portion of the MFS related to the dark frame has no physical information about the sample. Removal of the dark frames could be performed by cropping the Hölder exponent map on all sides by $\frac{Hvec_{max}}{2}$ rounded down. This is because a box of width $Hvec_{max}$ centered at a pixel less than $\frac{Hvec_{max}}{2}$ rounded down from the image boundary would include a region outside of the image. Below in figure A.1 is an example of a MFS that has been calculated from a Hölder exponent map that included the dark frame, and another that was cropped to remove it. The version on the right in figure A.1a which excludes the dark frame has a more prominent first peak (which can be noted by its lower value of $F(\alpha = 0)$), and is otherwise very similar to the spectrum that was calculated without cropping away the dark frame.

As the size of $Hvec_{max}$ is increased relative to the number of pixels in the image, the differences in the first peak become more pronounced, with the apparent reason being that the Hausdorff dimension associated with the dark frame becomes larger and creates an inflection between the $\alpha = 0$ intercept and the first peak in the MFS (figure A.1b). Conversely, excluding the dark frame in such an image seems to again make the first peak more prominent.

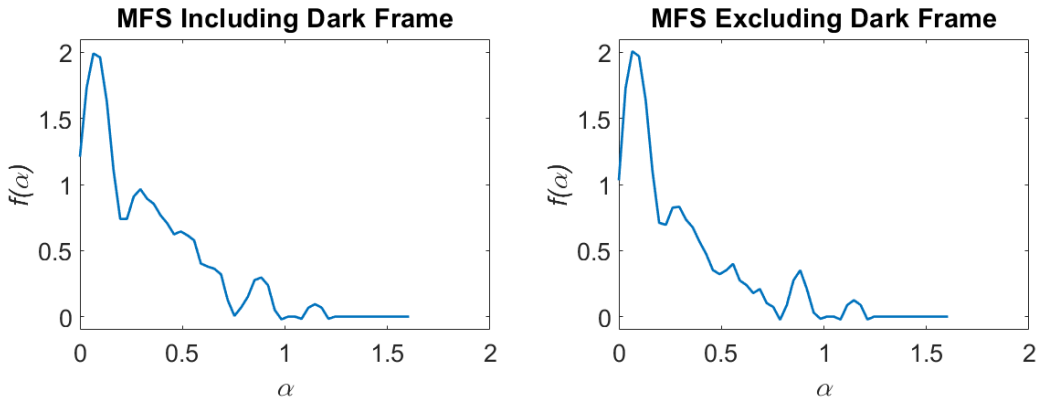

(a) MFSs for the original R_L map image dimensions.

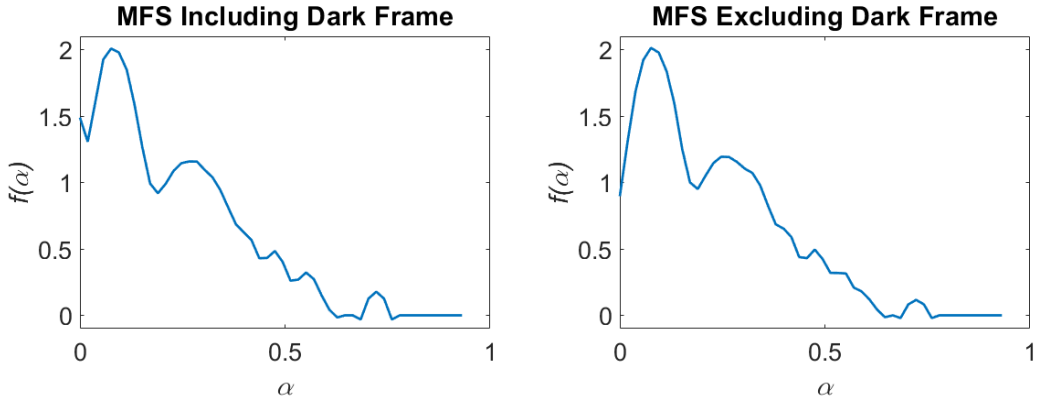

(b) MFSs for the R_L map that was shrunk by a factor of 4 prior to Hölder exponent calculation.

Figure A.1: Smoother MFSs that have been calculated with and without including the dark frame that is created in the Hölder exponent map.

A.3 Segmentation

Future applications of MFA for differentiating between retinal amyloid deposits may include comparisons between MFSs of fields that do and do not contain deposits. Analysis of the background retina in such cases could possibly indicate if textural differences near deposits are related to particular pathological changes. To identify deposit-based contributions to the MFS, the segmentation method by Mason [115] was initially considered. This segmentation method works perfectly from most considerations, but is designed in such a manner that it does not maintain the texture of the boundary between deposits and retinal surround. A version of the segmentation (also by Mason [115]) which typically slightly overestimates the size of the deposit (as compared to the human visual system) could possibly be applied to the Hölder exponent maps before F calculation, but in many of the anterior deposits with poorly defined boundaries, it is a highly subjective assessment as to whether the entire deposit is truly within the mask. Primarily for these reasons, unsegmented linear retardance maps were analyzed in the MFA described in chapter 3. However, other refinements could feasibly be made to the segmentation method for this particular application, that would likely slow the segmentation but result in more accurate preservation of the boundary between the deposits and retinal surround. One such modification could involve an active contour segmentation with the overestimated mask as a starting point for the segmentation.

A.4 Rotation Tests

Sensitivity of MFA of deposits to rotation of the scanning module about the z-axis was tested using six z-stacks of a single deposit imaged with different orientations. The z-stacks were then projected into the *en face* plane by summing along the z-direction (figure A.2). A segmentation was performed by thresholding each projected stack at 2000 (a.u.), to calculate the orientation of the deposit. The `regionprops` function in Matlab was then used to calculate the orientation of the segmented region. Orientation of the first z-stack was set to 0^o as a reference. MFSs were calculated for each projection, with $Hvec$: 1:2:17, $Svec_{min}$ 1, and the *max* capacity. An 8th order polynomial $p_8(\alpha)$ was fitted to each smoothed MFS[1] in Matlab. The polynomial fitting process also determined standard error values for each point in each fitted polynomial. For each of the 50 interpolated α chosen, the upper bound on the 95 % confidence interval CI_U was taken as the lowest value of the

[1]Recall that all of the MFSs are locally filtered using a Savitzky-Golay method

sum of the polynomial plus twice the calculated standard error δ at that point[2], and the converse is true of the lower bound on the 95 % confidence interval[2] CI_L (see equation A.3).

$$CI_U(\alpha) = min[p_8^i(\alpha) + 2\delta^i] \tag{A.2}$$

$$CI_L(\alpha) = max[p_8^i(\alpha) - 2\delta^i] \tag{A.3}$$

where $p_8^i(\alpha)$ represents the eighth order polynomial fit of the i^{th} z-stack evaluated at Hölder exponent α, and δ^i is the standard error on the evaluation of $p_8^i(\alpha)$, with $2\delta^i$ being a range from p_8^i at α that should enclose roughly 95 % of the predicted measurements. Comparison of the fitted polynomials, CI_U and CI_L, should reveal whether the polynomial fits are mutually consistent for any particular values or ranges of α. The spectra are nearly coincident at $\alpha = 0.03$. Figure A.3 illustrates the consistency between the MFSs of the differently oriented z-stacks. Trends in the figure are based on 8^{th} order polynomial fits to each of the smoothed (Savitzky-Golay) MFSs. In Matlab, the polynomial fitting process can calculate standard error δ for each point the polynomial is fitted to. In figure A.3, for each of the 50 interpolated α chosen, the upper bound on 95 % confidence interval was taken as the lowest value of the sum of the polynomial plus twice the calculated δ at that point (see equation A.3). The polynomial fitted MFSs of the rotated z-stacks are not significantly different for small to medium α. Most of the points that spread beyond the 95 % confidence interval are still near the boundary until the high-α end of the spectra. Note that in figure A.3 the upper and lower bounds cross at approximately α=0.25. This indicates a non-physical possibility and hence represents a region in the spectra in which modelling the similarity of the polynomial fits arguably failed.

Normally, the extent of the confidence interval is symmetric about a point (i.e. $x \pm \sigma_x$) and the interval bounds never cross. Interpretation of this unusual non-physical effect might lead to the judgment that none of the values in this range are consistent (all points are either above the upper bound or below the lower bound). This suggests that some sharper features in the z-stacks vary between the rotated fields. This point towards metrics involving the overall shape of the spectra (which is highly consistent) and those that are not influenced strongly by the Hausdorff dimensions near the end of the spectra.

To investigate this, the possibility that the end of the spectrum is not heavily influenced by large scale features in the z-stacks, but rather by noise and anomalies in the field, was tested. The process used in generating the plot in figure A.3 was repeated for the deposits only (see figure A.4). The background signals were removed from the projections to check if the inconsistency in the high α regime was indicative of differences in the regions

[2]Across all of the polynomial

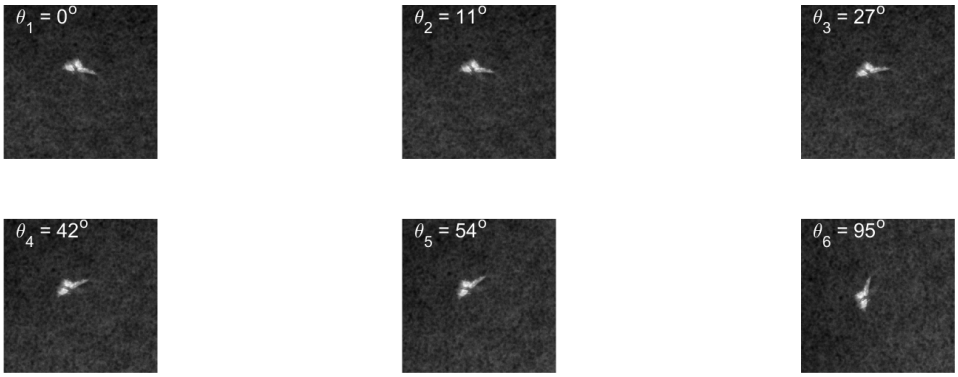

Figure A.2: Rotated versions of the same deposit, shown as a summed projection along the z (or *en face*) direction. Angles shown are defined relative to the overall orientation of the first stack (upper left).

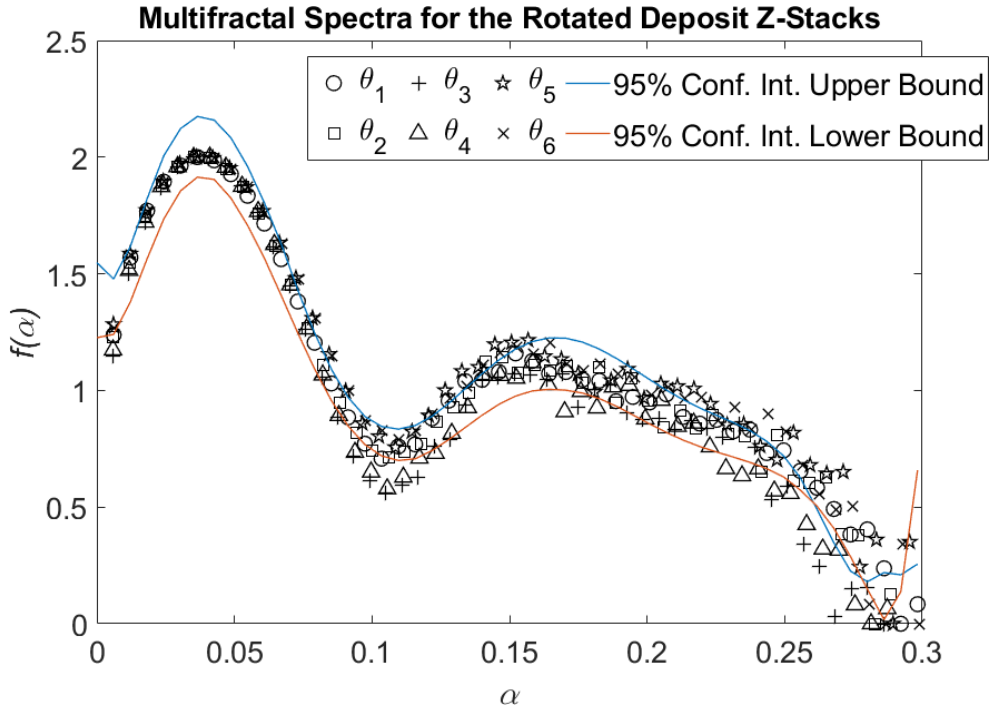

Figure A.3: MFSs for six different orientations of the same deposit with labelled confidence interval and polynomial fits. The solid lines represent conservative bounds on the 95% confidence interval. The data markers represent fitted curves based on the raw data (without smoothing).

associated with the deposits. This was accomplished by applying the mask that was used in determining deposit orientation to the Hölder exponent map before binning the α values and calculating the Hausdorff dimensions. Again, MFSs were calculated, but this time they were not smoothed, and then 8^{th} order polynomials were again fitted to the MFSs. Another difference between the calculation processes was that the α=0 coordinate was ignored as it was related solely to the background and thus was of no relevance.

The resultant MFSs with confidence interval bounds based on the polynomial fits are shown in figure A.4. From these MFSs, it seems that the deposit related spectra are almost entirely within the 95% confidence interval, suggesting that the spectra for the deposits are not significantly different from the range of the fitted polynomial curves. Previous reports have suggested that MFA is insensitive to translation and scale [98]. These tests suggest that MFSs of retinal amyloid deposits are fairly insensitive to rotation, including portions of the spectra linked to the deposits.

A.5 Polarization Metrics

Additional polarization metric maps from chapter 3 are shown in figures A.5 and A.6.

A.6 Magnification Tests (Additional Data)

See figure A.7 for an additional comparison of R_L maps that were resampled, and their corresponding MFSs. Also, figure A.9 displays the MFSs associated with R_L maps, based on the same set of 4X images, which have been resampled using three different methods available in Matlab. For α <0.35 in figure A.9, the spectra are similar, with slightly different peak widths. As α increases past 0.35 the differences between the spectra become severe, with a prominent peak near the end of the spectrum for the bicubically-resized R_L map. The bilinear and bicubic methods can include values outside the range of the original image in the resized result, taking away from the physical accuracy of the R_L map, and also affecting the MFS.

A.7 Proof of Equation 3.6

In chapter 3, some tests were performed to compare deposit R_L maps based on images taken with various magnifications. Equation 3.6 was used to determine the region within

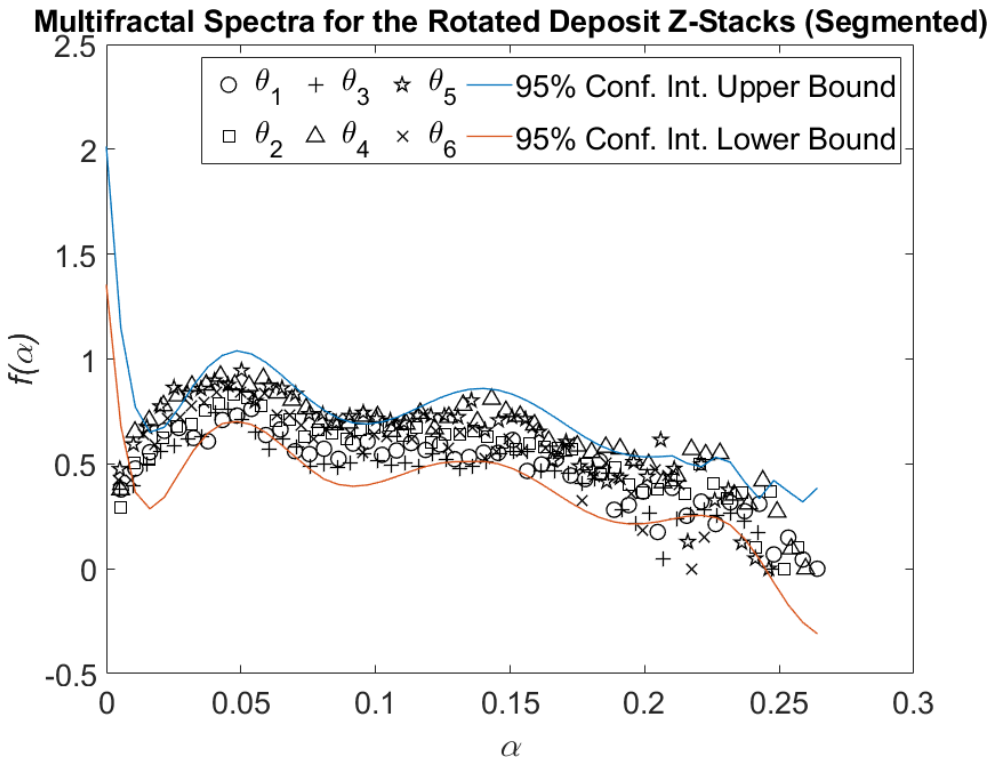

Figure A.4: MFSs for projections of six rotated z-stacks of the same deposit, with backgrounds removed through segmentation. The solid lines represent conservative bounds on the 95% confidence interval. The data markers represent the calculated MFSs without smoothing.

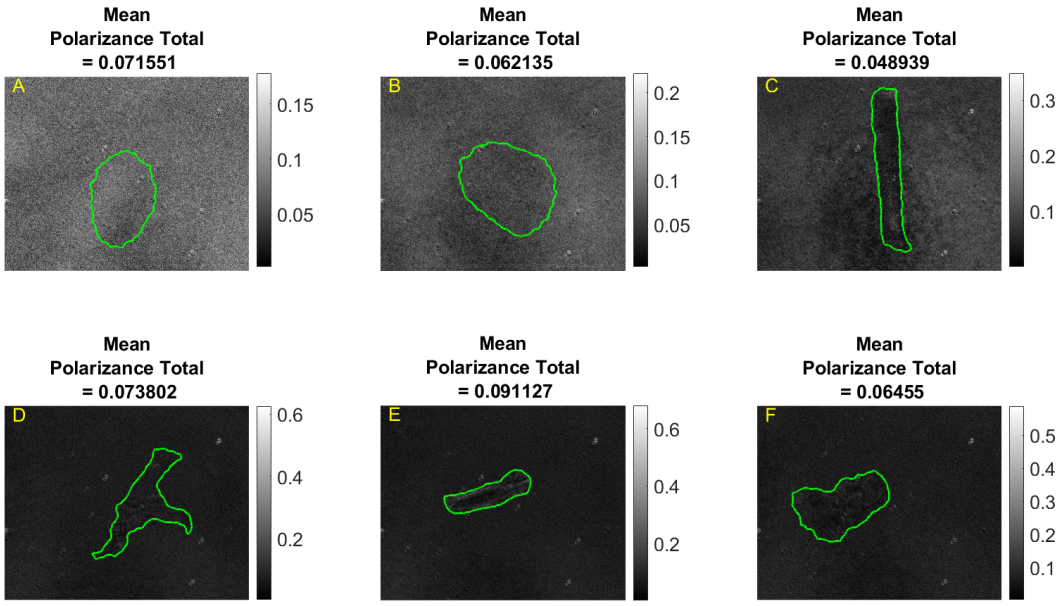

Figure A.5: Total polarizance maps for six deposits in anterior layers of retinal tissue samples from subjects with intermediate severity of AD.

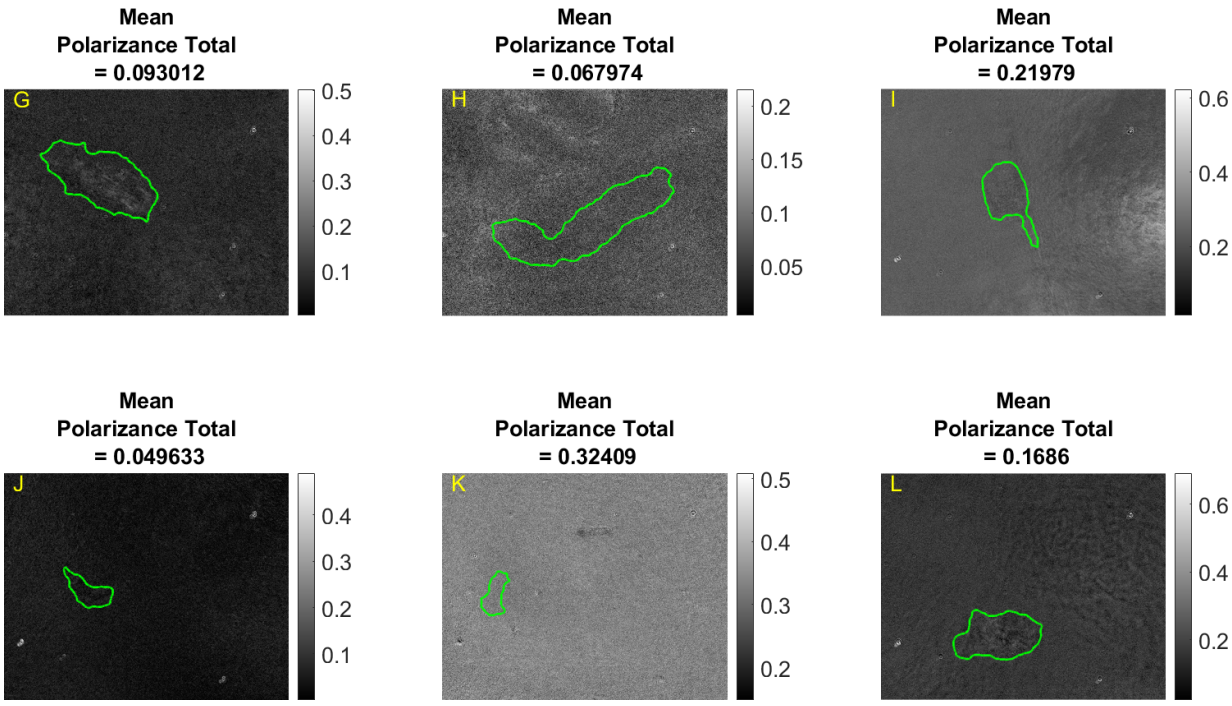

Figure A.6: Total polarizance P_T maps for six deposits in anterior layers of retinal tissue samples from subjects with high severity of AD. Note that the P_T mean deposit values are significantly different between intermediate and high severity of AD brain pathology but there is overlap.

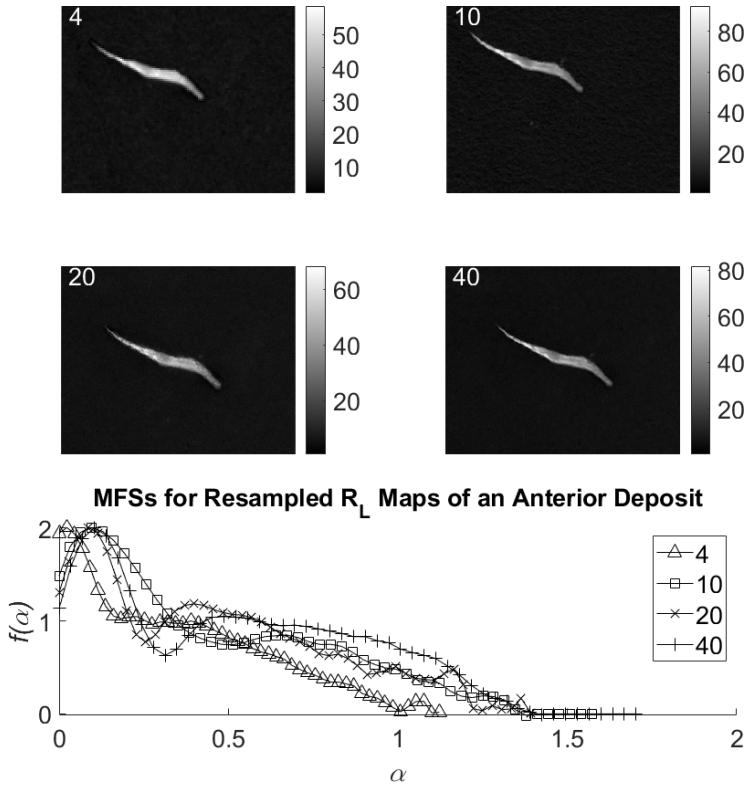

Figure A.7: R_L maps calculated from Mueller matrices based on images taken with different magnifications (see figure labels), and the corresponding MFSs indicating the impact of the scaling factor. The factors shown are those by which the R_L maps were shrunk before being enlarged by the reciprocal factor. The spectra were calculated using Hvec: 1:2:17, $Svec_{min}$: 1, capacity: *max*

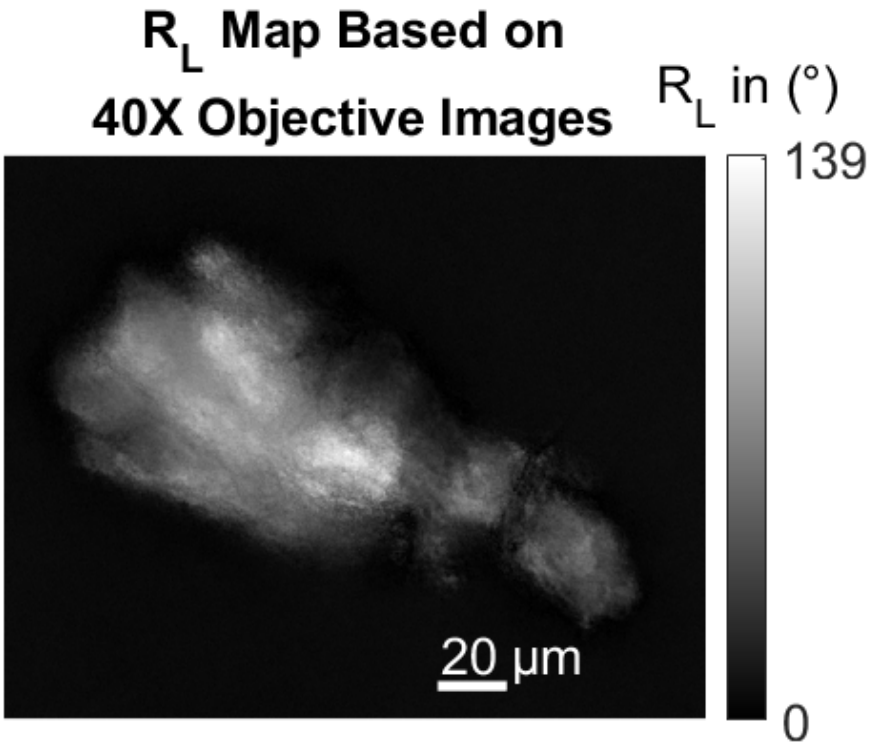

Figure A.8: R_L map based on images taken with a 40X objective for comparison with the resized R_L maps that are based on images taken with a 4X objective in figure A.9.

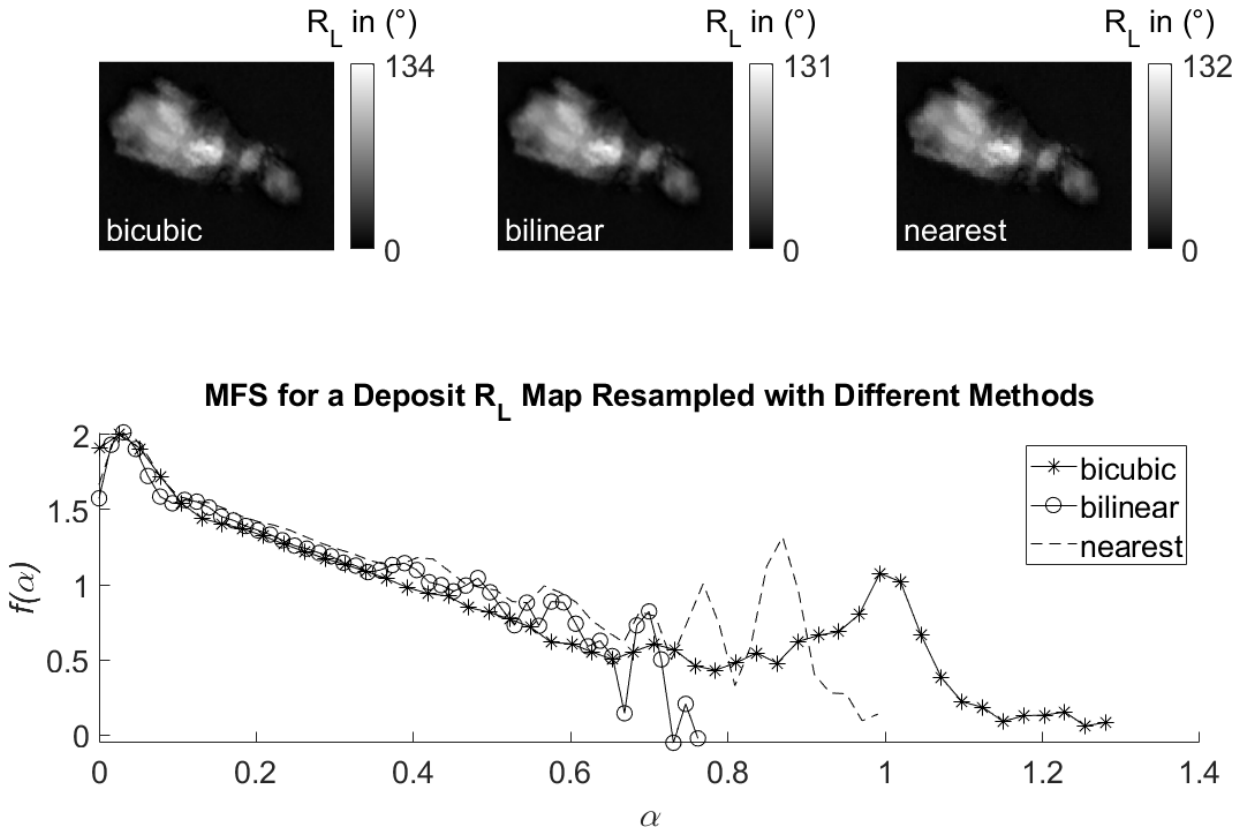

Figure A.9: R_L maps calculated from Mueller matrices based on images taken with a 4X objective and up-sampled to spatially match a 40X objective, with three different methods for performing the resizing operation. The resizing is an interpolation that is used to ensure that the R_L maps taken with different magnifications result in images associated with the same spatial region in the sample, with the same total number of pixels (which is important for the MFS calculation since the region sizes used in each step are defined in numbers of pixels). Corresponding MFSs are also presented. The spectra were calculated using Hvec: 1:2:17, $Svec_{min}$: 1, capacity: max

maps taken with objectives with 20X, 10X, or 4X magnification that corresponded to the same space encompassed by the 40X magnification. Lower magnification R_L maps cover a larger spatial region in the same number of pixels, hence fewer pixels are actually associated with the deposit. To derive equation 3.6, consider an image with dimensions x^O by y^O taken with objective O, which fully encloses a field imaged with another objective O', and allow the magnifications associated with O and O' to be M^O and $M^{O'}$, respectively. The ratio in the dimensions of the two images is the inverse of the ratio of the magnifications. Hence:

$$x^O = x^{O'} \frac{M^{O'}}{M^O}, \tag{A.4}$$

or equivalently:

$$x^{O'} = x^O \frac{M^O}{M^{O'}} \tag{A.5}$$

If the images taken with both objectives have identical centers (i.e. concentric rectangles), then the region of the image I^O taken with O that fully matches the region in image $I^{O'}$ taken with O' has horizontal boundaries given by: $x^O_{crop} = \left\lfloor \frac{x^O \pm x^{O'}}{2} \right\rfloor$, or equivalently:

$$x^O_{crop} = \left\lfloor \frac{x^O \pm x^O \frac{M^O}{M^{O'}}}{2} \right\rfloor \tag{A.6}$$

Then, by factoring out common terms:

$$x^O_{crop} = \frac{x^O}{2}(1 \pm \frac{M^O}{M^{O'}}) \tag{A.7}$$

Since this thesis is concerned with practical experimentation, it is necessary to ensure that the positions of the image endpoints in a particular dimension are integer values. For this purpose, the flooring operation $\lfloor\rfloor$ is used to round all values down to the nearest integer (though one could reasonably argue that simply rounding in either direction to the absolute nearest integer would be appropriate). For the relevant experiments described in chapter 3, R_L maps were resized to ensure that each of the lower objective-based maps had the same number of pixels associated with the deposit. Due to slight differences in lateral positions of the field, translations were performed to align the images after they were resized (interpolated), and then each was cropped so as to match the spatial region captured using $M^{O'}$=40. With that taken into consideration, the final formula representing the bounds of the cropped the R_L maps is:

$$x^O_{crop} = x^O \left\lfloor \frac{1}{2}(1 \pm \frac{M^O}{40}) \right\rfloor \tag{A.8}$$

with the equivalent expression holding for the cropping in the vertical direction.

Appendix B

Comments on Morphological Analysis of Amyloid in the Retina

B.1 Periodic Structural Elements

There are deposits that appear to have periodic segments that could be ordered bundles of fibrillar amyloid (figure B.1). These segments have been seen near the edges of deposits. This might be due to the fact that the edges of large deposits are often thinner than the bulk of the deposit and thus there is less "bleed-through" of fluorescence from other planes, making resolving individual fibrillar bundles less difficult.

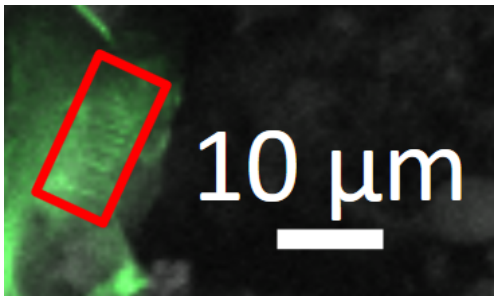

(a)

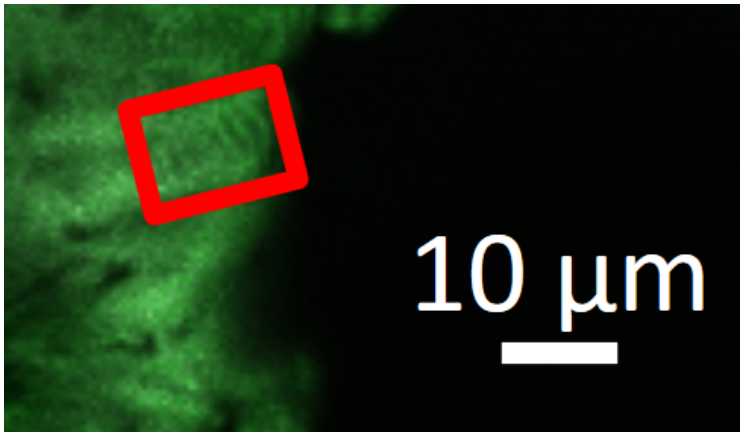

(b)

Figure B.1: Subsections from deposits that appear to display periodically arranged fibrillar bundles of amyloid. Note that B.1a was imaged by **MK**.

Appendix C

Permission Statements

Peter Andrew Charles Neathway

From: Sofie Nyström <sofie.nystrom@liu.se>
Sent: Friday, October 25, 2019 4:37 AM
To: Peter Andrew Charles Neathway
Cc: Peter Nilsson; Per Hammarström
Subject: RE: Amyloid Polymorphism Images
Attachments: APP23 vasc SNqFhF_01-17_010711082740.tif

Hi Peter,
Please find attached the image in high res. Cite Nyström ACS Chem biol 2013 and write image courtesy Sofie Nyström in the figure legend as citation (so no one expects to find this particular image in that paper). And make sure the image doesn't end up somewhere else. Or is copy righted.

Best
Sofie

From: Peter Andrew Charles Neathway <peter.neathway@uwaterloo.ca>
Sent: den 24 oktober 2019 16:58
To: Sofie Nyström <sofie.nystrom@liu.se>
Cc: Peter Nilsson <peter.r.nilsson@liu.se>; Per Hammarström <per.hammarstrom@liu.se>
Subject: Re: Amyloid Polymorphism Images

Hi Sofie,

Thank you for clarifying that! I have included citations to the papers you mentioned in my thesis, and I am hoping to include one of the images from the article for discussion. In particular, the image that I have screen-captured and copy below, is one I would like to include. Is there any chance at all that you still have a digital copy of this image so that I can include it at its proper resolution? If not I can use the screen-captured version, but I wanted to check with you first.

Thanks again! ☺

Figure C.1: Permission for inclusion of figure 1.1, p1

The Royal Society (U.K.) - License Terms and Conditions

Order Date	15-Jan-2020
Order license ID	1013787-1
ISSN	2054-0280
Type of Use	Republish in a thesis/dissertation
Publisher	The Society
Portion	Image/photo/illustration

LICENSED CONTENT

Publication Title	Philosophical transactions of the Royal Society of London. Series B, Biological sciences	Country	United Kingdom of Great Britain and Northern Ireland
Author/Editor	Royal Society (Great Britain)	Rightsholder	The Royal Society (U.K.)
Date	01/01/1934	Publication Type	e-Journal
Language	English	URL	https://royalsociety.org/journals/

REQUEST DETAILS

Portion Type	Image/photo/illustration	Distribution	Worldwide
Number of images / photos / illustrations	1	Translation	Original language of publication
Format (select all that apply)	Print, Electronic	Copies for the disabled?	No
		Minor editing privileges?	No
Who will republish the content?	Academic institution	Incidental promotional use?	No
Duration of Use	Life of current and all future editions	Currency	CAD
Lifetime Unit Quantity	Up to 999		
Rights Requested	Main product		

NEW WORK DETAILS

Title	Morphological and Multifractal Analyses of Retinal Amyloid Deposits for Staging in Alzheimer's Disease	Institution name	University of Waterloo
		Expected presentation date	2020-01-24
Instructor name	Melanie CW Campbell		

ADDITIONAL DETAILS

Order reference number	N/A	The requesting person / organization to appear on the license	Peter Neathway

Figure C.2: Permission for inclusion of figure 2.1, p1

REUSE CONTENT DETAILS

Title, description or numeric reference of the portion(s)	Vertical section through a human retina	**Title of the article/chapter the portion is from**	Organization of the Primate Retina: Light Microscopy
Editor of portion(s)	N/A	**Author of portion(s)**	Royal Society (Great Britain)
Volume of serial or monograph	255	**Issue, if republishing an article from a serial**	799
Page or page range of portion	116	**Publication date of portion**	1969-03-27

PUBLISHER TERMS AND CONDITIONS

Out of Copyright - any journal requested with a Publication date older than 70 years.

CCC Republication Terms and Conditions

1. Description of Service; Defined Terms. This Republication License enables the User to obtain licenses for republication of one or more copyrighted works as described in detail on the relevant Order Confirmation (the "Work(s)"). Copyright Clearance Center, Inc. ("CCC") grants licenses through the Service on behalf of the rightsholder identified on the Order Confirmation (the "Rightsholder"). "Republication", as used herein, generally means the inclusion of a Work, in whole or in part, in a new work or works, also as described on the Order Confirmation. "User", as used herein, means the person or entity making such republication.

2. The terms set forth in the relevant Order Confirmation, and any terms set by the Rightsholder with respect to a particular Work, govern the terms of use of Works in connection with the Service. By using the Service, the person transacting for a republication license on behalf of the User represents and warrants that he/she/it (a) has been duly authorized by the User to accept, and hereby does accept, all such terms and conditions on behalf of User, and (b) shall inform User of all such terms and conditions. In the event such person is a "freelancer" or other third party independent of User and CCC, such party shall be deemed jointly a "User" for purposes of these terms and conditions. In any event, User shall be deemed to have accepted and agreed to all such terms and conditions if User republishes the Work in any fashion.

3. Scope of License; Limitations and Obligations.

   3.1. All Works and all rights therein, including copyright rights, remain the sole and exclusive property of the Rightsholder. The license created by the exchange of an Order Confirmation (and/or any invoice) and payment by User of the full amount set forth on that document includes only those rights expressly set forth in the Order Confirmation and in these terms and conditions, and conveys no other rights in the Work(s) to User. All rights not expressly granted are hereby reserved.

   3.2. General Payment Terms: You may pay by credit card or through an account with us payable at the end of the month. If you and we agree that you may establish a standing account with CCC, then the following terms apply: Remit Payment to: Copyright Clearance Center, 29118 Network Place, Chicago, IL 60673-1291. Payments Due: Invoices are payable upon their delivery to you (or upon our notice to you that they are available to you for downloading). After 30 days, outstanding amounts will be subject to a service charge of 1-1/2% per month or, if less, the maximum rate allowed by applicable law. Unless otherwise specifically set forth in the Order Confirmation or in a separate written agreement signed by CCC, invoices are due and payable on "net 30" terms. While User may exercise the rights licensed immediately upon issuance of the Order Confirmation, the license is automatically revoked and is null and void, as if it had never been issued, if complete payment for the license is not received on a timely basis either from User directly or through a payment agent, such as a credit card company.

   3.3. Unless otherwise provided in the Order Confirmation, any grant of rights to User (i) is "one-time" (including the editions and product family specified in the license), (ii) is non-exclusive and non-transferable and (iii)

Figure C.3: Permission for inclusion of figure 2.1, p2

is subject to any and all limitations and restrictions (such as, but not limited to, limitations on duration of use or circulation) included in the Order Confirmation or invoice and/or in these terms and conditions. Upon completion of the licensed use, User shall either secure a new permission for further use of the Work(s) or immediately cease any new use of the Work(s) and shall render inaccessible (such as by deleting or by removing or severing links or other locators) any further copies of the Work (except for copies printed on paper in accordance with this license and still in User's stock at the end of such period).

3.4. In the event that the material for which a republication license is sought includes third party materials (such as photographs, illustrations, graphs, inserts and similar materials) which are identified in such material as having been used by permission, User is responsible for identifying, and seeking separate licenses (under this Service or otherwise) for, any of such third party materials; without a separate license, such third party materials may not be used.

3.5. Use of proper copyright notice for a Work is required as a condition of any license granted under the Service. Unless otherwise provided in the Order Confirmation, a proper copyright notice will read substantially as follows: "Republished with permission of [Rightsholder's name], from [Work's title, author, volume, edition number and year of copyright]; permission conveyed through Copyright Clearance Center, Inc. " Such notice must be provided in a reasonably legible font size and must be placed either immediately adjacent to the Work as used (for example, as part of a by-line or footnote but not as a separate electronic link) or in the place where substantially all other credits or notices for the new work containing the republished Work are located. Failure to include the required notice results in loss to the Rightsholder and CCC, and the User shall be liable to pay liquidated damages for each such failure equal to twice the use fee specified in the Order Confirmation, in addition to the use fee itself and any other fees and charges specified.

3.6. User may only make alterations to the Work if and as expressly set forth in the Order Confirmation. No Work may be used in any way that is defamatory, violates the rights of third parties (including such third parties' rights of copyright, privacy, publicity, or other tangible or intangible property), or is otherwise illegal, sexually explicit or obscene. In addition, User may not conjoin a Work with any other material that may result in damage to the reputation of the Rightsholder. User agrees to inform CCC if it becomes aware of any infringement of any rights in a Work and to cooperate with any reasonable request of CCC or the Rightsholder in connection therewith.

4. Indemnity. User hereby indemnifies and agrees to defend the Rightsholder and CCC, and their respective employees and directors, against all claims, liability, damages, costs and expenses, including legal fees and expenses, arising out of any use of a Work beyond the scope of the rights granted herein, or any use of a Work which has been altered in any unauthorized way by User, including claims of defamation or infringement of rights of copyright, publicity, privacy or other tangible or intangible property.

5. Limitation of Liability. UNDER NO CIRCUMSTANCES WILL CCC OR THE RIGHTSHOLDER BE LIABLE FOR ANY DIRECT, INDIRECT, CONSEQUENTIAL OR INCIDENTAL DAMAGES (INCLUDING WITHOUT LIMITATION DAMAGES FOR LOSS OF BUSINESS PROFITS OR INFORMATION, OR FOR BUSINESS INTERRUPTION) ARISING OUT OF THE USE OR INABILITY TO USE A WORK, EVEN IF ONE OF THEM HAS BEEN ADVISED OF THE POSSIBILITY OF SUCH DAMAGES. In any event, the total liability of the Rightsholder and CCC (including their respective employees and directors) shall not exceed the total amount actually paid by User for this license. User assumes full liability for the actions and omissions of its principals, employees, agents, affiliates, successors and assigns.

6. Limited Warranties. THE WORK(S) AND RIGHT(S) ARE PROVIDED "AS IS". CCC HAS THE RIGHT TO GRANT TO USER THE RIGHTS GRANTED IN THE ORDER CONFIRMATION DOCUMENT. CCC AND THE RIGHTSHOLDER DISCLAIM ALL OTHER WARRANTIES RELATING TO THE WORK(S) AND RIGHT(S), EITHER EXPRESS OR IMPLIED, INCLUDING WITHOUT LIMITATION IMPLIED WARRANTIES OF MERCHANTABILITY OR FITNESS FOR A PARTICULAR PURPOSE. ADDITIONAL RIGHTS MAY BE REQUIRED TO USE ILLUSTRATIONS, GRAPHS, PHOTOGRAPHS, ABSTRACTS, INSERTS OR OTHER PORTIONS OF THE WORK (AS OPPOSED TO THE ENTIRE WORK) IN A MANNER CONTEMPLATED BY USER; USER UNDERSTANDS AND AGREES THAT NEITHER CCC NOR THE RIGHTSHOLDER MAY HAVE SUCH ADDITIONAL RIGHTS TO GRANT.

Figure C.4: Permission for inclusion of figure 2.1, p3

7. Effect of Breach. Any failure by User to pay any amount when due, or any use by User of a Work beyond the scope of the license set forth in the Order Confirmation and/or these terms and conditions, shall be a material breach of the license created by the Order Confirmation and these terms and conditions. Any breach not cured within 30 days of written notice thereof shall result in immediate termination of such license without further notice. Any unauthorized (but licensable) use of a Work that is terminated immediately upon notice thereof may be liquidated by payment of the Rightsholder's ordinary license price therefor; any unauthorized (and unlicensable) use that is not terminated immediately for any reason (including, for example, because materials containing the Work cannot reasonably be recalled) will be subject to all remedies available at law or in equity, but in no event to a payment of less than three times the Rightsholder's ordinary license price for the most closely analogous licensable use plus Rightsholder's and/or CCC's costs and expenses incurred in collecting such payment.

8. Miscellaneous.

   8.1. User acknowledges that CCC may, from time to time, make changes or additions to the Service or to these terms and conditions, and CCC reserves the right to send notice to the User by electronic mail or otherwise for the purposes of notifying User of such changes or additions; provided that any such changes or additions shall not apply to permissions already secured and paid for.

   8.2. Use of User-related information collected through the Service is governed by CCC's privacy policy, available online here: https://marketplace.copyright.com/rs-ui-web/mp/privacy-policy

   8.3. The licensing transaction described in the Order Confirmation is personal to User. Therefore, User may not assign or transfer to any other person (whether a natural person or an organization of any kind) the license created by the Order Confirmation and these terms and conditions or any rights granted hereunder; provided, however, that User may assign such license in its entirety on written notice to CCC in the event of a transfer of all or substantially all of User's rights in the new material which includes the Work(s) licensed under this Service.

   8.4. No amendment or waiver of any terms is binding unless set forth in writing and signed by the parties. The Rightsholder and CCC hereby object to any terms contained in any writing prepared by the User or its principals, employees, agents or affiliates and purporting to govern or otherwise relate to the licensing transaction described in the Order Confirmation, which terms are in any way inconsistent with any terms set forth in the Order Confirmation and/or in these terms and conditions or CCC's standard operating procedures, whether such writing is prepared prior to, simultaneously with or subsequent to the Order Confirmation, and whether such writing appears on a copy of the Order Confirmation or in a separate instrument.

   8.5. The licensing transaction described in the Order Confirmation document shall be governed by and construed under the law of the State of New York, USA, without regard to the principles thereof of conflicts of law. Any case, controversy, suit, action, or proceeding arising out of, in connection with, or related to such licensing transaction shall be brought, at CCC's sole discretion, in any federal or state court located in the County of New York, State of New York, USA, or in any federal or state court whose geographical jurisdiction covers the location of the Rightsholder set forth in the Order Confirmation. The parties expressly submit to the personal jurisdiction and venue of each such federal or state court.If you have any comments or questions about the Service or Copyright Clearance Center, please contact us at 978-750-8400 or send an e-mail to support@copyright.com.

v 1.1

Figure C.5: Permission for inclusion of figure 2.1, p4

JOHN WILEY AND SONS LICENSE TERMS AND CONDITIONS

Oct 25, 2019

This Agreement between Peter Neathway ("You") and John Wiley and Sons ("John Wiley and Sons") consists of your license details and the terms and conditions provided by John Wiley and Sons and Copyright Clearance Center.

License Number	4695961463043
License date	Oct 25, 2019
Licensed Content Publisher	John Wiley and Sons
Licensed Content Publication	Neuropathology and Applied Neurobiology
Licensed Content Title	AMYLOID PLAQUES IN THE BRAINS OF MICE INFECTED WITH SCRAPIE: MORPHOLOGICAL VARIATION AND STAINING PROPERTIES
Licensed Content Author	H. FRASER, MOIRA E. BRUCE
Licensed Content Date	May 12, 2008
Licensed Content Volume	1
Licensed Content Issue	2
Licensed Content Pages	14
Type of use	Dissertation/Thesis
Requestor type	University/Academic
Format	Print and electronic
Portion	Figure/table
Number of figures/tables	1
Original Wiley figure/table number(s)	Figure 5.f
Will you be translating?	No
Title of your thesis / dissertation	Multifractal and Morphological Analysis of Retinal Amyloid Deposits for Staging in Alzheimer's Disease
Expected completion date	Jan 2020
Expected size (number of pages)	130
Requestor Location	Peter Neathway 200 University Ave W PHY 315 Waterloo, ON N2L 3G1 Canada Attn: Peter Neathway
Publisher Tax ID	EU826007151
Total	0.00 CAD
Terms and Conditions	

TERMS AND CONDITIONS

This copyrighted material is owned by or exclusively licensed to John Wiley & Sons, Inc. or one of its group companies (each a"Wiley Company") or handled on behalf of a society with

Figure C.6: Permission for inclusion of figure 2.6, p1

which a Wiley Company has exclusive publishing rights in relation to a particular work (collectively "WILEY"). By clicking "accept" in connection with completing this licensing transaction, you agree that the following terms and conditions apply to this transaction (along with the billing and payment terms and conditions established by the Copyright Clearance Center Inc., ("CCC's Billing and Payment terms and conditions"), at the time that you opened your RightsLink account (these are available at any time at http://myaccount.copyright.com).

Terms and Conditions

- The materials you have requested permission to reproduce or reuse (the "Wiley Materials") are protected by copyright.
- You are hereby granted a personal, non-exclusive, non-sub licensable (on a stand-alone basis), non-transferable, worldwide, limited license to reproduce the Wiley Materials for the purpose specified in the licensing process. This license, **and any CONTENT (PDF or image file) purchased as part of your order**, is for a one-time use only and limited to any maximum distribution number specified in the license. The first instance of republication or reuse granted by this license must be completed within two years of the date of the grant of this license (although copies prepared before the end date may be distributed thereafter). The Wiley Materials shall not be used in any other manner or for any other purpose, beyond what is granted in the license. Permission is granted subject to an appropriate acknowledgement given to the author, title of the material/book/journal and the publisher. You shall also duplicate the copyright notice that appears in the Wiley publication in your use of the Wiley Material. Permission is also granted on the understanding that nowhere in the text is a previously published source acknowledged for all or part of this Wiley Material. Any third party content is expressly excluded from this permission.
- With respect to the Wiley Materials, all rights are reserved. Except as expressly granted by the terms of the license, no part of the Wiley Materials may be copied, modified, adapted (except for minor reformatting required by the new Publication), translated, reproduced, transferred or distributed, in any form or by any means, and no derivative works may be made based on the Wiley Materials without the prior permission of the respective copyright owner.**For STM Signatory Publishers clearing permission under the terms of the STM Permissions Guidelines only, the terms of the license are extended to include subsequent editions and for editions in other languages, provided such editions are for the work as a whole in situ and does not involve the separate exploitation of the permitted figures or extracts,** You may not alter, remove or suppress in any manner any copyright, trademark or other notices displayed by the Wiley Materials. You may not license, rent, sell, loan, lease, pledge, offer as security, transfer or assign the Wiley Materials on a stand-alone basis, or any of the rights granted to you hereunder to any other person.
- The Wiley Materials and all of the intellectual property rights therein shall at all times remain the exclusive property of John Wiley & Sons Inc, the Wiley Companies, or their respective licensors, and your interest therein is only that of having possession of and the right to reproduce the Wiley Materials pursuant to Section 2 herein during the continuance of this Agreement. You agree that you own no right, title or interest in or to the Wiley Materials or any of the intellectual property rights therein. You shall have no rights hereunder other than the license as provided for above in Section 2. No right, license or interest to any trademark, trade name, service mark or other branding ("Marks") of WILEY or its licensors is granted hereunder, and you agree that you

Figure C.7: Permission for inclusion of figure 2.6, p2

shall not assert any such right, license or interest with respect thereto

- NEITHER WILEY NOR ITS LICENSORS MAKES ANY WARRANTY OR REPRESENTATION OF ANY KIND TO YOU OR ANY THIRD PARTY, EXPRESS, IMPLIED OR STATUTORY, WITH RESPECT TO THE MATERIALS OR THE ACCURACY OF ANY INFORMATION CONTAINED IN THE MATERIALS, INCLUDING, WITHOUT LIMITATION, ANY IMPLIED WARRANTY OF MERCHANTABILITY, ACCURACY, SATISFACTORY QUALITY, FITNESS FOR A PARTICULAR PURPOSE, USABILITY, INTEGRATION OR NON-INFRINGEMENT AND ALL SUCH WARRANTIES ARE HEREBY EXCLUDED BY WILEY AND ITS LICENSORS AND WAIVED BY YOU.

- WILEY shall have the right to terminate this Agreement immediately upon breach of this Agreement by you.

- You shall indemnify, defend and hold harmless WILEY, its Licensors and their respective directors, officers, agents and employees, from and against any actual or threatened claims, demands, causes of action or proceedings arising from any breach of this Agreement by you.

- IN NO EVENT SHALL WILEY OR ITS LICENSORS BE LIABLE TO YOU OR ANY OTHER PARTY OR ANY OTHER PERSON OR ENTITY FOR ANY SPECIAL, CONSEQUENTIAL, INCIDENTAL, INDIRECT, EXEMPLARY OR PUNITIVE DAMAGES, HOWEVER CAUSED, ARISING OUT OF OR IN CONNECTION WITH THE DOWNLOADING, PROVISIONING, VIEWING OR USE OF THE MATERIALS REGARDLESS OF THE FORM OF ACTION, WHETHER FOR BREACH OF CONTRACT, BREACH OF WARRANTY, TORT, NEGLIGENCE, INFRINGEMENT OR OTHERWISE (INCLUDING, WITHOUT LIMITATION, DAMAGES BASED ON LOSS OF PROFITS, DATA, FILES, USE, BUSINESS OPPORTUNITY OR CLAIMS OF THIRD PARTIES), AND WHETHER OR NOT THE PARTY HAS BEEN ADVISED OF THE POSSIBILITY OF SUCH DAMAGES. THIS LIMITATION SHALL APPLY NOTWITHSTANDING ANY FAILURE OF ESSENTIAL PURPOSE OF ANY LIMITED REMEDY PROVIDED HEREIN.

- Should any provision of this Agreement be held by a court of competent jurisdiction to be illegal, invalid, or unenforceable, that provision shall be deemed amended to achieve as nearly as possible the same economic effect as the original provision, and the legality, validity and enforceability of the remaining provisions of this Agreement shall not be affected or impaired thereby.

- The failure of either party to enforce any term or condition of this Agreement shall not constitute a waiver of either party's right to enforce each and every term and condition of this Agreement. No breach under this agreement shall be deemed waived or excused by either party unless such waiver or consent is in writing signed by the party granting such waiver or consent. The waiver by or consent of a party to a breach of any provision of this Agreement shall not operate or be construed as a waiver of or consent to any other or subsequent breach by such other party.

- This Agreement may not be assigned (including by operation of law or otherwise) by you without WILEY's prior written consent.

Figure C.8: Permission for inclusion of figure 2.6, p3

- Any fee required for this permission shall be non-refundable after thirty (30) days from receipt by the CCC.
- These terms and conditions together with CCC's Billing and Payment terms and conditions (which are incorporated herein) form the entire agreement between you and WILEY concerning this licensing transaction and (in the absence of fraud) supersedes all prior agreements and representations of the parties, oral or written. This Agreement may not be amended except in writing signed by both parties. This Agreement shall be binding upon and inure to the benefit of the parties' successors, legal representatives, and authorized assigns.
- In the event of any conflict between your obligations established by these terms and conditions and those established by CCC's Billing and Payment terms and conditions, these terms and conditions shall prevail.
- WILEY expressly reserves all rights not specifically granted in the combination of (i) the license details provided by you and accepted in the course of this licensing transaction, (ii) these terms and conditions and (iii) CCC's Billing and Payment terms and conditions.
- This Agreement will be void if the Type of Use, Format, Circulation, or Requestor Type was misrepresented during the licensing process.
- This Agreement shall be governed by and construed in accordance with the laws of the State of New York, USA, without regards to such state's conflict of law rules. Any legal action, suit or proceeding arising out of or relating to these Terms and Conditions or the breach thereof shall be instituted in a court of competent jurisdiction in New York County in the State of New York in the United States of America and each party hereby consents and submits to the personal jurisdiction of such court, waives any objection to venue in such court and consents to service of process by registered or certified mail, return receipt requested, at the last known address of such party.

WILEY OPEN ACCESS TERMS AND CONDITIONS

Wiley Publishes Open Access Articles in fully Open Access Journals and in Subscription journals offering Online Open. Although most of the fully Open Access journals publish open access articles under the terms of the Creative Commons Attribution (CC BY) License only, the subscription journals and a few of the Open Access Journals offer a choice of Creative Commons Licenses. The license type is clearly identified on the article.

The Creative Commons Attribution License

The Creative Commons Attribution License (CC-BY) allows users to copy, distribute and transmit an article, adapt the article and make commercial use of the article. The CC-BY license permits commercial and non-

Creative Commons Attribution Non-Commercial License

The Creative Commons Attribution Non-Commercial (CC-BY-NC)License permits use, distribution and reproduction in any medium, provided the original work is properly cited and is not used for commercial purposes.(see below)

Creative Commons Attribution-Non-Commercial-NoDerivs License

The Creative Commons Attribution Non-Commercial-NoDerivs License (CC-BY-NC-ND) permits use, distribution and reproduction in any medium, provided the original work is properly cited, is not used for commercial purposes and no modifications or adaptations are made. (see below)

Use by commercial "for-profit" organizations

Figure C.9: Permission for inclusion of figure 2.6, p4

Use of Wiley Open Access articles for commercial, promotional, or marketing purposes requires further explicit permission from Wiley and will be subject to a fee.
Further details can be found on Wiley Online Library
http://olabout.wiley.com/WileyCDA/Section/id-410895.html

Other Terms and Conditions:

v1.10 Last updated September 2015

Questions? customercare@copyright.com or +1-855-239-3415 (toll free in the US) or +1-978-646-2777.

Figure C.10: Permission for inclusion of figure 2.6, p5

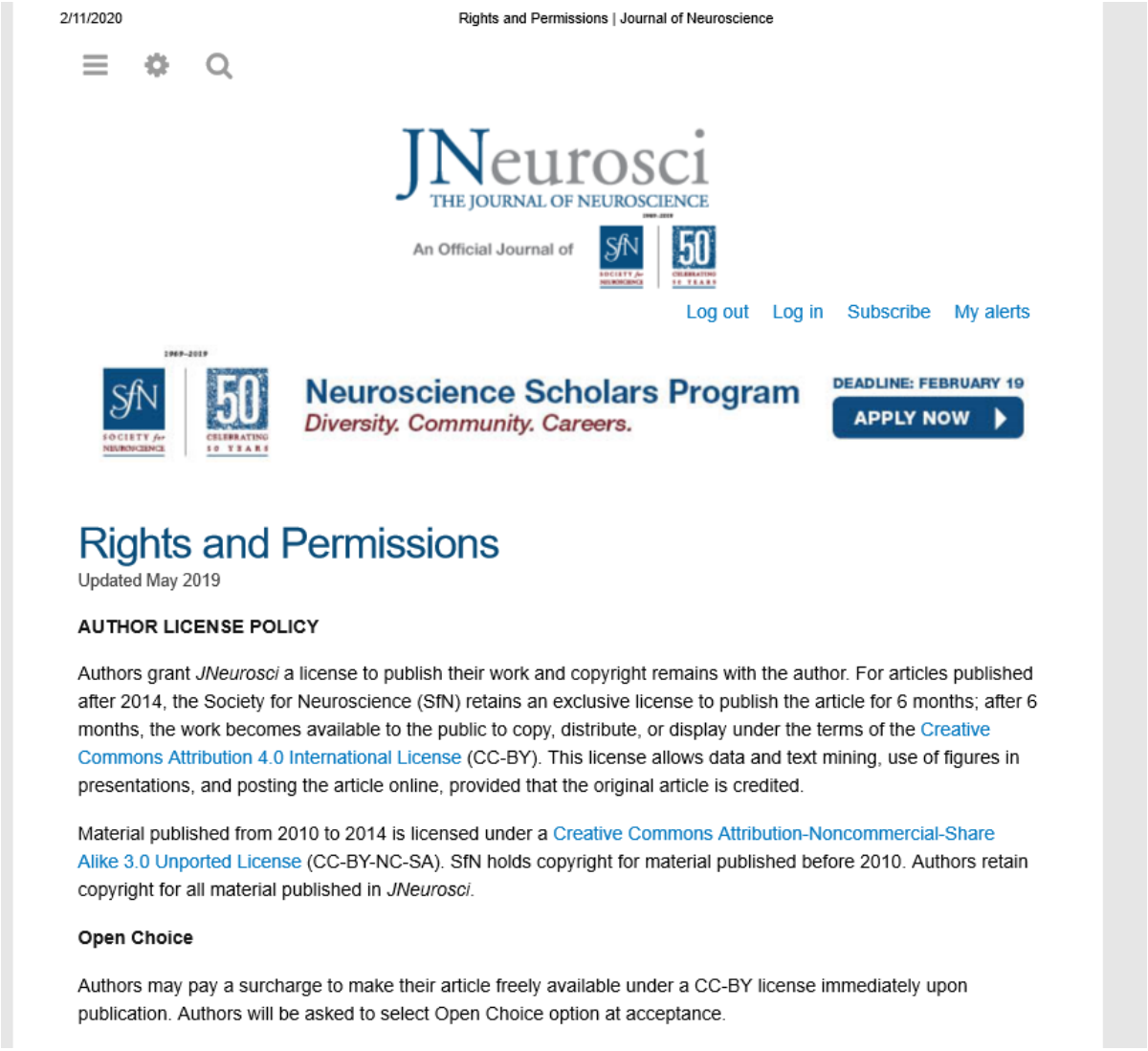

2/11/2020 Rights and Permissions | Journal of Neuroscience

JNeurosci
THE JOURNAL OF NEUROSCIENCE
An Official Journal of

Log out Log in Subscribe My alerts

Neuroscience Scholars Program
Diversity. Community. Careers.
DEADLINE: FEBRUARY 19
APPLY NOW

Rights and Permissions

Updated May 2019

AUTHOR LICENSE POLICY

Authors grant *JNeurosci* a license to publish their work and copyright remains with the author. For articles published after 2014, the Society for Neuroscience (SfN) retains an exclusive license to publish the article for 6 months; after 6 months, the work becomes available to the public to copy, distribute, or display under the terms of the Creative Commons Attribution 4.0 International License (CC-BY). This license allows data and text mining, use of figures in presentations, and posting the article online, provided that the original article is credited.

Material published from 2010 to 2014 is licensed under a Creative Commons Attribution-Noncommercial-Share Alike 3.0 Unported License (CC-BY-NC-SA). SfN holds copyright for material published before 2010. Authors retain copyright for all material published in *JNeurosci*.

Open Choice

Authors may pay a surcharge to make their article freely available under a CC-BY license immediately upon publication. Authors will be asked to select Open Choice option at acceptance.

Figure C.11: Permission for inclusion of figure 2.8b, p1

Author Rights

Authors do not need to obtain permission to reuse their material, including to:

- Reuse figures and tables in future works
- Include articles in theses or dissertations
- Reprint articles in books or compilations of their work
- Deposit the preprint version of their manuscript in an institutional repository or on their personal website. Th

JNeurosci-formatted PDF may be used after 6 months or immediately upon publication if the Open Choice opti was selected.

https://www.jneurosci.org/content/rights-permissions

The original article in *JNeurosci* must be cited and linked to, where appropriate.

Funder Mandates

JNeurosci automatically deposits all articles in PubMed Central regardless of funding status. Articles are deposite once they have appeared in an issue and will be freely available 6 months from the issue date, unless the authors selected Open Choice.

PERMISSION TO REUSE *JNEUROSCI* MATERIAL

Anyone may reprint original *JNeurosci* material without requesting permission. A full journal reference and link to version of record, where appropriate, must be included.

For content published before 2010, a copyright statement ("Copyright [year] Society for Neuroscience") should be included.

Questions should be directed to jnpermissions@sfn.org.

Figure C.12: Permission for inclusion of figure 2.8b, p2

Photocopies

JNeurosci is registered with the Copyright Clearance Center (CCC). Authorization to photocopy items for the internal or personal use of specific clients is granted by SfN provided that the copier pays the appropriate fee to the CCC.

Home
Alerts

Content
Early Release
Current Issue
Issue Archive
Collections

Information
For Authors
For the Media
For Subscribers

About
About the Journal
Editorial Board
Privacy Policy
Contact
Feedback

JNeurosci Print ISSN: 0270-6474 Online ISSN: 1529-2401

Figure C.13: Permission for inclusion of figure 2.8b, p3

WOLTERS KLUWER HEALTH, INC. LICENSE TERMS AND CONDITIONS

Oct 28, 2019

This Agreement between Peter Neathway ("You") and Wolters Kluwer Health, Inc. ("Wolters Kluwer Health, Inc.") consists of your license details and the terms and conditions provided by Wolters Kluwer Health, Inc. and Copyright Clearance Center.

License Number	4697701041220
License date	Oct 28, 2019
Licensed Content Publisher	Wolters Kluwer Health, Inc.
Licensed Content Publication	Stroke
Licensed Content Title	Cerebral Amyloid Angiopathy
Licensed Content Author	Gregory J. Zipfel, Henry Han, Andria L. Ford, et al
Licensed Content Date	Dec 8, 2008
Licensed Content Volume	40
Licensed Content Issue	3_suppl_1
Type of Use	Dissertation/Thesis
Requestor type	Individual
STM publisher name	
Portion	Figures/table/illustration
Number of figures/tables/illustrations	1
Figures/tables/illustrations used	2
Author of this Wolters Kluwer article	No
Title of your thesis / dissertation	Multifractal and Morphological Analysis of Retinal Amyloid Deposits for Staging in Alzheimer's Disease
Expected completion date	Jan 2020
Estimated size(pages)	130
Requestor Location	Peter Neathway 200 University Ave W PHY 315 Waterloo, ON N2L 3G1 Canada Attn: Peter Neathway
Total	0.00 CAD
Terms and Conditions	

Wolters Kluwer Health Inc. Terms and Conditions

1. **Duration of License:** Permission is granted for a one time use only. Rights herein do not apply to future reproductions, editions, revisions, or other derivative works. This permission shall be effective as of the date of execution by the parties for the maximum period of 12 months and should be renewed after the term expires.

Figure C.14: Permission for inclusion of figure 2.12, p1

i. When content is to be republished in a book or journal the validity of this agreement should be the life of the book edition or journal issue.
ii. When content is licensed for use on a website, internet, intranet, or any publicly accessible site (not including a journal or book), you agree to remove the material from such site after 12 months, or request to renew your permission license

2. **Credit Line:** A credit line must be prominently placed and include: For book content: the author(s), title of book, edition, copyright holder, year of publication; For journal content: the author(s), titles of article, title of journal, volume number, issue number, inclusive pages and website URL to the journal page; If a journal is published by a learned society the credit line must include the details of that society.
3. **Warranties:** The requestor warrants that the material shall not be used in any manner which may be considered derogatory to the title, content, authors of the material, or to Wolters Kluwer Health, Inc.
4. **Indemnity:** You hereby indemnify and hold harmless Wolters Kluwer Health, Inc. and its respective officers, directors, employees and agents, from and against any and all claims, costs, proceeding or demands arising out of your unauthorized use of the Licensed Material
5. **Geographical Scope:** Permission granted is non-exclusive and is valid throughout the world in the English language and the languages specified in the license.
6. **Copy of Content:** Wolters Kluwer Health, Inc. cannot supply the requestor with the original artwork, high-resolution images, electronic files or a clean copy of content.
7. **Validity:** Permission is valid if the borrowed material is original to a Wolters Kluwer Health, Inc. imprint (J.B Lippincott, Lippincott-Raven Publishers, Williams & Wilkins, Lea & Febiger, Harwal, Rapid Science, Little Brown & Company, Harper & Row Medical, American Journal of Nursing Co, and Urban & Schwarzenberg - English Language, Raven Press, Paul Hoeber, Springhouse, Ovid), and the Anatomical Chart Company
8. **Third Party Material:** This permission does not apply to content that is credited to publications other than Wolters Kluwer Health, Inc. or its Societies. For images credited to non-Wolters Kluwer Health, Inc. books or journals, you must obtain permission from the source referenced in the figure or table legend or credit line before making any use of the image(s), table(s) or other content.
9. **Adaptations:** Adaptations are protected by copyright. For images that have been adapted, permission must be sought from the rightsholder of the original material and the rightsholder of the adapted material.
10. **Modifications:** Wolters Kluwer Health, Inc. material is not permitted to be modified or adapted without written approval from Wolters Kluwer Health, Inc. with the exception of text size or color. The adaptation should be credited as follows: Adapted with permission from Wolters Kluwer Health, Inc.: [the author(s), title of book, edition, copyright holder, year of publication] or [the author(s), titles of article, title of journal, volume number, issue number, inclusive pages and website URL to the journal page].
11. **Full Text Articles:** Republication of full articles in English is prohibited.
12. **Branding and Marketing:** No drug name, trade name, drug logo, or trade logo can be included on the same page as material borrowed from *Diseases of the Colon & Rectum, Plastic Reconstructive Surgery, Obstetrics & Gynecology (The Green Journal), Critical Care Medicine, Pediatric Critical Care Medicine, the American Heart Association publications and the American Academy of Neurology publications.*
13. **Open Access:** Unless you are publishing content under the same Creative Commons license, the following statement must be added when reprinting material in Open Access journals: "The Creative Commons license does not apply to this content. Use of the material in any format is prohibited without written permission from the publisher, Wolters Kluwer Health, Inc. Please contact permissions@lww.com for further information."
14. **Translations:** The following disclaimer must appear on all translated copies: Wolters Kluwer Health, Inc. and its Societies take no responsibility for the accuracy of the translation from the published English original and are not liable for any errors which may occur.
15. **Published Ahead of Print (PAP):** Articles in the PAP stage of publication can be cited using the online publication date and the unique DOI number.
    i. Disclaimer: Articles appearing in the PAP section have been peer-reviewed and accepted for publication in the relevant journal and posted online before print publication. Articles appearing as PAP may contain statements, opinions, and information that have errors in facts, figures, or interpretation. Any final changes in manuscripts will be made at the time of print publication and will be reflected in the final electronic version of the issue. Accordingly, Wolters Kluwer Health, Inc., the editors, authors and their respective employees are not responsible or liable for the use of any such inaccurate or misleading data, opinion or information contained in the articles in this section.

Figure C.15: Permission for inclusion of figure 2.12, p2

16. **Termination of Contract:** Wolters Kluwer Health, Inc. must be notified within 90 days of the original license date if you opt not to use the requested material.
17. **Waived Permission Fee:** Permission fees that have been waived are not subject to future waivers, including similar requests or renewing a license.
18. **Contingent on payment:** You may exercise these rights licensed immediately upon issuance of the license, however until full payment is received either by the publisher or our authorized vendor, this license is not valid. If full payment is not received on a timely basis, then any license preliminarily granted shall be deemed automatically revoked and shall be void as if never granted. Further, in the event that you breach any of these terms and conditions or any of Wolters Kluwer Health, Inc.'s other billing and payment terms and conditions, the license is automatically revoked and shall be void as if never granted. Use of materials as described in a revoked license, as well as any use of the materials beyond the scope of an unrevoked license, may constitute copyright infringement and publisher reserves the right to take any and all action to protect its copyright in the materials.
19. **STM Signatories Only:** Any permission granted for a particular edition will apply to subsequent editions and for editions in other languages, provided such editions are for the work as a whole in situ and do not involve the separate exploitation of the permitted illustrations or excerpts. Please view: STM Permissions Guidelines
20. **Warranties and Obligations:** LICENSOR further represents and warrants that, to the best of its knowledge and belief, LICENSEE's contemplated use of the Content as represented to LICENSOR does not infringe any valid rights to any third party.
21. **Breach:** If LICENSEE fails to comply with any provisions of this agreement, LICENSOR may serve written notice of breach of LICENSEE and, unless such breach is fully cured within fifteen (15) days from the receipt of notice by LICENSEE, LICENSOR may thereupon, at its option, serve notice of cancellation on LICENSEE, whereupon this Agreement shall immediately terminate.
22. **Assignment:** License conveyed hereunder by the LICENSOR shall not be assigned or granted in any manner conveyed to any third party by the LICENSEE without the consent in writing to the LICENSOR.
23. **Governing Law:** The laws of The State of New York shall govern interpretation of this Agreement and all rights and liabilities arising hereunder.
24. **Unlawful:** If any provision of this Agreement shall be found unlawful or otherwise legally unenforceable, all other conditions and provisions of this Agreement shall remain in full force and effect.

For Copyright Clearance Center / RightsLink Only:

1. **Service Description for Content Services:** Subject to these terms of use, any terms set forth on the particular order, and payment of the applicable fee, you may make the following uses of the ordered materials:
    i. **Content Rental:** You may access and view a single electronic copy of the materials ordered for the time period designated at the time the order is placed. Access to the materials will be provided through a dedicated content viewer or other portal, and access will be discontinued upon expiration of the designated time period. An order for Content Rental does not include any rights to print, download, save, create additional copies, to distribute or to reuse in any way the full text or parts of the materials.
    ii. **Content Purchase:** You may access and download a single electronic copy of the materials ordered. Copies will be provided by email or by such other means as publisher may make available from time to time. An order for Content Purchase does not include any rights to create additional copies or to distribute copies of the materials

Other Terms and Conditions:
v1.18

Questions? customercare@copyright.com or +1-855-239-3415 (toll free in the US) or +1-978-646-2777.

Figure C.16: Permission for inclusion of figure 2.12, p3